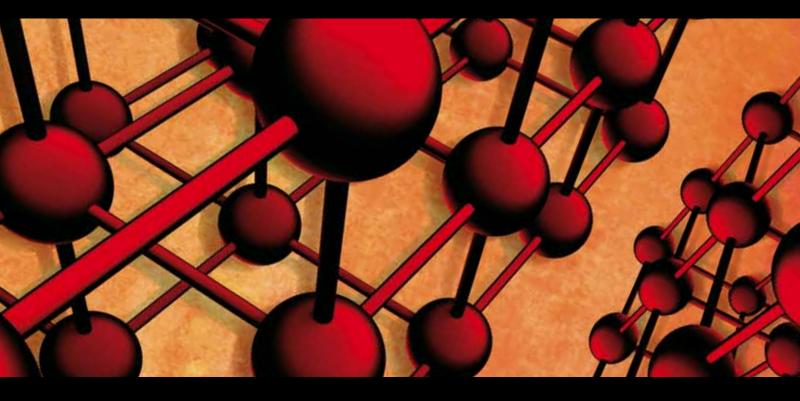
Materials, Devices, Fabrication, Characterization, and Applications for OLED Illumination and Display

Guest Editors: Jwo-Huei Jou, Yong Qiu, Saulius Grigalevicius, and Etienne Baranoff



Materials, Devices, Fabrication, Characterization, and Applications for OLED Illumination and Display

Materials, Devices, Fabrication, Characterization, and Applications for OLED Illumination and Display

Guest Editors: Jwo-Huei Jou, Yong Qiu, Saulius Grigalevicius, and Etienne Baranoff



Editorial Board

Marcel Ausloos, Belgium Robert S. Averback, USA V. P S Awana, India A. Bandyopadhyay, USA Z. Barber, UK Mark Blamire, UK Susmita Bose, USA Steve Bull, UK David Cann, USA Daolun Chen, Canada Manish Chhowalla, USA Paolo Colombo, Italy Martin Crimp, USA Jie Dai, Singapore C. K. Das, India Chris Davies, Australia J. Paulo Davim, Portugal Seshu Babu Desu, USA Yong Ding, USA Shi Xue Dou, Australia Chunying Duan, China Nadia El-Masry, USA David Field, USA Oiang Fu, China John Gillespie, USA Jeffrey T. Glass, USA Zhennan Gu, China Hiroki Habazaki, Japan Richard Hennig, USA

Dachamir Hotza, Brazil Chun-Hway Hsueh, USA Rui Huang, USA Shyh-Chin Huang, Taiwan Jacques Huot, Canada Hamlin Jennings, USA William A. Jesser, USA Ado Jorio, Brazil K. Kageyama, Japan S. Komarneni, USA Prashant Kumta, USA P. Lejcek, Czech Republic Markku Leskela, Finland Jun Li, Singapore Jing Li, USA Yuanhua Lin, China Zhimin Liu, China Meilin Liu, Georgia Maria Loi, The Netherlands Hai Lu, China Yiu-Wing Mai, Australia Peter Majewski, Australia Abdel S. Makhlouf, Germany Rajiv S. Mishra, USA S. Miyazaki, Japan Paul Munroe, Australia Korukonda Murty, USA Luigi Nicolais, Italy Tsutomu Ohzuku, Japan

Xiaoqing Pan, USA G. Ramanath, USA Raju Ramanujan, Singapore Jainagesh Sekhar, USA You Song, China Aloysius Soon, Korea Charles Sorrell, Australia Steven L. Suib, USA Wen-Hua Sun, China Sam-Shajing Sun, USA Achim Trampert, Germany An-Pang Tsai, Japan Vladimir Tsukruk, USA Krystyn Van Vliet, USA Stan Veprek, Germany Rui Vilar, Portugal Lianzhou Wang, Australia Kunpeng Wang, China John Wang, Singapore Jörg Wiezorek, USA Aiguo Xu, China Jenn-Ming Yang, Taiwan Jianqiao Ye, UK Yadong Yin, USA Jihong Yu, China Guan-Jun Zhang, China Dao Hua Zhang, Singapore

Contents

Materials, Devices, Fabrication, Characterization, and Applications for OLED Illumination and Display, Jwo-Huei Jou, Yong Qiu, Saulius Grigalevicius, and Etienne Baranoff Volume 2012, Article ID 878301, 2 pages

Simulation and System Design of a 3D Metrology Optical System Based on a Bidirectional OLED Microdisplay, Constanze Großmann, Ute Gawronski, Martin Breibarth, Gunther Notni, and Andreas Tünnermann Volume 2012, Article ID 417376, 9 pages

Reactive Chemical Vapor Deposition Method as New Approach for Obtaining Electroluminescent Thin Film Materials, Valentina V. Utochnikova, Oxana V. Kotova, Andrey A. Vaschenko, Leonid S. Lepnev, Alexei G. Vitukhnovsky, and Natalia P. Kuzmina Volume 2012, Article ID 809028, 9 pages

Polystyrene Backbone Polymers Consisting of Alkyl-Substituted Triazine Side Groups for Phosphorescent OLEDs, Beatrice Ch. D. Salert, Armin Wedel, Lutz Grubert, Thomas Eberle, Rémi Anémian, and Hartmut Krueger Volume 2012, Article ID 385178, 15 pages

Efficiency Control in Iridium Complex-Based Phosphorescent Light-Emitting Diodes, Boucar Diouf, Woo Sik Jeon, Ramchandra Pode, and Jang Hyuk Kwon Volume 2012, Article ID 794674, 14 pages

Blue Phosphorescent Organic Light-Emitting Devices with the Emissive Layer of mCP:FCNIr(pic), Ji Geun Jang and Hyun Jin Ji Volume 2012, Article ID 192731, 5 pages

LTPS-TFT Pixel Circuit Compensating for TFT Threshold Voltage Shift and IR-Drop on the Power Line for AMOLED Displays, Ching-Lin Fan, Min-Chi Shang, Wei-Chun Lin, Hsiu-Chen Chang, Kuang-Chi Chao, and Bo-Liang Guo Volume 2012, Article ID 270865, 5 pages

Enhancing the Out-Coupling Efficiency of Organic Light-Emitting Diodes Using Two-Dimensional Periodic Nanostructures, Qingyang Yue, Wei Li, Fanmin Kong, and Kang Li Volume 2012, Article ID 985762, 9 pages

Enhancement of Efficiency and Lifetime of Blue Organic Light-Emitting Diodes Using Two Dopants in Single Emitting Layer, Jianning Yu, Na Wei, Chong Li, Bin Wei, Wei Huang, Taiju Tsuboi, Jianhua Zhang, and Zhilin Zhang

Volume 2012, Article ID 247976, 4 pages

Hindawi Publishing Corporation Advances in Materials Science and Engineering Volume 2012, Article ID 878301, 2 pages doi:10.1155/2012/878301

Editorial

Materials, Devices, Fabrication, Characterization, and Applications for OLED Illumination and Display

Jwo-Huei Jou, 1 Yong Qiu, 2 Saulius Grigalevicius, 3 and Etienne Baranoff4

- ¹Department of Materials Science and Engineering, National Tsing-Hua University, Hsin-Chu 30013, Taiwan
- ² Department of Chemistry, Tsinghua University, Beijing 100084, China
- ³ Kaunas University of Technology, Lithuania
- ⁴ École Polytechnique Fédérale de Lausanne, Switzerland

Correspondence should be addressed to Jwo-Huei Jou, jjou@mx.nthu.edu.tw

Received 19 September 2012; Accepted 19 September 2012

Copyright © 2012 Jwo-Huei Jou et al. This is an open access article distributed under the Creative Commons Attribution License, which permits unrestricted use, distribution, and reproduction in any medium, provided the original work is properly cited.

The estimated global revenue is to be \$96 billion for lighting in 2012, and the same for flat panel display in 2018. Due to the numerous inherently disruptive advantages, such as being a plane light, very high in color rendering index, tunable color temperature, transparent, dimmable, humanfriendly, wide viewing angle, mercury free, sustainable raw materials, ultrathin, light weight, high contrast, fast response time and energy-saving, and so forth, organic light emitting diode (OLED) display and lighting will, sooner or later, take up a major portion of around \$200 billion revenue and eventually disrupt the current markets. Nowadays, OLED technology is on the threshold of reliability for numerous more contemporary applications. Even OLEDs have already met the requirements for some commercial applications in portable electronics, such as cellular phones, car stereos, digital cameras, and digital watches, there still some challenges especially like further increasing the lifetime and efficiency, while keeping the manufacturing cost lower, quality better, and emissive area size larger.

Recently, phosphorescent OLEDs had received a great deal of attention owing to their potential in achieving high efficiency, such as 100% internal quantum efficiency or 20% in external quantum efficiency (EQE), while 5% EQE for typical fluorescent OLEDs. In their review article, B. Diouf et al. discuss the key factors controlling the efficiency of phosphorescent OLEDs based on green and red emitting iridium complexes. The important factors discussed are exciton confinement, charge trapping, dopant concentration, and molecular structure of the materials. Interestingly, these

factors are presented as a full system taking into account the emitter, the host, and the adjacent layers as a whole.

The realization of deep-blue phosphorescent OLEDs has proved challenging. A significant restriction is the broad photoluminance spectrum characteristics of organic dopants. It is important to note that deep-blue or even pure-blue emission has not yet been observed from the phosphorescent emitters containing OLED devices to the moment. As a result, developing high-efficiency deep-blue OLEDs on the basis of phosphorescent dopants becomes crucial. In J. G. Jang and H. J. Ji paper, the authors investigated the deep-blue OLEDs using an emissive layer made of mCP as the host and FCNIr (pic) as the emitter. Optimization of the device architecture was achieved by varying the adjacent hole and electron transport layers, and results in a best device having CIE coordinates (0.14, 0.22) and 13.3% maximum external quantum efficiency.

The fabrication of small molecule based OLEDs generally requires thermal evaporation in a high vacuum. Thermal deposition process enables the formation of well controlled, homogeneous films, and the construction of very complex multilayer structures. This high freedom in layer design, allowing discrete charge transport and charge blocking layers to be formed, is one main reason accounting for the high efficiencies of OLEDs. Owing to the fact that molecular weight is too high for polymers to be thermally evaporated, polymer light emitting diodes (PLEDs) are often fabricated by solution processing techniques, such as spin-coating, inkjet printing, screen printing and rotogravure printing,

and so forth. Solution processed PLEDs hold significant promises for low cost devices. B. Ch. D. Salert et al. describe the synthesis and optoelectronic properties of a series of novel electron transporting polymers based on triazine moieties grafted on a polystyrene backbone. Furthermore, the polymers have been blended in the emissive layer containing a green emitting iridium complex and CoH-001 as a cohost.

Nowadays, OLED efficacy has already reached the fluorescent tube efficacy, but the lifetime remains a fundamental problem that limits its swiftness in commercialization. Luminance degradation is one of the crucial problems for broad spectrum of OLED lifetime and consistency. In J. Yu et al's paper, the authors investigated blue OLEDs using two dopants in single emitting layer. Higher efficiencies were obtained by codoping the emitting layer when compared to the case of noncodoping. The improvement was attributed to the charge balance in emitting layer. Additionally longer operational lifetime of the devices was achieved due to the expansion of recombination zone in emitting area.

All these research articles represent an innovative, exciting, novel and insightful observation into the state of the art, as well as promising opportunity for contemporary flat panel displays and solid state lightings. As reported in respective papers the performance of OLEDs can easily improve by the use of various efficient organic materials, such as novel dyes, various hosts, electron transporting materials, hole transporting materials, electron injection materials, hole injection materials, or by using a proper device structure and an efficient encapsulation techniques. This special issue is going to contribute significantly for development and commercialization of OLEDs.

Jwo-Huei Jou Yong Qiu Saulius Grigalevicius Etienne Baranoff Hindawi Publishing Corporation Advances in Materials Science and Engineering Volume 2012, Article ID 417376, 9 pages doi:10.1155/2012/417376

Research Article

Simulation and System Design of a 3D Metrology Optical System Based on a Bidirectional OLED Microdisplay

Constanze Großmann,^{1,2} Ute Gawronski,³ Martin Breibarth,³ Gunther Notni,³ and Andreas Tünnermann^{3,2}

- ¹ Fraunhofer IOF, Albert-Einstein-Straße 7, 07745 Jena, Germany
- ² IAP, Friedrich-Schiller University, Max-Wien-Platz 1, 07743 Jena, Germany

Correspondence should be addressed to Constanze Großmann, constanze.grossmann@iof.fraunhofer.de

Received 10 February 2012; Accepted 6 April 2012

Academic Editor: Yong Qiu

Copyright © 2012 Constanze Großmann et al. This is an open access article distributed under the Creative Commons Attribution License, which permits unrestricted use, distribution, and reproduction in any medium, provided the original work is properly cited.

Innovative display technologies enable a wide range of different system applications. specifically, in metrology, medical, and automotive applications microdisplays were increasingly used. In the last decades OLED microdisplays were in the focus of display development. A new class of OLED microdisplays with an integrated photodiode array is the latest development. The so-called bi-directional OLED microdisplays combine light-emitting devices (AM-OLED microdisplay) and photo sensitive detectors (photodiode matrix) on one single chip based on OLED-on-CMOS-technology. Currently this kind of display is still a prototype. Based on such a novel bidirectional OLED microdisplay, we present for the first time a system simulation and design of a 3D optical surface metrology system. The first step is the full characterization of the microdisplay. Depending on the characterization results the future system parameters are determined. Based on the characterization results and the application parameters the system design parameters are defined. The functionality of the system is simulated, and a theoretical proof of concept is presented. An example for our application on 3D optical surface metrology system is evaluated.

1. Introduction

Expanding requirements on manufacturing technology increase the demands on noncontact metrology systems. Typical optical metrology systems are based on a separated light-emitting unit (e.g., projection unit) and detection unit (e.g., camera unit) [1, 2]. This fact limits the miniaturization of the sensor system. Furthermore, the use of two optoelectronical devices complicates the integration and the alignment, which leads to higher production costs.

Typically, a projection unit includes a light source with a collecting optics, illuminating a light modulator (such as DMD (digital micromirror device) or LCoS (liquid crystal on silicon) displays) and a projection lens, imaging the generated pattern into the measurement plane. A first step towards the miniaturization of such an unit is the application of a self-emitting microdisplay (as active matrix OLED microdisplay) for pattern generation [3]. OLED microdisplays are state-of-the-art microdisplays, and they are used in a wide range

of applications (e.g., multimedia, medical, and metrology applications [2–7]). Such devices comprise light source and light modulator in one element, minimizing the number of components in a system. In contrast to conventional projection systems OLED microdisplays allow a simple and small system integration [6].

A further miniaturization can be realized by applying a microdisplay combining OLED microdisplay and sensor unit (i.e., photodiode matrix) on one single element. Such a bidirectional OLED microdisplay (BiMiD) was realized using OLED-on-CMOS-technology by Fraunhofer IPMS [8–10]. That means that the light source/image device is placed in the same plane as the detector. The bi-directional display used in this investigation consists of an AM-OLED microdisplay with an integrated photodiode matrix. That implies that each display pixel contains an emitting OLED pixel and a photodiode. Both functions work simultaneously and in the same wavelength range. First applications that are based on a similarly working BiMiD are flow, color, and reflex

³ Fraunhofer IOF, Albert-Einstein-Straße 7, 07745 Jena, Germany

sensors, which are presented in Reckziegel et al. [8]. Another application based on a BiMiD that works in different wavelength ranges for the OLED imaging and photodiode detection is an HMD and a distance sensor, which are mentioned in Richter et al. [9, 11].

In this paper we present a 3D surface optical metrology system based on phase-shifting fringe projection [1, 12–17] with BiMiDs. Fringes are projected onto the surface of measuring object. As they are observed via a different angle (triangulation angle), the fringes appear deformed according to the surface deformation of the measuring object. This deformation of the fringes allows calculating the 3D coordinates of all visible points. Up to now such systems are divided in a projection and an imaging unit increasing the size of the system.

We will demonstrate that the application of a bi-directional OLED microdisplay enables the realization of a highly integrated compact surface metrology sensor.

2. Fringe Projection Principle

A simple fringe projection 3D measurement system consists of an image acquisition sensor and a digital pattern (e.g., fringe) projector (see Figure 1(a)) [1]. The pattern/fringes are generated by a digital projection unit based on LCD, LCOS, DMD, or OLED microdisplay technology [2]. The image acquisition sensor can be applied as a conventional CCD. The 3D metrology system is based on fringe projection onto the surface of the measurement object. The fringes appear deformed when observed from a different angle (triangulation angle). The trinangulation angle is the angle between the optical axis of the projection lens and the imaging lens. From the deformation of the fringes the 3D coordinates of all visible points can be calculated and thus the object shape can be determined.

In Figure 1(b) a prototype of a 3D surface metrology system is shown. This system is based on an OLED projection unit and an imaging system. The trinangulation angle is 18°. The OLED microdisplay generates the fringe patterns that are projected via the projection lens onto the measuring object. The imaging lens displayed the object during the pattern sequence on the detector. Based on the variety of fringe images the 3D shape of the measuring object can be calculated. On the right side of Figure 1(b) the result of the measurement of a calibrated target is shown. A well-done conformity of the measured and target shape is presented.

A structured light approach combining the projection of a sequence of phase-shifted sinusoidal fringe patterns in combination with a sequence of Gray code patterns was used [18]. Due to the fact that phase-shifted sinusoidal fringe patterns produce 2π periodic phase values, additional phase unwrapping is necessary to solve these ambiguities, which is possible through the use of a Gray code sequence giving each sinus period a unique identifier [12, 17]. To be able to calculate 3D points on the objects surface using triangulation methods, at least 2 phase values for each 3D point are necessary in this setup along with a fully calibrated sensor arrangement (e.g., orientation parameters for the measurement camera and the fringe projector). This can be

achieved using two projected pattern sequences rotated 90° to each other. As a result each pixel in the measurement camera has a pair of phase values assigned to it. This pair of phase values describes exactly one position in the projector matrix (e.g., interpolated projector pixel). Using the orientation parameters of both sensor units, a simple triangulation can be used to calculate the 3D point on the surface [15]. Using this approach, the accuracy of the 3D coordinate measurement depends directly of the accuracy of the phase measurement (proportional).

3. Bidirectional OLED Microdisplay

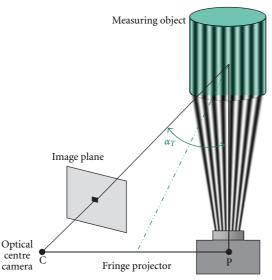
OLED microdisplays are widely used in the commercial applications like displays, which are directly observed by the user (mobile phone screens, head-mounted displays) [7, 9]. This display technology benefits from small geometrical size, low weight, low power consumption, and potentially high resolution [19]. High-brightness OLED microdisplays can also be applied as image generating devices in picoprojectors (e.g., for mobile phones) [2, 6]. However, those systems are unidirectional [9].

The development of light-emitting-polymer-(LEP-) on-CMOS-technology [19] opens the possibility to combine light emission and detection on one single chip. The so-called bi-directional OLED microdisplay (BiMiD), based on the OLED-on-CMOS-technology, has been developed by the Fraunhofer Institute for Photonic Microsystems (IPMS, Dresden)[8–10]. Such a display offers a new flexibility to optical metrology systems, because projection and imaging units can be combined in one optical path.

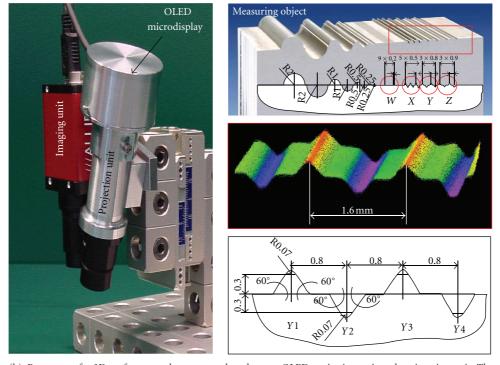
The CMOS-technology enables a simple electronics integration of OLED [19]. Figure 2 shows the cross-section of the design of the BiMiD. The CMOS top metal represents simultaneously the OLED bottom electrode (OLED cathode). A semitransparent thin metal layer is used as OLED electrode. The OLED layer is directly deposited onto the CMOS substrate. A detailed OLED layer structure is described in Reckziegel et al. [8]. The photodiodes (PDs) are embedded in the CMOS substrate. That means in each BiMiD pixel one OLED emitting pixel and one photodiode are integrated. Due to CMOS-technology (embedded photodiodes) a high fill factor of 90% comprising OLED pixel and photodiode can be realized.

The emitting unit is an active-matrix-(AM-) OLED microdisplay. Photodiodes with diameter of around 8 μ m are integrated in each OLED pixel (34 μ m²). The photodiodes are positioned about 7 μ m below the OLED layer. Figure 3(a) shows the BiMiD displaying an image, and Figure 3(b) shows a detailed view of the pixel structure.

Due to processing reasons, the first prototype of a BiMiD for our application has a limited photodiode resolution. Even though photodiodes are placed in each OLED pixel, only one photodiode out of four is integrated in the electronic control and therefore active. Accordingly, the photodiode resolution is reduced by four in comparison to the OLED resolution. The resulting resolution for the OLED microdisplay is QVGA (240 \times 320), and the photodiode resolution is QQVGA (120 \times 160). With this device, either



(a) Principle schematic of the basic fringe projection system. On the right side, the projector unit is placed, and, on the left side, the camera unite is positioned. Both these units are positioned in a specified triangulation angle α_T [1].



(b) Prototype of a 3D surface metrology system, based on an OLED projection unit and an imaging unit. The triangulation angle is 18°. On the right side, the measured target and the 3D shape model are shown [2, 4].

FIGURE 1: Principle design (left) and prototype (right) of the 3D surface metrology system based on one projection and one imaging unit.

simultaneous or sequential emission (OLED projection) and detection (photodiode) can be realized [20]. In the sequential mode of operation, the OLED projection and photodiode detection are wavelength independent ($\lambda_{OLED} \neq \lambda_{photodiode}$). In the simultaneous mode of operation, as we use it in our BiMiD prototype, OLEDs and photodiodes work in the same wavelength range ($\lambda_{OLED} = \lambda_{photodiode}$). In this case, however,

direct crosstalk effects between OLEDs and photodiodes can disturb the functionality.

We classify two different types of crosstalk: local and global crosstalk. Local crosstalk occurs directly between an OLED pixel and its neighbouring photodiodes, caused, for example, by internal reflection at CMOS layers (i.e., optical waveguide effect). In contrast to local crosstalk, global

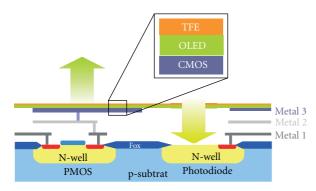


FIGURE 2: Cross-section of the bi-directional OLED-on-CMOS-microdisplay [9].

crosstalk indicates the influence of an emitting OLED pixel onto the photodiodes being spread over the whole display device. Global crosstalk can, for example, be caused by (e.g., multiple) reflections at the display cover glass and can therefore be detected by photodiodes being positioned not in the direct neighbourhood of the emitting OLED pixel. Local and global crosstalk have a strong impact onto the characteristics of the detected signal [11].

To limit the local crosstalk, we can take advantage of the limited resolution of photodiodes. As in a 2×2 pixel matrix only one photodiode is able to detect light, the OLED pixel surrounding the active photodiode is not used for light emission. Therefore, all images which are used are masked, that means that the OLED pixel including active photodiodes is inactive (e.g., black pixel projection). In this way, local crosstalk between the photodiode and its surrounding OLED can be prevented.

The current BiMiD prototype that we used for our prototype emits in the orange visible range ($\lambda_{cwl}=622$ nm) with a bandwidth of 48 nm (FWHM). The luminance of the OLED display at different voltage adjustments lies between 260 cd/m² and 7.8 kcd/m², which is suitable for high brightness projection applications. The radiation angle is around $\pm 45^{\circ}$ for each luminance level. The uniformity over the display is around 90%. The contrast ratio of the OLED display is around 30000:1 (ratio of full screen bright to full screen dark image). This impressible contrast ratio is a big advantage of OLED microdisplays in comparison to conventional microdisplays for projection purposes. The photodiodes exhibit a exposure time between 0.1434 ms and 1.174 s. The uniformity lies around 83% at the highest exposure times.

More details about the technology of the bi-directional OLED-on-CMOS-microdisplay are presented in Richter et al. [9].

4. Conceptual Design

The central element of our 3D sensor is the bi-directional OLED microdisplay (BiMiD). To prove the principle of the sensor the BiMiD was characterized. The measured parameters were used for the system simulation with the optical

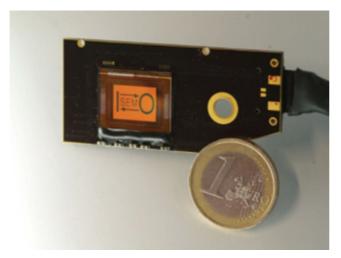
design program ZEMAX. In addition, a software for the generation of a 3D model was used.

First the BiMiD was characterized (see Section 3). The OLED microdisplay, the photodiode matrix (PD), and the crosstalk between OLED and photodiodes were evaluated. To measure the crosstalk of the BiMiD a paraxial lens design was used (see Figure 5). The BiMiD emits and detects light in the same plane and in the same spectral range. Figure 4(a) shows the projected test image (white square with a diagonal of 3 mm), and Figure 4(b) shows the detected image without additional optical elements (e.g., lens and mirror). A direct crosstalk between OLED pixel and photodiodes is detectable. The desired detection signal is lower than the crosstalk signal $(I_{\text{Detection}} < I_{\text{Crosstalk}})$. Due to the direct crosstalk the BiMiD active area was divided in two different fields: an object field and a detection field. In Figure 5 the paraxial lens design setup and the simplified laboratory setup that contains the separation of the projection and detection fields are shown. In the paraxial lens setup the blue path describes the projection path, and the green one describes the imaging path. Both object and image fields are placed next to each other. Fold mirrors are integrated in the projection path. The position of the fold mirrors and the dimension of the optical system configuration determine a triangulation angle (α_T) . The imaging path is unfolded. In both optical paths two paraxial lenses are integrated (Figure 5(a)). The realized setup including off-the-shelf optics is shown in Figure 5(b).

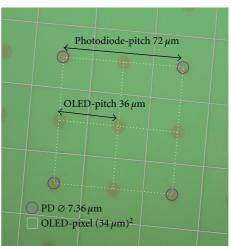
Figure 4(c) shows the detected image of the object. On the left-hand side the direct crosstalk image of the projection field and on the right hand side the object image are shown. Due to the internal display effect the active OLED pixel is imaged onto the photodiodes that are placed next to each other. Therefore, the projection object field and the detection field have to be separated via ray path folding. As described before the detection signal is not measureable in the area of the crosstalk. The distance (gap) between the projection and detection fields has to be larger than the crosstalk range radius. The dimension of the gap is depending on the OLED luminance and the photodiode sensitivity. For the following paraxial simulation the crosstalk around the projection field is neglected (gap = 0). But for further development of an optical prototype a gap > 0 between object field and detection field has to be considered.

As discussed before, the detection field has to be separated from the projection field on the display. Thereby, the detection field (diagonal 4.46 mm) is two times larger than the projection field (diagonal 8.92 mm) to realize a higher resolution (592×592 Pixel) for the imaging path. Figure 6 shows the compact paraxial optical system design for the 3D sensor: on the left side the BiMiD and on the right side the MO

The object (e.g., fringe pattern, see Figure 7) is imaged by a paraxial lens into the focal plane of the sensor. In the focal plane a MO is placed. Via a second paraxial lens the MO is observed during the fringe projection sequence and the image is detected by the PD. The system parameters are shown in Table 1. The OLED (object field) emits with

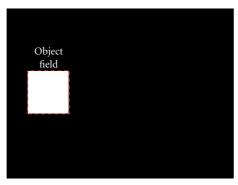




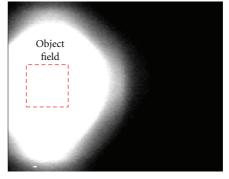


(b) Detailed view of the pixel matrix. The green pixel represents the OLED pixel and the circular mark highlights the active integrated photodiodes.

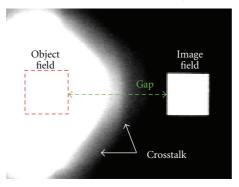
FIGURE 3: Bidirectional OLED-on-CMOS-microdisplay (at Fraunhofer IPMS).



(a) Test image of the object field (projection path, diagonal 3 mm).

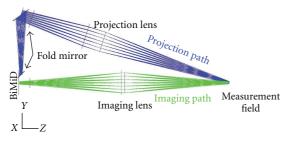


(b) Detected test image via the integrated photodiode matrix (PD) without optical elements (e.g., lens, mirror).

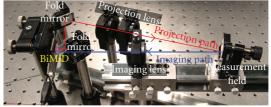


(c) Image of the detected test image in the labor setup (see Figure 5(b)) (detection path).

FIGURE 4: Image of test image and the detected photodiode image applying the 3D sensor system application (triangulation angle). The red square highlighted the object projection field. Due to the crosstalk effect the projection and detection fields have to be separated.



(a) Paraxial lens design of the function test.



(b) Labor setup of the paraxial lens design. The red path describes the projection path and the blue describes the imaging path.

FIGURE 5: Paraxial lens design and laboratory setup of the function test of an 3D sensor system. On the left-hand side the bi-directional OLED microdisplay is positioned. The projection path is folded by a fold mirror. The imaging path is unfolded. Both optical system magnifications are approximately $\beta' \approx -1$. The diagonal of the projection and imaging field is 3 mm. At first the object field is projected into the measurement field, and then the illuminated measurement field is imaged onto the bi-directional microdisplay (detection plane).

TABLE 1: System parameters of the paraxial lens design of the 3D sensor system (see Figure 6).

Visible
0.019
0.13
5 mm
6 mm
0.224
11.15
3.564 mm
0.85 mm
8.92 mm
±9°
$\approx 160 mm$
592×592 Pixel
$12.8 \text{mm} \times 9.6 \text{mm}$

lambertian radiation characteristic, and the measurement object emits with uniform radiation characteristics.

To realize a measurement field of around 0.85 mm the magnification of the projection lens is about -1/5. The imaging magnification is 11x. The measurement field diagonal is 0.85 mm. The distance between BiMiD and measurement plane is approximately 160 mm. Both system apertures are small, and the paraxial lens diameter at the projection path is 5 mm and at the imaging path 6 mm. The triangulation angle is $\alpha_T = \pm 9^\circ$; that means that the image is projected onto the measurement object under an angle of 9° .

The complete system principle is shown simplified in Figure 8. The first simulation part is to simulate the projection path of the OLED image. The OLED acts as an image/light source with lambertian radiation characteristics. The fringe pattern image is projected on the MO. In the first simulation step, the MO is used as a detector. The images are saved and used for the second simulation step, the imaging/detection path. The detected image, MO with fringes, acts as an image/light source for the imaging of the MO

into the real detector plane, the BiMiD. The radiation characteristic of the MO-fringe image is uniform. Figure 8(a) shows one of the fringe pattern images that is displayed in the measurement plane on the MO. The MO is a sinusoidal ideal object which is shown in Figure 8(b) and Figure 9(a). Figure 8(c) depicts the detected image of the MO during one fringe projection sequence. For the second part of simulation this image acts as an image/light source. The image is projected into the BiMiD detection field as shown in Figure 8(d). 46 fringe pattern images and 2 reference images were imaged onto the MO. Therefore, 48 images of the MO with fringe pattern were imaged into the BiMiD detection field (23 pattern images for each orientation, horizontal or vertical, and 2 reference images) (see Figure 7). Based on these detection images (BiMiD) the simulated measurement object could be recalculated to a 3D model. The result is shown in Figure 8(e) and Figure 9(b).

For the 3D calculation we decided to use a 16-step phase shift of the fringe pattern. Each pattern consists of a series of fringes next to each other with a width of 16 pixels each. During the sequence each pattern is shifted by 1 pixel between two adjacent steps. The basic pattern size is $1024 \times$ 1024 consisting of 64 periods of fringes (independent of the projector resolution, only the centered area is projected onto the object). This implies a gray code sequence of 7 images resulting in 23 images projected in one direction. As reference a black image and a bright image are also recorded. Therefore, we use 48 images for the complete measurement. In Figure 7 some test images are shown. During measurement each pixel records a series of intensity values. The periodic phase value is calculated from the intensity values of the 16 fringe patterns normalized with the dark and the bright image for reference using interpolation. Phase unwrapping is done using the Gray code images in the sequence. The intensity values of the Gray code sequence for each pixel are translated into a binary sequence representing the period number. Now a multiple of 2π is added to each periodic phase value depending on its period number to unwrap the phase values. After this calculation the sinusoidal MO, which is simulated in ZEMAX, is recalculated to a 3D model.

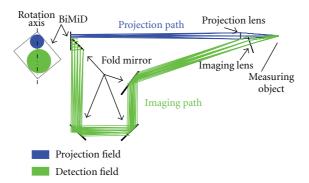


FIGURE 6: Paraxial optical system setup of the 3D sensor. On the left-hand side a top view of the BiMiD is shown and on the right-hand side the paraxial lens setup is shown. The projection and detection fields are oriented to reach the best fill factor for the microdisplay. Due to this effect the display is rotated for the paraxial system simulation. Projection and detection fields are orientated perpendicular. At the paraxial lens setup the bi-directional OLED microdisplay is positioned on the left side and on the right side the measurement object (e.g., sinusoidal mirror element) is placed. The blue ray path describes the projection and the green one describes the imaging path.

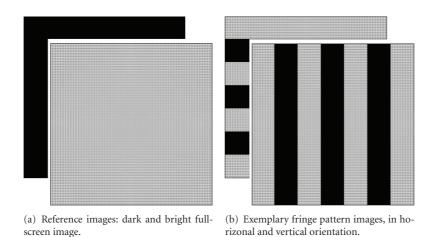


FIGURE 7: Simulated test images, which are used as source images for the projection path.

The recalculated and, for comparison, the simulated object is shown in Figure 9. The calculated 3D model shows well conformity to the simulated MO.

5. Conclusion

The monolithic design of OLED-on-CMOS backplane with photodiodes combines emitting and detecting units on one single chip. That offers a new flexibility for applications in optical metrology for surface and shape characterization and allows for compact optical systems, especially in the field of optical metrology.

In this paper we presented a compact, highly integrated 3D metrology system based on a fringe projection principle using a bi-directional OLED microdisplay developed by Fraunhofer IPMS. This microdisplay combines light emitting pixels called OLED microdisplay (projection unit) and light detecting pixels called photodiodes (camera unit) on one single device. This technology provides the opportunity for miniaturization of optical metrology systems.

In contrast to conventional 3D sensor systems (that are based on projection and imaging unti) the presented setup

based on BiMiD is compact. The presented 3D metrology system is based on fringe projection onto the surface of the measurement object. The fringes appear deformed when being observed via a different angle (triangulation angle). Based on the deformation of the fringes the 3D coordinates of all visible points can be calculated and, thus, the object shape can be determined.

Due to the internal crosstalk effect two separate lenses for projection and imaging are necessary. The system lens design is based on the BiMiD and two paraxial lenses, which are orientated via a triangulation angle of 18°. Both apertures are smaller than 6 mm. The measurement field has a diagonal of 0.85 mm. For the recalculation of the measurement object different reference and fringe pattern images are necessary. 23 fringe pattern images and 2 reference images are simulated through the optical system in both directions, projection and imaging, and both orientations, horizontal and vertical. Based on the detected images (images of the measuring object during fringe projection sequence), fringes are deformed due to the irregular measurement surface. The simulated measurement object can be recalculated to a 3D object model. Well conformity of the simulated and

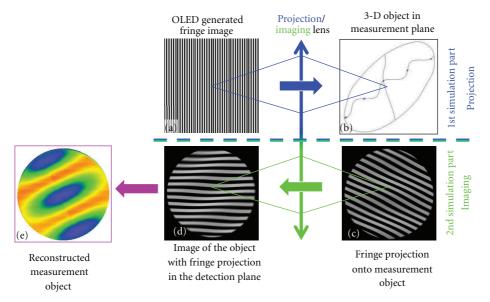


FIGURE 8: Principle of the 3D sensor system. The pattern images (OLED-BiMiD/(a)) are projected via a projection lens onto the measurement object (e.g., sinusoidal MO) (b). Then the detector (PD-BiMiD/(d)) detects the image of the measurement object during fringe projection (c). For this part the detected image of (c) is used as image/light source and is imaged into the BiMiD detector plane that is shown in (e). The 3D model is calculated with an internal Fraunhofer IOF software. (a) OLED generated fringe pattern image, (b) 3D measurement object, (c) fringe projection on the measurement object, (d) detected image of the measurement object during fringe projection, and (e) reconstructed 3D object.

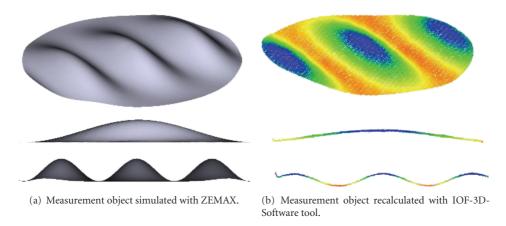


Figure 9: Simulated and reconstructed sinusoidal measuring object.

calculated measurement object could be shown. This system simulation shows the proof of concept of a 3D surface sensor based on bi-directional sensor device.

Due to the application of the bi-directional OLED microdisplay the fringe generating elements and the detectors are combined into one single device. Therefore, an ultracompact and solid system concept for 3D surface metrology has been realized. Such a compact sensor is very suitable for applications like inline quality control in manufacturing processes. In case of elimination of the crosstalk, it would be possible to realize a sensor with only one optics whereas in a next step, different optical system configurations, the application of microoptics, hybrid optics, and freeform optical elements will be considered to design and construct a full working 3D surface sensor.

Acknowledgments

The authors would like to thank the colleagues from Fraunhofer IPMS for their good cooperation. The project was supported by the German Federal Ministry for Education and Research (ISEMO, Project no. 16SV3682).

References

- [1] P. Kühmstedt, C. Munckelt, M. Heinze, C. Bräuer-Burchardt, and G. Notni, "3D shape measurement with phase correlation based fringe projection," in *Optical Measurement Systems for Industrial Inspection*, vol. 6616 of *Proceeding of SPIE*, 2007.
- [2] S. Riehemann, C. Grossmann, U. Vogel, B. Richter, and G. Notni, "Ultra small OLED pico projector," *Optik' Photonik*, vol. 4, no. 2, pp. 34–36, 2009.

- [3] G. Notni, S. Riehemann, P. Kühmstedt, L. Heidler, and N. Wolf, "OLED microdisplays—a new key element for fringe projection setups," in *Interferometry XII: Applications*, vol. 5532 of *Proceedings of SPIE*, pp. 170–177, usa, August 2004.
- [4] S. Riehemann, M. Palme, U. Lippmann, N. Wolf, and G. Notni, "System concept and optical design of miniaturized projection and imaging systems with OLED microdisplays," in *Optical Design and Engineering II*, vol. 5962 of *Proceedings of SPIE*, Jena, Germany, September 2005.
- [5] S. Riehemann, U. Lippmann, M. Palme, V. Vangdal, T. Thomson, and G. Notni, "Ocular OLED-HMD with simultaneous eye-tracking," in *Proceeding of the 44th International Symposium, Seminar, and Exhibition, SID*, vol. 37, no. 1, pp. 163–165, June 2006.
- [6] C. Großmann, S. Riehemann, G. Notni, and A. Tünnermann, "OLED-based pico-projection system," *Journal of the Society for Information Display*, vol. 18, no. 10, pp. 821–826, 2010.
- [7] M. Scholles, U. Vogel, I. Underwood et al., "HYPOLED Highperformance OLED microdisplays for mobile multimedia HMD and projection applications," in *Proceedings of the 48th Annual SID Symposium, Seminar, and Exhibition*, vol. 3, pp. 1926–1929, 2010.
- [8] S. Reckziegel, D. Kreye, T. Puegner et al., "Optical sensors based on monolithic integrated organic light-emitting diodes (OLEDs)," in *Optical Sensors*, vol. 7003 of *Proceedings of SPIE*, Strasbourg, France, April 2008.
- [9] B. Richter, U. Vogel, R. Herold et al., "Bidirectional OLED microdisplay: combining display and image sensor functionality into a monolithic CMOS chip," in *Proceedings of the IEEE International Solid-State Circuits Conference (ISSCC '11)*, pp. 314–315, February 2011.
- [10] U. Vogel, D. Kreye, S. Reckziegel, M. Törker, C. Grillberger, and J. Amelung, "OLED-on-CMOS integration for optoelectronic sensor applications," in *Silicon Photonics II*, vol. 6477 of *Proceedings of SPIE*, San Jose, Calif, USA, January 2007.
- [11] C. Grossmann, F. Perske, S. Zwick et al., "Surface metrology system based on bidirectional microdisplays," in *Optical Design and Engineering IV*, vol. 8167 of *Proceedings of SPIE*, 2011
- [12] F. Wahl, Mustererkennung, 1986.
- [13] J. Gerber, P. Kühmstedt, R. M. Kowarschik, G. Notni, and W. Schreiber, "Three-coordinate measuring system with structured light," in *Interferometry '94: Photomechanics*, vol. 2342 of *Proceedings of SPIE*, pp. 41–49, May 1994.
- [14] R. Kowarschik, P. Kühmstedt, J. Gerber, W. Schreiber, and G. Notni, "Adaptive optical three-dimensional measurement with structured light," *Optical Engineering*, vol. 39, no. 1, pp. 150–158, 2000.
- [15] W. Schreiber and G. Notni, "Theory and arrangements of self-calibrating whole-body three-dimensional measurement systems using fringe projection technique," in *Optical Engineering*, vol. 39 of *Proceedings of SPIE*, no. 1, pp. 159–169, 2000.
- [16] P. Kühmstedt, "Phasogrammetric optical 3D-sensor for the measurement of large objects," in *Optical Metrology in Produc*tion Engineering, vol. 5457 of *Proceedings of SPIE*, pp. 56–64, April 2004.
- [17] T. Luhmann, S. Robson, S. Kyle, and I. Harley, *Close Range Photogrammetry*, Luhmann 2006: Wiley, Whittles, 2006.
- [18] F. Chen, G. M. Brown, and M. Song, "Overview of three-dimensional shape measurement using optical methods," *Optical Engineering*, vol. 39, no. 1, pp. 10–22, 2000.
- [19] G. Kelly, R. Woodburn, I. Underwood et al., "A full-color QVGA microdisplay using light-emitting-polymer on CMOS," in Proceedings of the 13th IEEE International Conference on

- Electronics, Circuits and Systems(ICECS '06), pp. 760–763, December 2006.
- [20] D. Kreye, M. Toerker, U. Vogel, and J. Amelung, "Full colour RGB OLEDs on CMOS for active-matrix OLED microdisplays," in *Organic Ligh Emitting Materials and Devices X*, vol. 6333 of *Proceedings of SPIE*, San Diego, Calif, USA, August 2006.

Hindawi Publishing Corporation Advances in Materials Science and Engineering Volume 2012, Article ID 809028, 9 pages doi:10.1155/2012/809028

Research Article

Reactive Chemical Vapor Deposition Method as New Approach for Obtaining Electroluminescent Thin Film Materials

Valentina V. Utochnikova,^{1,2} Oxana V. Kotova,^{1,3} Andrey A. Vaschenko,² Leonid S. Lepnev,² Alexei G. Vitukhnovsky,² and Natalia P. Kuzmina¹

Correspondence should be addressed to Valentina V. Utochnikova, valentina.utochnikova@gmail.com

Received 21 March 2012; Revised 1 May 2012; Accepted 8 May 2012

Academic Editor: Yong Qiu

Copyright © 2012 Valentina V. Utochnikova et al. This is an open access article distributed under the Creative Commons Attribution License, which permits unrestricted use, distribution, and reproduction in any medium, provided the original work is properly cited.

The new reactive chemical vapor deposition (RCVD) method has been proposed for thin film deposition of luminescent non-volatile lanthanide aromatic carboxylates. This method is based on metathesis reaction between the vapors of volatile lanthanide dipivaloylmethanate (Ln(dpm)₃) and carboxylic acid (HCarb orH₂Carb') and was successfully used in case of HCarb. Advantages of the method were demonstrated on example of terbium benzoate (Tb(bz)₃) and o-phenoxybenzoate thin films, and Tb(bz)₃ thin films were successfully examined in the OLED with the following structure glass/ITO/PEDOT:PSS/TPD/Tb(bz)₃/Ca/Al. Electroluminescence spectra of Tb(bz)₃ showed only typical luminescent bands, originated from transitions of the terbium ion. Method peculiarities for deposition of compounds of dibasic acids H₂Carb' are established on example of terbium and europium terephtalates and europium 2,6-naphtalenedicarboxylate.

1. Introduction

A search for new electroluminescent (EL) materials for organic light-emitting diodes (OLEDs) is still an actual challenge for chemists. The solution of it means not only finding a compound which fits the EL material requirements but also the right choice or creation of a technique providing the transformation of such precursors into the thin films of high smoothness and low thickness. This can be demonstrated on examples of lanthanide coordination compounds which are well-known potential luminescent materials [1-5]. However, it is not that simple to find among them the luminescent lanthanide coordination compound, which demonstrates simultaneously high thermal and UV stability, bright luminescence, while being volatile or possesses high solubility to deposit thin film of high quality by physical methods from gas phase or solutions. In case of highly volatile β -diketonates the obvious physical

deposition technique allows to obtain thin films of high quality, and their luminescence efficiency can be increased by variation of the substituents in ligands. However these compounds do not exhibit required UV stability. A different situation arises from lanthanide aromatic carboxylates which show high UV, thermal, and chemical stability, as well as high luminescence efficiency, which can reach 100% in case of Tb(bz)₃ [6–9], but for these compounds the choice for the film deposition technique among known methods appears rather impossible. The aromatic carboxylates form extremely rigid 3D networks [10-12], which make them nonvolatile and poorly soluble in organic solvents that complicate deposition of their thin films from gas phase or solution and cause the necessity for search or development of the new methods. Thus, we have proposed the reactive chemical vapor deposition (RCVD) technique for thin films of nonvolatile luminescent lanthanide aromatic carboxylates (HCarb—aromatic monocarboxylic acid) [13, 14].

¹ Laboratory of Chemistry of Coordination Compounds, Chemistry Department, Lomonosov Moscow State University, 1-3 Leninskie Gory, 119991 Moscow, Russia

²Luminescence Division, Optical Department, Lebedev Physical Institute, 53 Leninsky Prosp., 119991 Moscow, Russia

³ School of Chemistry, Centre for Synthesis and Chemical Biology, Trinity College Dublin, College Green, Dublin 2, Ireland

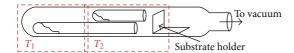


FIGURE 1: Two temperature zones reactor for gas phase reaction (1).

New RCVD method is based on the gas phase reaction between volatile $Ln(dik)_3$ (Hdik = β -diketone) and HCarb (reaction (1)):

$$\begin{array}{l} Ln(dik)_{3\,vapor} + \ xHCarb_{vapor} \\ \\ \longrightarrow \ LnCarb_{3\,solid} + \ 3Hdpm_{vapor}. \end{array} \tag{1}$$

The development of RCVD method involved two main steps: (1) study of general principles and (2) elicitation of reaction (1) parameters influencing the quality of thin films deposited (transparency, roughness, thickness, and coating continuity). Lanthanide dipivaloylmethanates, Ln(dpm)3, were selected as precursors because they are known as the most volatile and thermally stable nonfluorinated Ln(dik)₃; their vapor consists of mononuclear species only, and temperature dependencies of the saturated vapor pressure have been determined for compounds of all rare earth elements (REE_S) [15, 16]. Among monocarboxylic aromatic acids the series of HCarb was first selected to study the gas phase reaction (1), namely, benzoic acid (Hbz) and its o-substituted derivatives: salicylic acid (HSal), anthranilic acid (Habz), Nphenylanthranilic acid (HPA), and o-phenoxybenzoic acid (Hpobz), which differ by chemical stability and volatility [13]. These experiments were run within a horizontal quartz glass reactor with two temperature zones: T_1 for more volatile HCarb evaporation and T_2 for less volatile Ln(dpm)₃ evaporation and film deposition (Figure 1).

Variation of both T_1 and T_2 values allowed us to control the reagents partial vapor pressure ratio during the gas phase reaction. The vapors of HCarb and Ln(dpm)₃ converged in the zone T_2 , their interaction occurred, and nonvolatile products deposited on substrate and reactor walls in this hot zone. The composition of products deposited was evaluated by elemental, IR, ¹H NMR and luminescent spectroscopy analyses. The following main features of the proposed RCVD method were established: (1) gas phase ligand exchange reaction (1) takes place with a formation of Ln(Carb)₃ product; however there is a risk of its incompleteness, which causes product contamination by the $Ln(Carb)_{3-x}(dpm)_x$ impurities; (2) to exclude the formation of these impurities the ratio between the partial vapor pressures of HCarb and $Ln(dpm)_3$ should be >3:1; (3) the temperature T_2 of the reaction/deposition area should be sufficient to overcome the activation barrier of the reaction but it should not be higher than the temperatures of the decomposition of reactants and product; (4) $Ln(Carb)_{3-x}(dpm)_x$ impurities can be removed by reaction (2) under thermal treatment of the gas phase reaction product in the range of Ln(Carb)₃ stability [13]:

$$\operatorname{Ln}(\operatorname{Carb})_{3-x}(\operatorname{dpm})_{x}$$

$$\longrightarrow (3-x)/3 \operatorname{Ln}(\operatorname{Carb})_{3} + x/3 \operatorname{Ln}(\operatorname{dpm})_{3}.$$
(2)

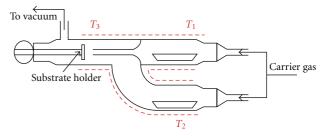


FIGURE 2: Three temperature zones RCVD reactor for thin films deposition.

To control these factors and to reveal their influence on the thin films quality the special RCVD reactor was constructed (Figure 2) [17].

In this reactor the evaporation zones (T_1, T_2) and film deposition zone (T_3) were separated, and reagents were transported separately into the deposition zone T_3 by a stream of carrier gas. The deposition parameters of transparent thin films with uniform composition, morphology, and thickness in the range of 50-100 nm were found for $Tb(bz)_3$ and $Tb(pobz)_3$. In order to analyze the composition of the thin films the special analytical approach, which corresponded to the combination of luminescent and Raman spectroscopy, was suggested [14, 18]. It worth noting that the temperatures (T_1, T_2, T_3) within the RCVD reactor play a crucial role in the composition, transparency, and morphology of Tb(Carb)₃ thin films. Therefore, transparent Tb(Carb)₃ thin films can be obtained under excessive pressures of HCarb (p(HCarb):p(Tb(dpm)₃) \gg 3), which is set by T_1/T_2 ratio, and T_3 value must be enough for activation of the reaction (2). The variation of Tb(Carb)₃ thin film thickness from 200 nm to 40 nm is possible by simply decreasing the amount of the reagents within the evaporation zones. Once these principles were fulfilled, it allowed us to deposit high-quality thin films of Tb(bz)₃ and $Tb(pobz)_3$ [14].

Here we present new results on EL test of $Tb(bz)_3$ thin films within OLED heterostructure and estimation of proposed RCVD method applicability for deposition of terbium and europium carboxylate thin films derivatives of dibasic acids H_2Carb' such as terephtalic (H_2 tph) and 2,6-naphtalenedicarboxylic (H_2 nda) acid.

2. Results and Discussion

2.1. $Tb(bz)_3$ as EL Layer within OLED. Thin films of $Tb(bz)_3$ deposited using RCVD method in three temperature zone reactor (Figure 2) were successfully used in the OLED structure such as glass/ITO/PEDOT:PSS/TPD/Tb(bz)₃/Ca/Al. EL spectra of $Tb(bz)_3$ showed only typical luminescent bands, originated from transitions of the terbium ion $^5D_4 \rightarrow ^7F_J$ (J=6-3), while no emission of hole transporting layers in the blue region was observed (Figure 3).

Thus the efficiency of the RCVD technique was demonstrated for deposition of the thin films for nonvolatile

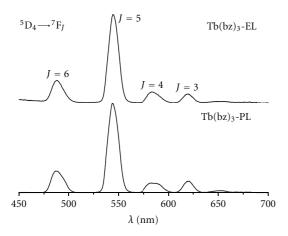


Figure 3: Normalized EL and PL spectra ($\lambda_{ex} = 337 \text{ nm}$) of Tb(bz)₃.

Tb(Carb)₃ complexes using highly volatile monobasic aromatic carboxylic acids (HCarb) as a precursors. The Tb(bz)₃ films deposited were of such high quality that their use in the OLED structure led to the bright Tb-centered electroluminescence without showing any sublayers luminescence.

2.2. RCVD Method Applicability for Thin Film Deposition of Tb and Eu Complexes with H2Carb'. Some lanthanide compounds with aromatic dibasic acids H₂Carb' could be prospective candidates for EL materials due to their bright luminescence and extremely high thermal stability [6, 9]. Terbium and europium derivatives of terephtalic (H₂tph) and 2,6-naphtalenedicarboxylic (H₂nda) acids are among the most promising candidates among these compounds; thus they were selected for study of the RCVD applicability for thin film deposition of nonvolatile lanthanide complexes with dibasic acids. The solid state carboxylates $Eu_2(tph)_3(H_2O)_4(I)$, $Tb_2(tph)_3(H_2O)_4(II)$, $Eu_2(nda)_3(H_2O)_6$ (III), and $Tb_2(nda)_3(H_2O)_6$ (IV) were synthesized according to the traditional method [19], and their luminescent properties and thermal stability were characterized to use them as standards for identification of the gas phase reaction products.

2.2.1. Luminescent Properties and Thermal Stability of the $Ln_2(Carb')_3(H_2O)_n$ Solid Samples (I–IV). Luminescent properties of the compounds I–IV were studied in comparison with those of H_2 tph and H_2 nda. Luminescence spectra of I and II (Figure 4) show only typical ion luminescent bands for both complexes, originated from the electronic transitions of the terbium or europium ions. No emission in the blue region was observed, which is the result of complete energy transfer from the organic part to the central ion. Besides a typical Stark splitting of the terbium emission bands is observed in the spectrum of II.

In case of $Ln_2(nda)_3(H_2O)_6$ only europium complex (III) shows ion luminescence, while in spectrum of terbium complex (IV) there are no terbium luminescence bands present, and a broad band in blue region, originated from the ligand emission, is observed. The hypsochromic shift

and narrowing of this band in comparison with H_2 nda luminescence band originate from the acid deprotonation and complexation with terbium ion.

The energy of nda^{2-} triplet level was estimated using the gadolinium compound $Gd_2(nda)_3(H_2O)_6$ phosphorescence spectrum. Unlike europium and terbium complexes, whose luminescence can be sensitized by coordinated ligands, gadolinium compounds do not emit visible light. However, the phosphorescence spectra of these complexes show signals resulting from triplet to singlet transitions and are thus reflecting the triplet state energies of the coordinated ligands [6]. According to the luminescence spectrum of $Gd_2(nda)_3(H_2O)_6$ (Figure S2) (see supplementary material available online at doi:10.1155/2012/809028) excited state level energies of nda^{2-} are $S_1(nda^{2-}) = 24200$ cm⁻¹, $T_1(nda^{2-}) = 18400$ cm⁻¹.

The simplified energy diagram (Figure 5) show that energy of the nda^{2-} triplet level is high enough only for energy transfer according to the scheme $T_1(nda^{2-}) \rightarrow {}^5D_0(Eu^{3+})$, while no energy transfer to ${}^5D_4(Tb^{3+})$ can occur.

In the excitation spectrum of H_2 tph two bands are observed (\sim 280 and \sim 330 nm) (Figure 6), which also presented in the spectra of I and II. Besides in the spectra of I and II the low intensity direct ion excitation bands at 360–420 nm and 350–370 nm, correspondingly, are observed. In the excitation spectrum of H_2 nda there are three bands (\sim 280 nm, \sim 370 nm, and \sim 425 nm). First two bands are also present in the spectrum of III, while the band at 425 nm is absent, which results from the absence of the energy transfer via the corresponding triplet state. The excitation spectrum of compound IV was recorded in the range of 200–350 nm since the maximum of its luminescence is 390 nm, and thus only the band at \sim 280 nm could be measured.

Thermogravimetric (TG) curves of **I–IV** were recorded in argon atmosphere and contain two steps of weight loss in all cases: the first step of water molecules elimination and the second step of $Ln_2(Carb')_3$ decomposition (Figure 7).

In case of I and II (Carb'=tph) the residues contained lanthanide oxides Eu_2O_3 and Tb_4O_7 , while III and IV (Carb'=nda) could not decompose completely in the inert atmosphere, and the residue most probably is contaminated with carbon.

2.2.2. Gas Phase Synthesis. The reaction providing the gas phase synthesis of $Ln_2(Carb')_3$ should take place according to (3):

$$\begin{split} 2Ln(dpm)_{3\,vapor} + 3H_2Carb'_{vapor} \\ \longrightarrow Ln_2\big(Carb'\big)_{3\,solid} \, + \, 6Hdpm_{vapor}. \end{split} \tag{3}$$

Brightly luminescent compounds I, II, and III were selected for these syntheses with the aim of their luminescent thin films deposition, but initially reactions (3) were performed in the reactor with two temperature zones (Figure 1).

A choice of the temperature regime providing course of the reaction (3) was based on analysis of the relations between volatility and stability of the starting reagents and products. The stability of Tb₂Carb'₃ against thermal

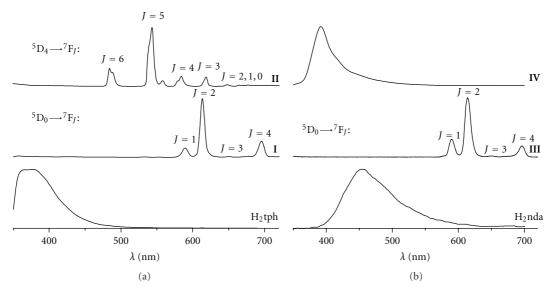


FIGURE 4: Normalized luminescence spectra of H_2 tph, $Eu_2(tph)_3(H_2O)_4(\mathbf{I})$, $Tb_2(tph)_3(H_2O)_4(\mathbf{II})$, H_2 nda, $Eu_2(nda)_3(H_2O)_6(\mathbf{III})$ and $Tb_2(nda)_3(H_2O)_6(\mathbf{IV})$ ($\lambda_{ex}=260$ nm).

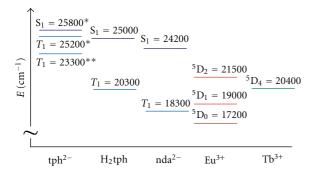


FIGURE 5: Simplified energy diagram of Eu^{3+} , Tb^{3+} , nda^{2-} , and H_2 tph, and tph²⁻ (*tph²⁻ energy levels values were taken from [20]; **tph²⁻ energy levels values were taken from [6]).

decomposition, determined from thermal analysis data, is rather high: I, II are stable until 400°C in inert atmosphere, III—until 600°C (Figure 7). H₂tph is stable at least until >400°C even in air [21]. This data is not available for H₂nda; however it can be purified by sublimation at 370°C in vacuum (0.01 mmHg) without decomposition, and thus it can be concluded that it is stable at least until this temperature. The data on the dependence between the vapor pressure and temperature for H2tph and H2nda is absent in the literature, and therefore volatility of these acids was estimated using thermal analysis in inert atmosphere in comparison with Hbz (Figure 8). For Hbz saturated vapor pressure temperature dependence is known [22], and empirical relation between the temperature range of its evaporation in gas phase reaction (1) and half weight loss temperature $(T_{1/2})$ in TG curve was established.

Thus, the thermogravimetric curves (Figure 8) indicate that the $T_{1/2}$ values increase in the row Hbz (180°C) < H₂tph (350°C) < H₂nda (390°C), which reflects the volatility row.

For Hbz it was shown [14, 23] that temperature of the acid evaporation zone should lie in the range of $(T_{1/2} \pm 100)^{\circ}$ C, and it means that for H₂tph and H₂nda the values of evaporation temperature could not be less than 250 and 300°C, respectively. According to the mass spectrometry data, Ln(dpm)₃ molecules are stable in gas phase only up to ~290°C, though the Ln-containing species with low partial pressures are present in the gas phase until at least 540°C [24]. Thus, Ln(dpm)₃ complexes are the least thermal stable reagents that can prevent carrying out reaction (3).

The diprotic nature of the H_2 Carb' acids can also hamper reaction (3). Earlier we have already studied the gas phase synthesis of the lanthanide complexes with diprotic ligands on example of yttrium complex with a Schiff base H_2 Salen (from ethylenediamine and salicylic aldehyde) [25]. It was shown that only a mixed-ligand complex of the composition Y(dpm)(Salen) was formed in both gas phase and solution interactions of $Y(dpm)_3$ and H_2 Salen even in the excess presence of the last one. We proposed that it resulted from the weak acidity of H_2 Salen ($pK_a \sim 11$ -12, [26]) contrary to HCarb ($pK_a = 4.21$ for Hbz) and the formation of two sixmembered chelate rings with yttrium ion.

The dibasic acids selected in this work are strong ($pK_a^1 = 3.51$ and $pK_a^2 = 4.82$ for H_2 tph; $pK_a^1 = 3.8$ and $pK_a^2 = 4.7$ for H_2 nda), and thus we expect that Ln_2 Carb'₃ as a product of the reaction (3) should form.

For the gas phase reaction less volatile H_2 Carb' were placed in the hotter zone T_2 and more volatile $Ln(dpm)_3$ —in the colder zone T_1 . For gas phase synthesis of **I** the following initial conditions were selected based on both thermal analysis for H_2 tph (Figure 8) and vapor pressure temperature dependences for $Eu(dpm)_3$ data [27]: $T_1(Eu(dpm)_3) = 160^{\circ}$ C and $T_2(H_2$ tph) = 250°C. Probably the value of T_2 was too low for sufficient vapor pressure of H_2 tph, and thus the product was not formed. The repeated experiment with

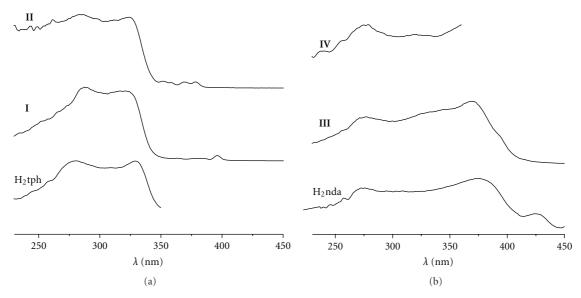


FIGURE 6: Normalized excitation spectra of H_2 tph ($\lambda_{em} = 380 \, \text{nm}$), $Eu_2(tph)_3(H_2O)_4$ (I, $\lambda_{em} = 612 \, \text{nm}$), $Tb_2(tph)_3(H_2O)_4$ (II, $\lambda_{em} = 545 \, \text{nm}$), H_2 nda ($\lambda_{em} = 450 \, \text{nm}$), $Eu_2(nda)_3(H_2O)_6$ (III, $\lambda_{em} = 612 \, \text{nm}$), and $Tb_2(nda)_3(H_2O)_6$ (IV, $\lambda_{em} = 390 \, \text{nm}$).

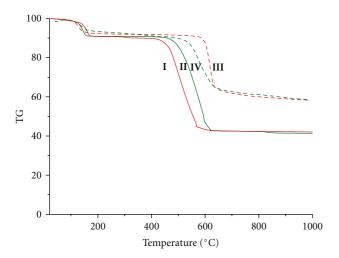


FIGURE 7: Thermogravimetric curves of $Ln_2(Carb')_3(H_2O)_n$ (I–IV).

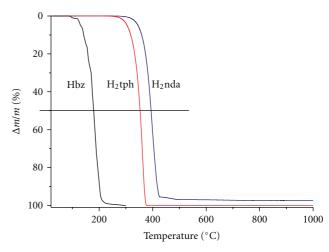


FIGURE 8: TG curves of Hbz, H2tph, and H2nda.

 $T_1(\text{Eu}(\text{dpm})_3) = 160^{\circ}\text{C}$ and $T_2(\text{H}_2\text{tph}) = 300^{\circ}\text{C}$ led to a product formation, but its quantity was extremely low, and it was formed as a thin film (i film) on the surface of glass substrate and reactor walls. The experiment on terbium terephthalate deposition at the same values of T_1 and T_2 led to ii film formation.

The emission spectra of both i and ii films show a broad fluorescence signal with the maximum at $\sim 360\,\mathrm{nm}$ besides the ion luminescence of $\mathrm{Eu^{3+}}$ and $\mathrm{Tb^{3+}}$, which is illustrated in Figure 9 on example of ii film. At the same time excitation spectra demonstrate blue shift of the band edges in comparison with the spectra of I and II concomitantly with the absence of the band at $> 350\,\mathrm{nm}$, corresponding to the $\mathrm{dpm^-}$ -ligand (Figure 9) and thus revealing that the most probable composition of thin films corresponds to the $\mathrm{Ln_2Carb_3}(\mathrm{H_2Carb})_x$. The product of the

same composition was also formed by the reaction (3) in solution (see Supplementary Information), which annealing at 360° C led to pure Ln_2Carb_3 formation. However, during gas phase synthesis it was not possible to increase the T_2 in order to exclude the acid codeposition into the film, since this temperature is limited by the $Ln(dpm)_3$ stability in the gas phase. Therefore the annealing procedure was used to remove the H_2 tph impurity from i and ii films. Films annealed at 360° C for 1 hour did not contain the acid impurities according to both excitation and emission spectra, and their composition corresponded to $Ln_2(tph)_3$.

The explanation of the blue shift of the excitation spectra band edges for the thin films containing H₂tph can be found from the estimation of the singlet and triplet energy levels of terephtalic acid from emission spectra of H₂tph (Figure S3). The obtained value of the triplet energy level

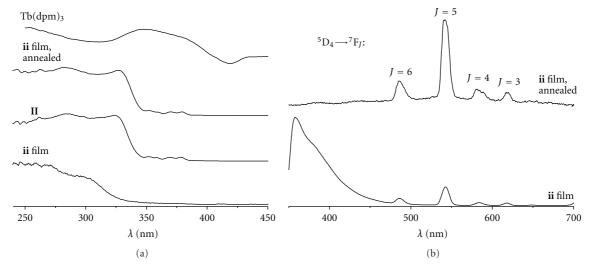


FIGURE 9: Normalized (a) excitation spectra of $Tb_2(tph)_3(H_2O)_4(II)$, ii film, ii film annealed, and $Tb(dpm)_3$ ($\lambda_{em} = 545 \text{ nm}$), and (b) emission spectra of ii film and ii film annealed ($\lambda_{ex} = 280 \text{ nm}$).

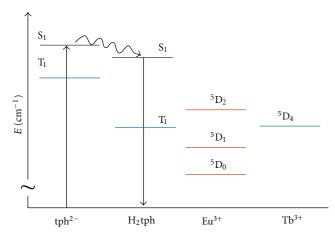


FIGURE 10: Simplified energy diagram showing the energy levels of tph^{2-} , H_2tph along with Eu^{3+} and Tb^{3+} .

(Figure 10) shows that in case of europium ion the ligands triplet states and europium resonance levels lie in the row $T_1(\text{tph}^{2-}) > T_1(\text{H}_2\text{tph}) > {}^5\text{D}_1(\text{Eu}^{3+})$ (Figure 10), which means that presence of terephtalic acid should simplify the energy transfer from tph^{2-} to europium ion. However according to the recorded spectra H_2tph presence is most likely preventing the energy transfer to Eu^{3+} ; thus we can conclude that H_2tph triplet state does not at all participate in the energy transfer processes, which could be described according to the scheme, presented in Figure 10.

In the case of terbium containing ii film two possible mechanisms of H_2 tph impact on the terbium ion luminescence can be proposed: (1) either H_2 tph triplet level can compete with terbium resonance level 5D_4 during the energy transfer processes or (2) the mechanism can be the same as in case of i film. Since the observed profiles of excitation spectra of i and ii films are the same (Figure 11), we can

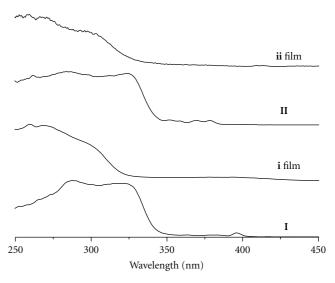


FIGURE 11: Normalized excitation spectra of $Eu_2(tph)_3(H_2O)_4(I)$, $Tb_2(tph)_3(H_2O)_4(II)$, i film, and ii film ($\lambda_{em}=612$ nm for I and i film, $\lambda_{em}=545$ nm for II and ii film).

suggest that the scheme of H_2 tph participation in the energy transfer in case of terbium compound is similar to that one for europium compound (Figure 10). Elimination of H_2 tph after annealing results in the band edge for thin films being identical to the reference solid state samples **I** or **II** (Figure 9) and proves the formation of the pure Ln_2 (tph)₃ films.

Since volatility of H_2 nda is lower than of H_2 tph, the gas phase reaction (3) with H_2 nda was performed at higher temperature $T_2(H_2$ nda) = 370°C and the same temperature $T_1(Eu(dpm)_3) = 160$ °C, which led to the **iii** film deposition. According to the luminescence spectra (Figure 12) this film was also contaminated with codeposited acid H_2 nda, which was removed after annealing at 370°C for 1 hour.

No., Ln	T_1 (H ₂ Carb'), °C	T_2 (Ln(dpm) ₃), °C	m_1 (H ₂ Carb'), g	m_2 (Ln(dpm) ₃), g	Product assignment	
		$H_2Carb' =$	H_2 tph			
1, Eu	160	250	0.58	0.075	N/A	
2, Eu	160	300	0.71	0.068	i film	
3, Tb	160	300	0.82	0.097	ii film	
$H_2Carb' = H_2nda$						
4, Eu	160	370	0.50	0.500	iii film	

TABLE 1: Experimental conditions of gas phases syntheses.

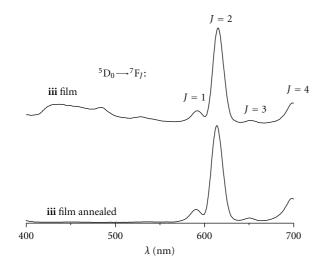


Figure 12: Normalized emission spectra of iii film and iii annealed film ($\lambda_{ex} = 260$ nm).

Thus the metathesis reaction (3) between $Ln(dpm)_3$ and dibasic acids H_2Carb' takes place in the gas phase, which was shown on example of $H_2Carb' = H_2tph$, H_2nda . However, due to the low volatility of these acids it is necessary to significantly increase the temperature of their evaporation in order to assure the vapor pressure. Simultaneously the raise of this temperature leads to the risk of $Ln(dpm)_3$ thermal decomposition in hot zone of the reactor. This mismatch of the temperature ranges of $Ln(dpm)_3$ stability in gas phase and H_2Carb' volatility results in the low yield of the product and the unsteadiness of the gas phase reaction, which cannot be excluded even by using the three-zone reactor. Thus gas phase reaction (3) takes place but is significantly hampered by the low volatility of H_2Carb' .

3. Conclusion

In conclusion we presented here the reactive chemical vapor deposition (RCVD) method for thin film deposition of non-volatile aromatic carboxylates, based on metathesis reaction between volatile Ln(dpm)₃ and aromatic carboxylic acids. The advantages of this method for deposition of thin films of lanthanide derivatives of the highly volatile monobasic acids were demonstrated on examples of terbium benzoate and *o*-phenoxybenzoate. The thin films of high quality were

deposited which allowed us to use them for OLED manufacturing on the example of Tb(bz)₃-based OLED with the structure glass/ITO/PEDOT:PSS/TPD/Tb(bz)₃/Ca/Al. The RCVD method was examined for deposition of the thin films of luminescent lanthanide derivatives of low-volatile dibasic carboxylic acids H₂tph and H₂nda. Here, the use of this method is complicated by the low volatility of the selected acids due to the mismatch of the temperature ranges of Ln(dpm)₃ stability in gas phase and H₂Carb' volatility. Thus RCVD method is perspective for highly volatile acids derivatives deposition and is significantly hampered in case of low volatile acids.

4. Experimental Part

Commercial dipivaloylmethane (Hdpm, Fluka) and pure for analysis grade terbium, europium, and gadolinium nitrate hexahydrates, sodium hydroxide (NaOH), and terephtalic acid (H₂tph, Acros organics) were used as received. Naphthalenedicarboxylic acid (H₂nda) and benzoic acid (Hbz) were purified by vacuum sublimation (0.01 mmHg) at 370 and 80°C, respectively.

The elemental analysis of complexes was carried out on a C,H,N-analyzer of the Organic Chemistry Division, Chemical Department, Lomonosov Moscow State University. Thermal analysis was carried out on a thermoanalyzer STA 409 PC Luxx (NETZSCH, Germany) in the temperature range of 20-1000°C in argon atmosphere, heating rate 10°/min. Photoluminescence and excitation spectra were measured on Perkin-Elmer LS-55 luminescence spectrometer utilizing with a xenon lamp with a tunable wavelength as an excitation source at 25°C as well as multichannel spectrometer S2000 (Ocean Optics) with a nitrogen laser LGI-21 ($\lambda_{\rm ex} = 337 \, {\rm nm}$) as an excitation source at 77 K. All emission and excitation spectra were corrected for the instrumental functions. The triplet state energy was estimated from maximum of the broad not resolved phosphorescence band in Gd₂(nda)₃(H₂O)₆ and H₂tph luminescence spectra at 77 K, distinguished from the second short-wave band, attributed to fluorescence (Figures S2 and S3).

The complexes $Ln(dpm)_3 \cdot 2H_2O$ (Ln = Eu, Tb) were synthesized and characterized by a standard procedure [15, 16]. Anhydrous $Ln(dpm)_3$ were obtained by sublimation of the hydrated complexes in vacuum (0.01 mmHg) at 120–150°C.

OLED manufacturing took place in a clean room class 10000 (Lebedev Physical Institute, Moscow, Russia) in a glovebox with argon atmosphere. Thin films of PEDOT:PSS with thickness \sim 30 nm were obtained by spin-coating. TPD layer was thermally evaporated (Univex-300, Leybord-Heraeus) under a pressure below 10^{-6} mmHg. The thickness was \sim 40 nm controlled by quartz indicator. Emitting layer (Tb(bz)₃) was deposited using RCVD technique at $T_1(\text{Tb}(\text{dpm})_3) = 125^{\circ}\text{C}$, $T_2(\text{Hbz}) = 140^{\circ}\text{C}$, $T_3 = 250^{\circ}\text{C}$. The contacts were attached to the electrodes, and the device was sealed with epoxy resin. Electroluminescence spectra were measured on a PicoQuant time-correlated single photon counting system used as a conventional spectrofluorimeter. Spectral resolution was 4 nm.

4.1. Synthesis of $Ln_2(Carb')_3$ (Ln = Eu, Tb; $H_2Carb' = H_2tph$, H_2nda). $Ln_2(Carb')_3 \cdot nH_2O$ (n = 4, 6) were synthesized by a standard procedure [19] by the reaction of water solutions of $Tb(NO_3)_3 \cdot 6H_2O$ (1 mmol) and of $K_2(Carb')$ (1.5 mmol, from KOH and H_2Carb').

 $Eu_2(tph)_3(H_2O)_4(I)$: for $Eu_2C_{24}H_{20}O_{16}$ (M = 868) anal. calcd. (%): C, 33.2; H, 2.3. Found (%): C, 30.7; H, 2.5.

IR spectrum, cm⁻¹: 3200–3600 (ν (O–H)), 3065 (ν (C–H)), 2982 (ν (C–H)), 2900 (ν (C–H)), 1590 (δ (C–C)), 1541 (ν _{as.} (COO)), 1505, 1410, 1420.

 $Tb_2(tph)_3(H_2O)_4(II)$: for $Tb_2C_{24}H_{20}O_{16}$ (M = 882) anal. calcd. (%): C, 32.7; H, 2.4. Found (%): C, 32.7; H, 2.6.

Raman spectrum, cm⁻¹: 3067 (C–H), 1612 s. (C–C arom.), 1529 (COO $_{as}^-$), 1456 s. (COO $_{sym}^-$), 1310, 1145, 869 s., 629.

IR spectrum, cm⁻¹: 3200–3600 (ν (O–H)), 3063 (ν (C–H)), 2983 (ν (C–H)), 2903 (ν (C–H)), 1587 (δ (C–C)), 1541 (ν _{as}(COO)), 1504, 1402, 1424.

 $Eu_2(nda)_3(H_2O)_6(III)$: for $Eu_2C_{36}H_{30}O_{18}$ (M=1054) anal. calcd. (%): C, 40.8; H, 2.9. Found (%): C, 40.8; H, 2.8.

Raman spectrum, cm⁻¹: 1632 (C–C arom.), 1487 (COO⁻), 1439 (COO⁻), 1394, 1122, 784, 523.

IR spectrum, cm⁻¹: 3200–3600 (ν (O–H)), 3059 (ν (C–H)), 2970 (ν (C–H)), 2913 (ν (C–H)), 1605 (δ (C–C)), 1540 (ν _{as}(COO)), 1490, 1409, 1358.

 $Gd_2(nda)_3(H_2O)_6$: for $Gd_2C_{36}H_{30}O_{18}$ (M = 1064) anal. calcd. (%): C, 40.0; H, 2.8. Found (%): C, 40.8; H, 2.8.

IR spectrum, cm⁻¹: 3200–3600 (ν (O–H)), 3060 (ν (C–H)), 2973 (ν (C–H)), 2910 (ν (C–H)), 1607 (δ (C–C)), 1544 (ν _{as}(COO)), 1493, 1410, 1353.

 $Tb_2(nda)_3(H_2O)_6(IV)$: for $Tb_2C_{36}H_{30}O_{18}$ (M=1068) anal. calcd. (%): C, 39.1; H, 2.8. Found (%): C, 40.5; H, 2.9.

IR spectrum, cm⁻¹: 3200–3600 (ν (O–H)), 3073 (ν (C–H)), 2887 (ν (C–H)), 2829 (ν (C–H)), 1602 (δ (C–C)), 1544 (ν _{as}(COO)), 1490, 1410, 1360.

4.2. Gas Phase Reaction of $Ln(dpm)_3$ and H_2Carb' ($H_2Carb' = H_2tph$, H_2nda ; Ln = Eu, Tb). The gas phase reaction of $Ln(dpm)_3$ with appropriate H_2Carb' was carried out under reduced pressure (0.01 mm Hg) in a horizontal glass reactor with two temperature zones (T_1 and T_2) (Figure 1). The unreacted volatile reactants were collected in the zone maintained at room temperature. The nonvolatile reaction

products condensed in the reactor zone with the temperature T_2 .

The time of experiments was 60 min. The values of temperatures of the reaction zones and masses of the reagents are summarized in Table 1.

Acknowledgments

The authors thank the Ministry of Education and Science of Russian Federation (contract no. 16.516.11.6071) for the financial support.

References

- [1] K. Binnemans, "Lanthanide-based luminescent hybrid materials," *Chemical Reviews*, vol. 109, no. 9, pp. 4283–4374, 2009.
- [2] L. D. Carlos, R. A. S. Ferreira, V. de Zea Bermudez, B. Julian-Lopez, and P. Escribano, "Progress on lanthanide-based organic-inorganic hybrid phosphors," *Chemical Society Reviews*, vol. 40, no. 2, pp. 536–549, 2011.
- [3] S. V. Eliseeva and J. C. G. Bünzli, "Rare earths: Jewels for functional materials of the future," *New Journal of Chemistry*, vol. 35, no. 6, pp. 1165–1176, 2011.
- [4] A. De Bettencourt-Dias, "Lanthanide-based emitting materials in light-emitting diodes," *Dalton Transactions*, no. 22, pp. 2229–2241, 2007.
- [5] M. A. Katkova and M. N. Bochkarev, "New trends in design of electroluminescent rare earth metallo-complexes for OLEDs," *Dalton Transactions*, vol. 39, no. 29, pp. 6599–6612, 2010.
- [6] M. Hilder, P. C. Junk, U. H. Kynast, and M. M. Lezhnina, "Spectroscopic properties of lanthanoid benzene carboxylates in the solid state: part 1," *Journal of Photochemistry and Photobiology A*, vol. 202, no. 1, pp. 10–20, 2009.
- [7] M. Hilder, M. Lezhnina, M. L. Cole, C. M. Forsyth, P. C. Junk, and U. H. Kynast, "Spectroscopic properties of lanthanoid benzene carboxylates in the solid state: part 2. Polar substituted benzoates," *Journal of Photochemistry and Photobiology A*, vol. 217, no. 1, pp. 76–86, 2011.
- [8] M. Bredol, U. Kynast, and C. Ronda, "Designing luminescent materials," *Advanced Materials*, vol. 3, no. 7-8, pp. 361–367, 1991.
- [9] R. Łyszczeka, Z. Rzączyńska, A. Kula, and A. Gładysz-Płaska, "Thermal and luminescence characterization of lanthanide 2,6-naphthalenedicarboxylates series," *Journal of Analytical and Applied Pyrolysis*, vol. 92, no. 2, pp. 347–354, 2011.
- [10] L. Armelao, S. Quici, F. Barigelletti et al., "Design of luminescent lanthanide complexes: From molecules to highly efficient photo-emitting materials," *Coordination Chemistry Reviews*, vol. 254, no. 5-6, pp. 487–505, 2010.
- [11] Y. E. Alexeev, B. I. Kharisov, T. C. H. García, and A. D. Garnovskii, "Coordination motifs in modern supramolecular chemistry," *Coordination Chemistry Reviews*, vol. 254, no. 7-8, pp. 794–831, 2010.
- [12] S. Qiu and G. Zhu, "Molecular engineering for synthesizing novel structures of metal-organic frameworks with multifunctional properties," *Coordination Chemistry Reviews*, vol. 253, no. 23-24, pp. 2891–2911, 2009.
- [13] V. V. Utochnikova, O. V. Kotova, E. M. Shchukina, S. V. Eliseeva, and N. P. Kuz'mina, "Gas-phase synthesis of terbium and lutetium carboxylates," *Russian Journal of Inorganic Chemistry*, vol. 53, no. 12, pp. 1878–1884, 2008.

- [14] O. V. Kotova, V. V. Utochnikova, S. V. Samoylenkov, A. D. Rusin, L. S. Lepnev, and N. P. Kuzmina, "Reactive chemical vapour deposition (RCVD) of non-volatile terbium aromatic carboxylate thin films," *Journal of Materials Chemistry*, vol. 22, no. 11, pp. 4897–4903, 2012.
- [15] K. J. Eisentraut and R. E. Sievers, "Volatile rare earth chelates," *Journal of the American Chemical Society*, vol. 87, no. 22, pp. 5254–5256, 1965.
- [16] C. Görller-Walrand and K. Binnemans, "Rationalization of crystal-field parametrization," in *Handbook on the Physics* and Chemistry of Rare Earths, K. A. Gschneidner Jr. and L. Eyring, Eds., vol. 23, Chapter 153, pp. 121–283, North-Holland, Amsterdam, The Netherlands, 1996.
- [17] S. V. Samoilenkov, O. V. Kotova, N. P. Kuzmina, L. S. Lepnev, and A. G. Vitukhnovskii, "Method of making thin films of chemical compounds and installation for realising said method," Patent Application Russia, CODEN: RUXXE7, RU2388770, 2010.
- [18] O. Kotova, S. Eliseeva, R. Muydinov, N. Kuzmina, and A. Kaul, "MOCVD application for thin film deposition of nonvolatile lanthanide carboxylates," *Proceedings Volumes of The Electrochemical Society*, vol. 9, pp. 306–311, 2005.
- [19] Gmelin Handbook of Inorganic Chemistry, System no. 39, vol. D4, Springer, Berlin, Germamy, 1984.
- [20] Z. Wang, Y. Yang, Y. Cui, Z. Wang, and G. Qian, "Color-tunable and white-light emitting lanthanide complexes based on (Ce_xEu_yTb_{1-x-y})₂(BDC)₃(H₂O)₄," *Journal of Alloys and Compounds*, vol. 510, no. 1, pp. L5–L8, 2011.
- [21] ICI Chemicals and Polymers Limited, Product Safety Data: Pure Terephthalic Acid, 1991.
- [22] T. E. Jordan, Vapor Pressure of Organic Compounds, Interscience, London, UK, 1954.
- [23] O. V. Kotova, V. V. Utochnikova, S. V. Eliseeva, S. V. Samoilenkov, and N. P. Kuz'mina, "Gas-phase synthesis of lanthanide(III) benzoates Ln(Bz)₃ (Ln = La, Tb, Lu)," Russian Journal of Coordination Chemistry, vol. 33, no. 6, pp. 454–457, 2007.
- [24] G. V. Girichev, N. I. Giricheva, N. V. Belova, A. R. Kaul, N. P. Kuzmina, and O. Yu. Gorbenko, "Yttrium dipivaloylmethanate thermal stability study using mass-spectrometry method," *Russian Journal of Inorganic Chemistry*, vol. 38, p. 2, 1993.
- [25] V. V. Utochnikova, O. V. Kotova, and N. P. Kuz'mina, "Solution and gas-phase synthesis of the heteroligand yttrium complex with dipivaloylmethane and bis(salicylidene)ethylenediamine Y(dpm)(salen)," *Moscow University Chemistry Bulletin*, vol. 62, no. 4, pp. 226–229, 2007.
- [26] F. Lloret, M. Mollar, J. Faus, M. Julve, I. Castro, and W. Diaz, "Solution chemistry of N,N'-ethylenebis(salicylideneimine) and its copper(II), nickel(II) and iron(III) complexes," *Inorganica Chimica Acta*, vol. 189, no. 2, pp. 195–206, 1991.
- [27] J. E. Sicre, J. T. Dubois, K. J. Eisentraut, and R. E. Sievers, "Volatile lanthanide chelates. II. Vapor pressures, heats of vaporization, and heats of sublimation," *Journal of the American Chemical Society*, vol. 91, no. 13, pp. 3476–3481, 1969.

Hindawi Publishing Corporation Advances in Materials Science and Engineering Volume 2012, Article ID 385178, 15 pages doi:10.1155/2012/385178

Research Article

Polystyrene Backbone Polymers Consisting of Alkyl-Substituted Triazine Side Groups for Phosphorescent OLEDs

Beatrice Ch. D. Salert,¹ Armin Wedel,¹ Lutz Grubert,² Thomas Eberle,³ Rémi Anémian,³ and Hartmut Krueger¹

- ¹ Department of Polymers and Electronics, Fraunhofer Institute for Applied Polymer Research, Geiselbergstraße 69, 14476 Potsdam, Germany
- ² Department of Chemistry, Humboldt University, Brook-Taylor-Straße 2, 12489 Berlin, Germany

Correspondence should be addressed to Hartmut Krueger, krueger@iap.fhg.de

Received 9 March 2012; Accepted 16 April 2012

Academic Editor: Etienne Baranoff

Copyright © 2012 Beatrice Ch. D. Salert et al. This is an open access article distributed under the Creative Commons Attribution License, which permits unrestricted use, distribution, and reproduction in any medium, provided the original work is properly cited.

This paper describes the synthesis of new electron-transporting styrene monomers and their corresponding polystyrenes all with a 2,4,6-triphenyl-1,3,5-triazine basic structure in the side group. The monomers differ in the alkyl substitution and in the meta-/ paralinkage of the triazine to the polymer backbone. The thermal and spectroscopic properties of the new electron-transporting polymers are discussed in regard to their chemical structures. Phosphorescent OLEDs were prepared using the obtained electron-transporting polymers as the emissive layer material in blend systems together with a green iridium-based emitter 13 and a small molecule as an additional cohost with wideband gap characteristics (CoH-001). The performance of the OLEDs was characterized and discussed in regard to the chemical structure of the new electron-transporting polymers.

1. Introduction

In 1990, when Burroughes et al. published first results on light-emitting diodes based on fluorescent conjugated polymers, these materials achieved more and more interest not only in science but also in technical application in displays and lighting [1]. From this time onwards, the development of full color flat panel displays was a main focus in research and development. Those displays would gain many advantages such as a wide viewing angle, high brightness and processing on flexible substrates. This is due to the ability of easy solution processing for large areas via different printing techniques like ink-jet printing [2] or roll-to-roll [3] procedures. During the past ten years, research activities have been more and more focused on phosphorescent systems. One reason for this is their lower power consumption [4]. Higher quantum efficiencies can be obtained in a light-emitting diode using phosphorescent transition metal complexes containing organic ligands instead of singlet-emitting materials [5]. Some transition

metal complexes, particularly iridium-(III) complexes, show very short triplet excited state lifetimes due to high radiative decay rates. Up to 100% internal quantum efficiencies of these phosphorescent emitters are possible in adapted host systems [6].

Solution-processable phosphorescent materials can be broken down into two categories—solution based small molecules and polymers. Both material approaches consist of a transition metal complex acting as an efficient emitter and of a charge transport host responsible for an efficient hole and electron transport to the emitter. Suzuki et al. [7] introduced polystyrene as nonconjugated polymer backbone carrying the emitter and the host units as covalent attached side groups. As it is known polystyrene is an optically and electrically stable backbone. Due to this fact, polystyrene can be used as the polymer main chain while substitutions of several active side groups can be investigated.

Following this idea, we recently introduced some novel hole- and electron-transporting units as side groups of a polystyrene backbone and tested them in phosphorescent

³ Merck KGaA, Frankfurter Straße 250, 64293 Darmstadt, Germany

devices [8-10]. To improve and to adapt the electron transport in phosphorescent systems for small-moleculebased OLEDs tris-(8-hydroxyquinoline) aluminum (AlQ₃) is a very commonly used electron transporting material. First reports using this material were published about 25 years ago [11]. During the past five years, research is looking for alternative electron-transporting materials. Chen et al. and Inomata et al. studied 1,3,5-triazine-core structures and their behavior in OLEDs. They used different substituted 1,3,5triazine core structures as small molecules in OLEDs [12, 13]. Klenkler et al. recently published a triazine-based structure which shows high electron mobility resulting in OLEDs with a lower driving voltage and higher efficiency [14]. Behl and Zentel [15] studied first p-vinyl-substituted 2,4,6-tripheny-1,3,5-triazine monomers, their polymerization, and the OLED performance using the obtained polymers as electrontransporting matrices.

In this paper, we now introduce several new electrontransporting units all based on a central 2,4,6-triphenyl-1,3,5-triazine unit. According to Chen et al. and Inomata et al. [12, 13], who studied 1,3,5-triazine-core structures as small molecules, we decided to combine the idea of those groups to the studies done by Suzuki et al. [7] using polystyrene as a nonconjugated polymer backbone. Besides analyzing a simple nonsubstituted 1,3,5-triazine core polymer, we wanted to get more information about OLED performance for substituted polymers. As substitution pattern we chose several small alkyl substituents and compared their properties with their nonsubstituted analogues in OLEDs. Therefore, several new styryl derivatives with different dialkyl substituents to the triazine core were synthesized and polymerized. The polymers were characterized with UV-Vis- and fluorescence spectroscopy and with DSC. Cyclovoltammograms of their monomers were discussed to describe the energy levels of their corresponding polymers. The influence of different 2,4,6-substitutions of the triazine core structures for the OLED performance was studied by using them as electron-transporting components. Therefore, blends of the new triazine containing polystyrenes with an iridium-tris-2-phenylpyridine derivative 13 as phosphorescent green emitter and a small molecule CoH-001 (from Merck) as an additional cohost with wideband gap characteristics were prepared. From the blends, OLEDs were built up, and the results are compared in regard to brightness, electroluminescence, and efficiency.

2. Experimental

2.1. Synthesis and Methods. All chemicals were obtained from Merck KGaA, Fluka or Sigma Aldrich and were used without further purification. All synthesis steps were carried out under argon atmosphere, and dry solvents were used which were stored over a molecular sieve. Silica gel (60 Merck) was used for column chromatography. The polymerizations were carried out in a glove box under argon atmosphere, and tetrahydrofuran (freshly distilled) was used. OLED device preparation was carried out in a glove box.

2.1.1. High Resolution with TMS as Standard NMR Spectra.

¹H-NMR and ¹³C-NMR spectra of the synthesized intermediates, monomers, and polymers were measured with a UNITY INOVA 500 Spectrometer from Varian. As solvents, deuterated chloroform or tetrahydrofuran was used.

Elemental analyses were obtained by using a Thermo Scientific FlashEA 1112 CHNS/O Automatic Elemental Analyser.

2.1.2. Gel Permeation Chromatography. To determine the molecular weights and their distribution of the synthesized polymers, a combined system consisting of a water HPLC pump 515, autosampler 717 plus, dual λ absorption detector 2487, and a refraction index detector 2414 was used. The polymers were measured in tetrahydrofuran at room temperature. A precolumn and three columns from Waters (7,8 mm \times 300 mm; Styragel HR3, HR4, HR5) filled with a copolymer of styrene and divinylbenzene 5 μ m and PS standards from Polymer Laboratories were used. Polymer solutions of 2 mg/L in tetrahydrofuran were used which were stirred at room temperature for 24 hours before they were filtered through a syringe filter (1 μ m) and measured.

Thermal analysis was obtained by using a Netzsch DSC 204 system with a scan rate of 10 K/min. About 5 mg of the polymer was weighed in a $40 \,\mu\text{L}$ aluminum pan.

- 2.1.3. UV/VIS Spectroscopy. The synthesized polymers were measured as a film on silica glass. The films were prepared from chloroform solution (7,5 mg/mL) by spin coating. For the measurement, a Carry 5000 UV/VIS Spectrometer of Perkin-Elmer was used.
- 2.1.4. Photoluminescence Spectroscopy. The same films that were used for UV-Vis measurements were measured at a Perkin-Elmer LS50B to determine photoluminescence. The excitation wavelength was 300 nm.
- 2.1.5. Cyclovoltammetry. Cyclic voltammetry was performed using a PG310 USB (HEKA Elektronik) potentiostat interfaced to a PC with PotMaster v2x43 (HEKA Elektronik) software for data evaluation. A three-electrode configuration contained in a nondivided cell consisting of a platinum disc ($d=1\,\mathrm{mm}$) as working electrode, a platinum plate as counter-electrode, and a saturated calomel electrode (SCE) with an agar-agar-plug in a Luggin capillary with a diaphragm as reference electrode was used. Measurements were carried out in N,N-dimethylformamide (anhydrous, SIGMA-ALDRICH) containing 0.1 M Bu₄NPF₆ (FLUKA) using a scan rate of $dE/dt=1\,\mathrm{V\,s^{-1}}$. The data is given in reference to the ferrocene redox couple (Fc/Fc⁺) which was used as external standard.
- 2.1.6. OLED Preparation. For the OLED preparation, ITO-coated glass substrates were used which were obtained from Optrex Europe GmbH (sheet resistance 20 Ohm/□; luminance area = 4 mm²). Before preparation, the ITO-glass substrates were cleaned via ultrasonic bath. The first hole injection layer was applied by spin-coating

a water-based dispersion of polyethylenedioxythiophene/polystyrene sulfonic acid (Clevios CH8000; Heraeus Holding GmbH). The layer was dried at 130° C for five minutes. As a hole-transporting layer, Interlayer 1 (Merck KGaA) was coated on the substrate. This is followed by a spin-coating process of the emitting polymer blend which was dissolved in toluene for 24 hours and filtered through a syringe filter with pore size of $0.2 \, \mu \text{m}$ before preparation. The blend consists of emitter 13, the wideband gap small molecule CoH-001 and the electron-transporting polymer 9a/b-12a/b. The wideband gap small molecule and the electron-transporting polymer 9a/b-12a/b were added with $41.7 \, \text{wt}\%$ while the emitter $13 \, \text{was}$ added with $16.7 \, \text{wt}\%$.

After the spin-coating process, another drying process was done at 110°C for 10 minutes to completely remove the solvent. The cathode (5 nm Ba and 150 nm Al) was deposited by a thermal evaporation process under high vacuum. The preparation was done in a glove box under nitrogen. For OLED characterization, luminance-voltage plots, efficiency-voltage plots, and electroluminescence spectra were measured with a Konica Minolta Camera CS2000. The electroluminescence was measured with a Diode-Array Spectrometer EPP 2000 from Stella Net. Inc.

2.1.7. Monomer Synthesis

2-(3-Bromo-Phenyl)-4,6-Diphenyl-[1,3,5]-Triazine (3a, $R_1 = H$). 60,59 g (0,454 mol) aluminium trichloride was exhibited. After the addition of 9,9 mL (0,136 mol) thionylchloride, 60 mL (0,454 mol) 3-bromobenzoylchloride, and 98,4 mL benzonitrile, the chemicals were dissolved in 800 mL 1,2-dichlorobenzene. The mixture was stirred for 20 hours at 100° C. After 1 hour, 48,61 g (0,909 mol) ammonium chloride was added to the reaction. After cooling to room temperature, the reaction mixture was poured into 3 L methanol and stirred for 45 minutes. The solid product was filtered and washed with hot ethanol. After drying under reduced pressure at 60° C 36,69 g (20% yield), a solid white product was obtained.

¹H-NMR (500 MHz, THF-d₈, δ): 8,93 (s, 1H, aromatic); 8,80 (d, 5H, aromatic, J = 6,83); 7,80 (d, 1H, aromatic, J = 7,08); 7,59 (m, 6H, aromatic); 7,53 (t, 1H, aromatic, J = 8,06).

2,4-Diphenyl-6-(4'-Vinyl-Biphenyl-3-yl)-[1,3,5]-Triazine (5a). 1,16 g (0,003 mol) (3a), 0,74 g (0,005 mol) 4-vinylphenylboronic acid (4) and 0,02 g (0,02 mmol) tetrakis(triphenylphosphine)palladium(0) were dissolved in 45 mL THF, and after the addition of 30 mL 1 M sodium carbonate solution, the mixture was stirred for 24 hours at reflux. After cooling to room temperature, the mixture was filtered over celite, and diluted with ethyl acetate. The mixture was washed with water three times, and the solvent of the organic layers was removed under reduced pressure. A recrystallisation in chloroform/ethanol (1:2) yielded 0,75 g (61%) of the pure product.

¹H-NMR (500 MHz, CDCl₃, δ): 9,01 (s, 1H, aromatic); 8,78 (m, 5H, aromatic); 7,85 (d, 1H, aromatic, J = 8,30);

7,73 (d, 2H, aromatic, J = 6,34); 7,63 (m, 9H, aromatic); 6,80 (dd, 1H, CH₂=CHAr, J = 10,99, J = 17,58); 5,85 (d, 1H, CH₂=CHAr trans, J = 17,58); 5,32 (d, 1H, CH₂=CHAr cis, J = 10,99).

 13 C-NMR (125 MHz, CD₂Cl₃, δ): 171,65 (2, -C=N-); 171,5 (1, -C=N-); 141,2 (1, C4); 140,2 (1, C4); 137,0 (1, C₄); 136,8 (1, C₄); 136,4 (1, =CH₂); 136,2 (1, C₄); 132,5 (2, =CH-); 131,0 (1, =CH-); 129,1 (1, =CH-); 129,0 (4, =CH-); 128,7 (4, =CH-); 127,9 (1, =CH-); 127,4 (3, =CH-); 126,8 (2, =CH-); 114,1 (1, CH₂).

Elemental Analysis. calcd. for $C_{29}H_{21}N_3$ (MW 411,51 g mole⁻¹): C: 84,65; H: 5,14; N: 10,21; found: C: 85,38; H: 5,16; N: 10,18.

2-(3-Bromo-Phenyl)-4,6-Bis-(4-Tert-Butyl-Phenyl)-[1,3,5]-Triazine (3a, R_1 = Tert.-Butyl). 1,67 g (0,013 mol) aluminium trichloride was exhibited. After the addition of 5,3 mL (0,0314 mol) 4-tert-butylbenzonitrile, 1,7 mL (0,0126 mol) 3-bromobenzoylchloride, and 0,3 mL (0,0038 mol) thionylchloride, the chemicals were dissolved in 25 mL 1,2-dichlorobenzene. The mixture was stirred for 20 hours at 100°C. After 1 hour, 1,3 g (0,025 mol) ammonium chloride was added to the reaction.

After cooling to room temperature, the reaction mixture was poured into 100 mL methanol and stirred for 45 minutes. The solid product was filtered and washed with hot ethanol. After drying under reduced pressure at 60°C, we yielded 2,98 g (48%) of a solid white product.

¹H-NMR (500 MHz, CDCl₃, δ): 8,88 (s, 1H, aromatic); 8,67 (m, 5H, aromatic); 7,72 (d, 1H, aromatic, J = 8,05); 7,60 (d, 4H, aromatic, J = 8,55); 7,44 (t, 1H, aromatic, J = 8,05); 1,41 (s, 18H, CH₃=CHAr, J = 18,0).

2,4-Bis-(4-Tert-Butyl-Phenyl)-6-(4'-Vinyl-Biphenyl-3-yl)-[1,3,5]-Triazine (8a). 2,0 g (0,004 mol) (3a, R_1 = Tert.-Butyl), 0,89 g (0,006 mol) 4-vinylphenylboronic acid (4) and 0,05 g (0,04 mmol) tetrakis(triphenylphosphine)palladium(0) were dissolved in 54 mL THF, and after the addition of 26 mL 1 M sodium carbonate solution, the mixture was stirred for 24 hours at reflux. After cooling to room temperature, the mixture was filtered over celite, and ethyl acetate was added. The mixture was washed with water three times, and the solvent of the organic layers was removed under reduced pressure. A recrystallisation in chloroform/ethanol (1:2) yielded 0,85 g (41%) of the pure product.

¹H-NMR (500 MHz, CDCl₃, δ): 9,00 (s, 1H, aromatic); 8,74 (d, 1H, aromatic, J = 6,59); 8,70 (d, 4H, aromatic, J = 4,88); 7,83 (d, 1H, aromatic, J = 7,56); 7,72 (d, 2H, aromatic, J = 7,80); 7,61 (m, 7H, aromatic); 6,80 (dd, 1H, CH₂=CHAr, J = 10,98, 17,58); 5,84 (d, 1H, CH₂=CHAr, trans, J = 17,58); 5,31 (d, 1H, CH₂=CHAr, cis, J = 10,98).

¹³C-NMR (125 MHz, CD₂Cl₃, δ): 171,5 (2, -C=N-); 171,3 (1, -C=N-); 156,0 (2, C₄); 141,1 (1, C₄); 140,2 (1, C₄); 137,0 (1, C₄); 136,9 (1, CH₂); 136,4 (1, =CH₂); 133,6 (2, C₄); 130,8 (1, =CH-); 129,1 (1, =CH-); 128,8 (4, =CH-); 127,8 (1, =CH-); 127,4 (3, =CH-); 126,8 (2, =CH-); 125,6 (4, =CH-); 114,1 (1, -CH₂); 35,1 (2, -C-CH₃); 31,2 (6, -CH₃).

Elemental Analysis. calcd. for $C_{37}H_{37}N_3$ (MW 523,73 g mole⁻¹): C: 84,86; H: 7,12 N: 8,02; found: C: 84,94; H: 7,34; N: 8,02.

2-(3-Bromo-Phenyl)-4,6-Bis-(4-Ethyl-Phenyl)-[1,3,5]-Triazine (3a, R₁ = Ethyl). 1,21 g (0,018 mol) aluminium trichloride was exhibited. After the addition of 2,6 mL (0,038 mol) 4-ethylbenzonitrile, 1,2 mL (0,018 mol) 3-bromobenzoylchloride, and 0,2 mL (0,0054 mol) thionylchloride, the chemicals were dissolved in 40 mL 1,2-dichlorobenzene. The mixture was stirred for 20 hours at 100°C. After 1 hour, 0,79 g (0,036 mol) ammonium chloride was added to the reaction. After cooling to room temperature, the reaction mixture was poured into 10 mL methanol and stirred for 45 minutes. The solid product was filtered and washed with hot ethanol. After drying under reduced pressure at 60°C, we yielded 1,79 g (45%) of a solid white product.

¹H-NMR (500 MHz, CDCl₃, δ): 8,88 (s, 1H, aromatic); 8,69 (d, 1H, aromatic, J = 7,82); 8,66 (d, 4H, aromatic, J = 5,13); 7,72 (d, 1H, aromatic, J = 7,81); 7,44 (t, 1H, aromatic); 7,41 (d, 4H, aromatic, J = 8,06); 2,78 (q, 4H, CH₂=CH₃, J = 7,57); 1,32 (t, 6H, CH₃=CH₂).

2,4-Bis-(4-Ethyl-Phenyl)-6-(4'-Vinyl-Biphenyl-3-yl)-[1,3,5]-Triazine (7a). 1,7 g (0,0038 mol) (3a, R_1 = Ethyl), 0,94 g (0,0064 mol) 4-vinylphenylboronic acid (4) and 0,04 g (0,026 mmol) tetrakis(triphenylphosphine)palladium(0) were dissolved in 65 mL THF, and after the addition of 38 mL 1 M sodium carbonate solution, the mixture was stirred for 24 hours at reflux. After cooling to room temperature, the mixture was filtered over celite, and ethyl acetate was added. The mixture was washed with water three times, and the solvent of the organic layers was removed under reduced pressure. A recrystallisation in chloroform/ethanol (1:2) and a column chromatography in hexane/toluene (4:1) yielded 0,52 g (29%) of the pure product.

¹H-NMR (500 MHz, CDCl₃, δ): 8,98 (s, 1H, aromatic); 8,74 (d, 1H, aromatic, J = 7,80); 8,69 (d, 1H, aromatic, J = 6,59); 7,82 (d, 1H, aromatic, J = 6,59); 7,82 (d, 1H, aromatic, J = 6,59); 7,63 (t, 1H, aromatic, J = 7,57); 7,57 (d, 2H, aromatic, J = 8,30); 7,40 (d, 4H, aromatic, J = 8,06); 6,79 (dd, 1H, CH₂=CHAr, J = 10,98, J = 17,57); 5,84 (d, 1H, CH₂=CHAr, trans, J = 17,57); 5,31 (d, 1H, CH₂=CHAr, cis, J = 10,98); 2,78 (q, 2H, CH₂, J = 7,65); 1,32 (t, 3H, CH₃, J = 7,57).

 $^{13}\text{C-NMR}$ (125 MHz, CD₂Cl₃, δ): 171,5 (2, -C=N-); 171,3 (1, -C=N-); 149,3 (2, C₄); 141,1 (1, C₄); 140,2 (1, C₄); 137,0 (1, C₄); 136,9 (1, CH₂); 136,4 (1, =CH₂); 133,8 (2, C₄); 130,8 (1, =CH-); 129,1 (4, =CH-); 129,0 (1, =CH-); 128,2 (4, =CH-); 127,8 (1, =CH-); 127,4 (2, =CH-); 127,4 (2, =CH-); 126,7 (1, =CH-); 114,1 (1, -CH₂); 29,0 (2, -CH₂-); 15,4 (2, -CH₃).

Elemental Analysis. calcd. for $C_{33}H_{29}N_3$ (MW 467,62 g mole⁻¹): C: 84,76; H: 6,25 N: 8,99; found: C: 84,36; H: 6,16; N: 8,91.

 $2\text{-}(3\text{-}Bromo\text{-}Phenyl)\text{-}4,6\text{-}di\text{-}p\text{-}Tolyl\text{-}[1,3,5]\text{-}Triazine}$ (3a, R_1 = Methyl). 1,63 g (0,012 mol) aluminium trichloride and 3,0 g (0,026 mol) p-tolunitrile were exhibited. After the addition of 1,6 mL (0,012 mol) 3-bromobenzoylchloride and 0,3 mL (0,0037 mol) thionylchloride, the chemicals were dissolved in 100 mL 1,2-dichlorobenzene. The mixture was stirred for 20 hours at 140°C. After 1 hour, 1,31 g (0,0244 mol) ammonium chloride was added to the reaction. After cooling to room temperature, the solvent was completely removed, and the product was isolated by column chromatography in hexane/toluene (8:1), which yielded 1,23 g (24%) of a solid white product.

¹H-NMR (500 MHz, CDCl₃, δ): 8,87 (s, 1H, aromatic); 8,69 (d, 1H, aromatic, J = 7,81); 8,64 (d, 4H, aromatic, J = 6,59); 7,72 (d, 1H, aromatic, J = 8,79); 7,44 (t, 1H, aromatic, J = 7,81); 7,37 (d, 4H, aromatic, J = 8,06).

2,4-Di-p-Tolyl-6-(4'-Vinyl-Biphenyl-3-yl)-[1,3,5]-Triazine (**6a**). 1,0 g (0,0025 mol) (**3a**, $\mathbf{R}_1 = \mathbf{Methyl}$), 0,55 g (0,0037 mol) 4-vinylphenylboronic (**4**) acid and 0,02 g (0,017 mmol) tetrakis(triphenylphosphine)palladium(0) were dissolved in 50 mL THF, and after the addition of 25 mL 1 M sodium carbonate solution, the mixture was stirred for 24 hours at reflux. After cooling to room temperature, the mixture was filtered over celite, and ethyl acetate was added. The mixture was washed with water three times, and the solvent of the organic layers was removed under reduced pressure. Column chromatography with hexane/toluene (4:1) gave 0,73 g (67%) of the pure white powder product.

¹H-NMR (500 MHz, CDCl₃, δ): 9,04 (s, 1H, aromatic); 8,76 (d, 1H, aromatic, J = 7,81); 8,70 (d, 4H, aromatic, J = 8,30); 7,89 (d, 1H, aromatic, J = 8,30); 7,75 (d, 2H, aromatic, J = 6,59); 7,65 (t, 1H, aromatic, J = 7,81); 7,58 (d, 2H, aromatic, J = 8,31); 7,39 (d, 4H, aromatic, J = 8,06); 6,79 (dd, 1H, CH₂=CHAr, J = 10,98, J = 17,82); 5,86 (d, 1H, CH₂=CHAr, trans, J = 17,82); 5,26 (d, 1H, CH₂=CHAr, cis, J = 10,98); 2,46 (s, 6H, CH₂=CH₃).

Elemental Analysis. calcd. for $C_{31}H_{25}N_3$ (MW 439,57 g mole⁻¹): C: 84,71; H: 5,73 N: 9,56; found: C: 84,72; H: 5,87; N: 9,32.

2-(4-Bromo-Phenyl)-4,6-Diphenyl-[1,3,5]-Triazine (3b). 60,59 g (0,454 mol) aluminium trichloride was exhibited. After the addition of 9,9 mL (0,136 mol) thionylchloride, 60 mL (0,454 mol) 3-bromobenzoylchloride and 98,4 mL benzonitrile, the chemicals were dissolved in 800 mL 1,2-dichlorobenzene. The mixture was stirred for 20 hours at 100°C. After 1 hour, 48,61 g (0,909 mol) ammonium chloride was added to the reaction. After cooling to room temperature, the reaction mixture was poured into 3 L methanol and stirred for 45 minutes. The solid product was filtered and washed with hot ethanol. After drying under reduced pressure at 60°C, we yielded 36,69 g (20%) of a solid white product.

¹H-NMR (500 MHz, CDCl₃, δ): 8,77 (d, 4H, aromatic, J = 6,84); 8,65 (d, 2H, aromatic, J = 8,06); 7,71 (d, 2H, aromatic, J = 8,78); 7,60 (m, 6H, aromatic).

2,4-Diphenyl-6-(4'-Vinyl-Biphenyl-4-yl)-[1,3,5]-Triazine (5b). 1,16 g (0,003 mol) (3b), 0,74 g (0,005 mol) 4-vinyl-phenylboronic acid (4) and 0,02 g (0,02 mmol) tetrakis (triphenylphosphine)palladium(0) were dissolved in 45 mL THF, and after the addition of 30 mL 1 M sodium carbonate solution, the mixture was stirred for 24 hours at reflux. After cooling to room temperature, the mixture was filtered over celite, and ethyl acetate was added. The mixture was washed with water three times, and the solvent of the organic layers was removed under reduced pressure. A recrystallisation in chloroform/ethanol (1:2) yielded 0,75 g (61%) of the pure product.

¹H-NMR (500 MHz, CDCl₃, δ): 8,85 (d, 2H, aromatic, J = 8,54); 8,80 (d, 4H, aromatic, J = 4,89); 7,82 (d, 2H, aromatic, J = 8,44); 7,69 (d, 2H, aromatic, J = 8,30); 7,61 (m, 6H, aromatic); 7,55 (d, 2H, aromatic, J = 8,30); 6,78 (dd, 1H, CH₂=CHAr, J = 10,98, 17,58); 5,69 (d, 1H, CH₂=CHAr, trans, J = 17,58); 5,32 (d, 1H, CH₂=CHAr, cis, J = 10,98).

 13 C-NMR (125 MHz, CD₂Cl₃, δ): 171,6 (2, -C=N-); 171,3 (1, -C=N-); 144,6 (1, C₄); 139,6 (1, C₄); 137,3 (1, C₄); 136,3 (1, =CH₂); 136,3 (2, C₄); 135,2 (1, C₄); 132,5 (2, =CH₂); 129,5 (2, =CH-); 129,0 (4, =CH-); 128,6 (4, =CH-); 127,4 (2, =CH-); 127,1 (2, =CH-); 126,8 (2, =CH-); 114,1 (1, CH₂).

Elemental Analysis. calcd. for $C_{29}H_{21}N_3$ (MW 411,51 g mole⁻¹): C: 84,65; H: 5,14 N: 10,21; found: C: 84,56; H: 5,16; N: 9,84.

2-(4-Bromo-Phenyl)-4,6-Bis-(4-Tert-Butyl-Phenyl)-[1,3,5]-Triazine (3b, R₁ = Tert.-Butyl). 1,67 g (0,013 mol) aluminium trichloride, 5,0 g (0,031 mol) 4-tert-butylbenzonitrile, 2,76 g (0,126 mol) 4-bromobenzoylchloride were exhibited. After the addition of 0,3 mL (0,0038 mol) thionylchloride, the chemicals were dissolved in 25 mL 1,2-dichlorobenzene. The mixture was stirred for 20 hours at 100°C. After 1 hour, 1,34 g (0,025 mol) ammonium chloride was added to the reaction. After cooling to room temperature, the reaction mixture was poured into 500 mL methanol and stirred for 45 minutes. The solid product was filtered and dried under reduced pressure at 60°C. The white product powder yielded 3,10 g (21%).

¹H-NMR (500 MHz, THF-d₈, δ): 8,64 (m, 4H, aromatic); 7,68 (d, 2H, aromatic, J = 8,54); 7,58 (d, 4H, aromatic, J = 8,55); 1,40 (s, 18H, (CH₃)₂).

2,4-Bis-(4-Tert-Butyl-Phenyl)-6-(4'-Vinyl-Biphenyl-4-yl)-[1,3,5]-Triazine (8b). 2,0 g (0,004 mol) (3b, R_1 = Tert.-Butyl), 0,89 g (0,006 mol) 4-vinylphenylboronic acid (4) and 0,05 g (0,04 mmol) tetrakis(triphenylphosphine)palladium(0) were dissolved in 54 mL THF, and after the addition of 26 mL 1 M sodium carbonate solution, the mixture was stirred for 24 hours at reflux. After cooling to room temperature, the mixture was filtered over celite, and ethyl acetate was added. The mixture was washed with water three times, and the solvent of the organic layers was removed under reduced pressure. A recrystallisation in chloroform/ethyl acetate yielded 1,60 g (76%) of the pure product.

¹H-NMR (500 MHz, CDCl₃, δ): 8,82 (d, 2H, aromatic, J = 8,30); 8,69 (d, 4H, aromatic, J = 8,31); 7,79 (d, 2H, aromatic, J = 8,30); 7,67 (d, 2H, aromatic, J = 8,30); 7,60 (d, 4H, aromatic, J = 8,30); 6,78 (dd, 1H, CH₂=CHAr, J = 10,98, 17,58); 5,83 (d, 1H, CH₂=CHAr, trans, J = 17,58); 5,31 (d, 1H, CH₂=CHAr, cis, J = 10,99).

 $^{13}\text{C-NMR} \ (125 \ \text{Mhz}, \text{CDCl}_3, \delta) : 171,5 \ (2, -\text{C=N-}); \ 171,1 \ (1, -\text{C=N-}); \ 156,0 \ (2, \text{C}_4); \ 144,4 \ (1, \text{C}_4); \ 139,8 \ (1, \text{C}_4); \ 137,3 \ (1, \text{C}_4); \ 136,3 \ (1, \text{CH}_2); \ 135,4 \ (1, \text{C}_4); \ 133,7 \ (2, \text{C}_4); \ 129,4 \ (2, -\text{CH-}); \ 128,8 \ (4, -\text{CH-}); \ 127,4 \ (2, -\text{CH-}); \ 127,0 \ (2, -\text{CH-}); \ 126,8 \ (2, -\text{CH-}); \ 125,6 \ (4, -\text{CH-}); \ 114,3 \ (1, -\text{CH}_2); \ 35,1 \ (2, -\text{C-CH}_3); \ 31,2 \ (6, -\text{CH}_3).$

Elemental Analysis. calcd. for $C_{37}H_{37}N_3$ (MW 523,73 g mole⁻¹): C: 84,86; H: 7,12 N: 8,02; found: C: 86,13; H: 7,34; N: 7,38.

2-(4-Bromo-Phenyl)-4,6-di-p-Tolyl-[1,3,5]-Triazine (3b, R_1 = Methyl). 1,2 g (0,009 mol) aluminium trichloride, 1,99 g (0,009 mol) 4-bromobenzoylchloride were exhibited. After the addition of 2,3 mL (0,02 mol) p-tolunitrile and 0,2 mL (0,0027 mol) thionylchloride, the chemicals were dissolved in 25 mL 1,2-dichlorobenzene. The mixture was stirred for 20 hours at 130°C. After 1 hour, 0,97 g (0,018 mol) ammonium chloride was added to the reaction. After cooling to room temperature, the reaction mixture was poured into 20 mL methanol and stirred for 45 minutes. The solid product was filtered and dried under reduced pressure at 60°C. The white product powder yielded 1,10 g (29%).

¹H-NMR (500 MHz, CDCl₃, δ): 8,62 (m, 6H, aromatic); 7,69 (d, 2H, aromatic, J = 8,54); 7,37 (d, 4H, aromatic, J = 8,06); 2,48 (s, 6H, CH₂=CH₃).

2,4-Di-p-Tolyl-6-(4'-Vinyl-Biphenyl-4-yl)-[1,3,5]-Triazine (**6b**). 1,0 g (0,0024 mol) (**3b**, **R**₁ = **Methyl**), 0,59 g (0,004 mol) 4-vinylphenylboronic acid (**4**) and 0,02 g (0,02 mmol) tetrakis(triphenylphosphine)palladium(0) were dissolved in 50 mL THF, and after the addition of 24 mL 1 M sodium carbonate solution, the mixture was stirred for 24 hours at reflux. After cooling to room temperature, the mixture was filtered over celite, and ethyl acetate was added. The mixture was washed with water three times, and the solvent of the organic layers was removed under reduced pressure. A column chromatography in hexane/toluene (8:1) yielded 0,41 g (39%) of the pure white product.

¹H-NMR (500 MHz, CDCl₃, δ): 8,83 (d, 2H, aromatic, J = 8,54); 8,68 (d, 4H, aromatic, J = 8,06); 7,81 (d, 2H, aromatic, J = 8,30); 7,69 (d, 2H, aromatic, J = 8,05); 7,55 (d, 2H, aromatic, J = 8,30), 7,38 (d, 4H, aromatic, J = 8,06); 6,78 (dd, 1H, CH₂=CHAr, J = 10,98, 17,58); 5,84 (d, 1H, CH₂=CHAr, trans, J = 17,58); 5,32 (d, 1H, CH₂=CHAr, cis, J = 10,99); 2,49 (s, 6H, CH₂=CH₃).

 $^{13}\text{C-NMR}$ (125 MHz, CD₂Cl₃, δ): 171,5 (2, -C=N-); 171,1 (1, -C=N-); 144,4 (1, C₄); 143,0 (2, C₄); 139,7 (1, C₄); 137,3 (1, C₄); 136,3 (1, =CH₂); 135,4 (1, C₄); 133,7 (2, C₄); 129,4 (2, =CH-); 129,4 (4, =CH-); 128,9 (4, =CH-); 127,4 (2, =CH-); 127,0 (2, =CH-); 126,8 (2, =CH-); 114,3 (1, -CH₂); 21,8 (2, -CH₃).

Elemental Analysis. calcd. for $C_{31}H_{25}N_3$ (MW 439,57 g mole⁻¹): C: 84,71; H: 5,73 N: 9,56; found: C: 85,10; H: 5,84; N: 9,48.

2-(4-Bromo-Phenyl)-4,6-Bis-(4-Ethyl-Phenyl)-[1,3,5]-Triazine (3b, R₁ = Ethyl). 1,2 g (0,009 mol) aluminium trichloride and 1,99 g (0,009 mol) 4-bromobenzoylchloride were exhibited. After the addition of 2,3 mL (0,02 mol) 4-ethylbenzonitrile and 0,2 mL (0,0027 mol) thionylchloride, the chemicals were dissolved in 40 mL 1,2-dichlorobenzene. The mixture was stirred for 20 hours at 130°C. After 1 hour, 0,97 g (0,018 mol) ammonium chloride was added to the reaction. After cooling to room temperature, the reaction mixture was poured into 20 mL methanol and stirred for 45 minutes. The solid product was filtered, washed with hot ethanol and dried under reduced pressure at 60°C. The white product powder yielded 0,87 g (22%).

¹H-NMR (500 MHz, CDCl₃, δ): 8,65 (m, 6H, aromatic); 7,70 (d, 2H, aromatic, J = 8,79); 7,40 (d, 4H, aromatic, J = 8,55); 2,78 (q, 4H, CH₂=CH₃, J = 7,56); 1,32 (t, 6H, CH₃=CH₂, J = 7,56).

2,4-Bis-(4-Ethyl-Phenyl)-6-(4'-Vinyl-Biphenyl-4-yl)-[1,3,5]Triazine (7b). 0,8 g (0,0018 mol) (3b, $R_1 = Ethyl$), 0,4 g (0,0027 mol) 4-vinylphenylboronic acid (4) and 0,01 g (0,012 mmol) tetrakis(triphenylphosphine)palladium(0) were dissolved in 40 mL THF, and after the addition of 18 mL 1 M sodium carbonate solution, the mixture was stirred for 24 hours at reflux. After cooling to room temperature, the mixture was filtered over celite, and ethyl acetate was added. The mixture was washed with water three times, and the solvent of the organic layers was removed under reduced pressure. A column chromatography in hexane/toluene (4:1) yielded 0,5 g (59%) of the pure white product.

¹H-NMR (500 MHz, CDCl₃, δ): 8,81 (d, 2H, aromatic, J = 8,54); 8,69 (d, 4H, aromatic, J = 8,30); 7,78 (d, 2H, aromatic, J = 8,30); 7,67 (d, 2H, aromatic, J = 8,05); 7,52 (d, 2H, aromatic, J = 8,06); 6,78 (dd, 1H, CH₂=CHAr, J = 10,75, 17,58); 5,82 (d, 1H, CH₂=CHAr, trans, J = 17,58); 5,30 (d, 1H, CH₂=CHAr, cis, J = 10,74); 2,77 (q, 4H, CH₂=CH₃, J = 7,57); 1,31 (t, 6H, J = 7,81).

 $^{13}\text{C-NMR} \ (125\,\text{MHz}, \ \text{CD}_2\text{Cl}_3, \ \delta); \ 171,4 \ (2, \ -\text{C=N-}); \\ 171,0 \ (1, -\text{C=N-}); \ 149,2 \ (2, \ \text{C}_4); \ 144,3 \ (1, \ \text{C}_4); \ 139,7 \ (1, \ \text{C}_4); \\ 137,2 \ (1, \ \text{C}_4); \ 136,3 \ (1, \ -\text{CH}_2); \ 13,4 \ (1, \ \text{C}_4); \ 133,9 \ (2, \ \text{C}_4); \\ 129,4 \ (2, -\text{CH-}); \ 129,0 \ (4, -\text{CH-}); \ 128,1 \ (4, -\text{CH-}); \ 127,3 \ (2, -\text{CH-}); \ 127,0 \ (2, -\text{CH-}); \ 126,7 \ (2, -\text{CH-}); \ 114,3 \ (1, -\text{CH}_2); \\ 29,0 \ (2, -\text{CH}_2-); \ 15,4 \ (2, -\text{CH}_3). \\ \end{cases}$

Elemental Analysis. Calcd. for $C_{33}H_{29}N_3$ (MW 467,26 g mole⁻¹): C: 84,76; H: 6,25 N: 8,99; found: C: 84,97; H: 6,54; N: 8,85.

2.1.8. General Polymerization Procedure. The polymerizations were carried out in a glove box under an argon atmosphere. For the free radical polymerization, N,N-azobisisobutyronitrile in a concentration of 2 mol% was used. The monomers and the initiator were dissolved in

 $R_1 = H$; methyl; ethyl; tert-butyl groups

FIGURE 1: General structure of the electron-transporting polystyrenes **9a/b–12a/b** with 2,4,6-triphenyl-1,3,5-triazine side groups (a: meta; b: para).

freshly distilled tetrahydrofuran. The solution was stirred for 72 hours at 50°C. For purification, the polymers **9a/b–12a/b** were diluted in THF, precipitated in methanol/diethyl ether several times, and dried under reduced pressure at 60°C.

3. Results and Discussion

3.1. Synthesis of Monomers and Polymers. As a general structure for the electron-transporting polymers 9a/b-12a/b, we used a polystyrene with 2,4,6-triphenyl-1,3,5-triazine side groups as it is shown in Figure 1.

The styryl group is linked to the 2,4,6-triphenyl-1,3,5-triazine in two different ways—in meta- and paraposition. Furthermore, the 4- and 6-phenyl rings are substituted in paraposition by different alkyl groups R1 (H, methyl, ethyl and tert.-butyl). The aim of this work is to study the influence of these structure modifications on the solubility, the film forming properties, thermal properties and on OLED performance.

A typical phosphorescent green emitter 13 was used in combination with a small molecule cohost CoH-001; both were delivered from Merck KGaA, Darmstadt and used as received.

In order to synthesise the triazine core structure shown in Figure 1, we used the already known nitrile route, which is described by Behl and Zentel [15]. A general scheme for the nitrile route is shown in Figure 2.

$$CN$$
 $+$
 $AlCl_3; SOCl_2$
 $1, \overline{2\text{-dichlorobenzene}}$
 R_1
 R_1
 R_2
 R_3

 $R_1 = H$; methyl; ethyl; tert-butyl groups

FIGURE 2: Nitrile route for building up the triazine core (a: 3-bromo-, b: 4-bromo-derivate).

The first step is the triazine formation which is done via a nitrile group exchange catalyzed by aluminium trichloride. The reactants are a bromosubstituted benzoic acid chloride and a nitrile with the appropriate side groups. As benzoic acid we used the 3-bromo (2a) and the 4-bromo derivative (2b) in order to get the different linkage for the styryl substitution in meta- or paraposition during the second step. For the building of the triazine core, the yields are often about 50% depending on the nitrile substituent used.

The second step is a Suzuki coupling of the triazine bromide (3a/b) with 4-vinylphenylboronic acid (4). This reaction step is shown in Figure 3. For this reaction, yields of up to 80% were reached.

Table 1 shows the used nitriles and the yields for the twostep monomer synthesis.

The polymerizations of the synthesized monomers were done via a free radical mechanism with AIBN as initiator under an inert atmosphere. The general polymer structure is shown in Figure 1. The monomer was dissolved in freshly distilled tetrahydrofuran (THF) and stirred at 60°C for three days. Afterwards, multiple precipitations in methanol/diethyl ether were done to separate monomer residue, low molecular fractions, and other impurities. After purification, the yields were about 80%.

Table 2 shows the yields of the synthesized polymers to the corresponding monomers from Table 1 as well as selected analytical data for the polymers.

The molecular weights and their distribution of the polymers were characterized by GPC measurement. DSC measurements were performed to determine the thermal behavior and the glass transition for which the data is listed in Table 2. All polymers show a good solubility in toluene and chlorinated solvents such as 1,2-dichlorobenzene. For device preparation, it was possible to spin-coat good films from toluene.

In regard to the analytical data, there is an influence on the molecular weight and the glass transition temperature depending on the inserted substituent. The weight average molecular weight lies in the range of $23 * 10^3$ and $100 * 10^3$ g/mol. The para tert.-butyl substituted polymer (12b) shows with $100 * 10^3$ g/mol the highest molecular weight, while the para methyl substituted polymer (10b) shows with $23 * 10^3$ g/mol the lowest molecular weight. The nonsubstituted structures both show an average molecular weight around $65 * 10^3$ g/mol.

The methyl and ethyl substituted polymers 10a/b and 11a/b show a lower molecular weight while the tert.-butyl substituted polymers 12a/b show a higher molecular weight in comparison to the nonsubstituted structure 9a/b. This effect can be explained by the inserted alkyl groups for the polymers 10a/b and 11a/b. Methyl or ethyl groups can alloy chain transfer with the benzyl hydrogens. Three mesomeric structures that consist of a more or less stable state can be built up. These resonance structures lower the molecular weight. As for polymer 12a/b the tert.-butyl groups are stiff enough and do not build up mesomeric structures and therefore show a higher molecular weight.

For all polymers only glass transition temperatures (T_g) were observed by DSC. No further thermal effects such as melting or crystallization were seen. The results for the glass transition temperature show a division between meta- and paralinked polymers. The metalinked polymers have a lower T_g than the paralinked polymers. This effect can be explained by the stiffness of the different structures. The paralinked polymers have the ability to pack in a more compact way due to their side group while the packing of the metalinked polymers is hindered because of their twisted structure in regard to the polymer backbone. Behl and Zentel [15] found quite similar results for their vinyl-substituted 2,4,6triphenyl-1,3,5-triazine polymers compared to our styrylsubstituted analogues. The ethyl substituted polymers (11a and 11b) both show a lower T_g in comparison to the nonsubstituted structure (9a and 9b). Those flexible groups have the ability to twist within the structure and thus lower the glass transition temperature. In contrast to that, the tert.-butyl substituted polymers (12a and 12b) show

 $R_1 = H$ (5); methyl (6); ethyl (7); tertbutyl (8) groups

FIGURE 3: Introduction of styryl functionality by Suzuki coupling (a: meta; b: para).

TABLE 1: Overview of the yields and inserted nitriles for the synthesized monomers.

Number	Inserted nitrile	Inserted benzoic acid chloride	Overall yield (%)
5a	CN	3-bromobenzoic acid chloride	61
5b	CN	4-bromobenzoic acid chloride	26
6a	CN	3-bromobenzoic acid chloride	57
6b	CN	4-bromobenzoic acid chloride	67
7a	CN	3-bromobenzoic acid chloride	29
7b	CN	4-bromobenzoic acid chloride	59
8a	CN	3-bromobenzoic acid chloride	41
8b	CN	4-bromobenzoic acid chloride	55

an increase in T_g which can be explained by their more compact structure. A second reason could be the increasing molecular weight. For some polymers T_g still is dependent on the polymerization degree. A polymerization degree up to 50 is accepted for a correlation between T_g , and the polymerization degree while above 50 the glass transition

temperature is independent from the polymerization degree [16].

3.2. UV- and PL Spectra. Figures 4 and 5 show the UV-Vis spectra of the obtained polymers. In the UV-Vis spectra all polymers illustrate an absorption maximum

Inserted monomer	Polymer	GPC (10 ³ g/mol)		PDI	Glass transition	Yield (%)	UV-Vis maxima	PL maxima
		M_w	M_n	1101	temperature (°C)	11010 (70)	(nm)	(nm)
5a	9a	66,3	22,9	2,89	202	87	270	420
5b	9b	67,7	19,8	3,42	237	82	283	438
6a	10a	34,6	14,8	2,33	215	83	277	419
6b	10b	23,8	10,2	2,33	248	55	293	431
7a	11a	57,3	21,4	2,68	200	79	278	413
7b	11b	42,2	16,2	2,61	235	81	294	428
8a	12a	74,3	28,5	2,60	246	81	278	427
8b	12b	100,8	34,6	2,91	277	74	292	426

TABLE 2: Analytical data of the synthesized polymers.

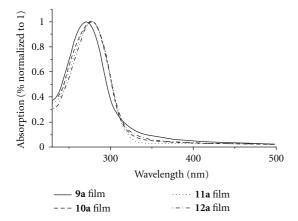


FIGURE 4: UV-spectra of metasubstituted polymer films **9a–12a** on silica glass.

between 270 nm and 300 nm. The metalinked polymers 9a–12a demonstrate absorption at about 275 nm while the paralinked polymers 9b–12b indicate absorption at about 300 nm. The nonsubstituted metalinked polymer 9a shows the lowest absorption maximum at 270 nm. The substituted metalinked polymers 10a–12a present shifted absorption maxima by about 7-8 nm. The nonsubstituted paralinked polymer 9b exhibits an absorption maximum at 283 nm. Substituted paralinked polymers 10b–12b show the furthest shift to higher wavelength absorption (around 10 nm). This bathochromic shift can be explained by the +I-effect of the alkyl groups. For larger alkyl groups especially in the case of paralinked polymers the +I-effect becomes stronger so that the furthest wavelength shift can be seen for the tert.-butyl substituted polymer 12b.

The nonsubstituted paralinked structure **9b** and the tert-butyl paralinked structure **12b** both show a shoulder at about 350 nm which could be explained by some aggregation effects of the alkyl structure. None of these effects could be found in the DSC measurements.

Figure 6 shows the photoluminescence spectra of the metalinked polymers 9a–12a while Figure 7 shows the photoluminescence spectra for the paralinked polymers 9b–12b. For the photoluminescence spectra, the excitation wavelength for all polymers was 300 nm. The emission maxima

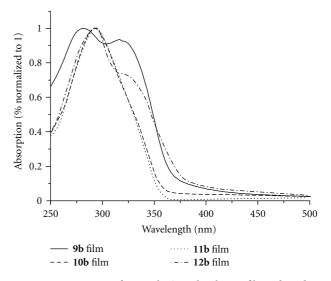


FIGURE 5: UV spectra of parasubstituted polymer films **9b–12b** on silica glass.

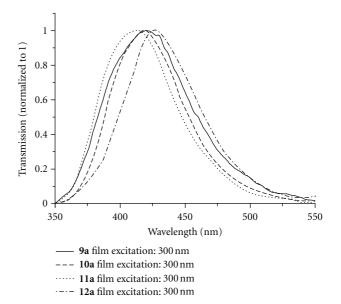


FIGURE 6: PL spectra of metapolymer films 9a-12a on silica glass.

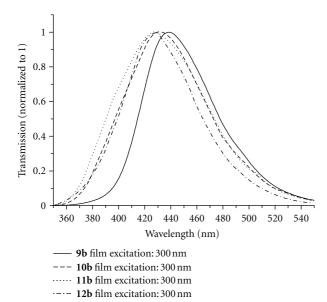


Figure 7: PL spectra of parapolymer films 9b–12b on silica glass.

are seen between 420 nm and 440 nm. The paralinked substituted polymers **9b–12b** show a higher emission wavelength maximum than their metalinked analogues. The highest difference between meta- and paralinked polymers of 18 nm is found for the nonsubstituted polymers **9a** and **9b**. With increasing alkyl substitution length these differences become smaller. In the case of tert.-butyl substituted polymers **12a** and **12b** there is no significant deflection anymore.

3.3. HOMO and LUMO Energy Levels. Table 3 shows an overview of the reduction potentials as well as the resultant LUMO energy levels. Since the oxidation potentials for the synthesized polymers all lie above +2 V, in regard to their expected HOMO levels that should lie below -6 eV, it was not possible to determine their HOMO levels with the CV equipment. Measurements in different solvents showed that the standard electrolyte was becoming oxidized before an oxidation of the polymer occurred. First, reduction behavior of the new polymers was investigated by applying the polymers as films on glass carbon electrodes. But in this case the ground electrolyte was reduced before the polymer or with the polymer, so that an exact determination of the LUMO levels was not possible. Therefore, CV measurements were carried out in dimethylformamide solutions with an extended reduction window to higher voltages of about +2.5 V. Because the polymers were not soluble in the used solvent N,N-dimethylformamide for CV measurements, their corresponding monomers were used instead. As Zeng et al. showed CV measurements for tris-phenyl-s-triazine finding a LUMO of -2.6 eV one can assume that the styryl group does not affect the LUMO level [17]. According to this, we estimated the monomer LUMO levels and equated them with the polymer LUMO levels in first approximation.

Figures 8 and 9 show the 1e⁻ transfer found in the CV measurement. While Figure 8 shows the metalinked monomers, Figure 9 shows the results for the paralinked

TABLE 3: LUMO energy levels and reduction potentials of corresponding monomers 5a/b-8a/b.

Monomer	Reduction peak potential ¹ (V)	LUMO ² (eV)
5a	-2,1	-2,7
5b	-2,1	-2,7
6b	-2,1	-2,7
7a	-2,2	-2,6
7b	-2,1	-2,7
8a	-2,2	-2,6
8b	-2,1	-2,7
1		

¹Peak potential converted to [Fc/Fc⁺] by adding 0,522 V. ²LUMO layer determined for [Fc/Fc⁺] by adding +4,8 eV.

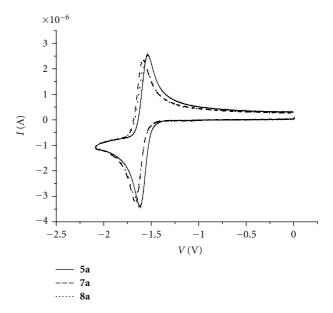


FIGURE 8: Cyclovoltammograms of monomers **5a–8a** with 1e⁻ transfer (reduction cycles).

monomers. Figures 8 and 9 show the first reduction peak measured up to $-2.0\,\mathrm{V}$ which is completely reversible. The reduction potential for the metalinked monomers 5a-8a is lower (about $0.05-0.07\,\mathrm{V}$) than their corresponding paralinked analogues 5b-8b. The reoxidation potential shows a more pronounced difference between metalinked monomers (at about $-1.6\,\mathrm{V}$) and paralinked (at about $-1.9\,\mathrm{V}$) monomers. The LUMO values can be estimated from the reduction peak potentials to around $-2.6--2.7\,\mathrm{eV}$, which should allow a quite efficient electron injection from the barium cathode into the emissive layer.

The whole reduction with the $2e^-$ transfer for the metalinked monomers is shown in Figure 10 and for the paralinked monomers in Figure 11. It is seen that the second reduction step (at -2,4 V) is nonreversible for the metalinked monomers 5a-8a. For these monomers a degradation product peak is seen in the reoxidation at about -0,5 V. In contrast to that the second reduction step (at -2,1 V) is nearly reversible for the paralinked monomers

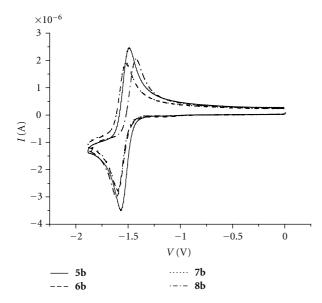


FIGURE 9: Cyclovoltammograms of monomers 5b–8b with 1e⁻ transfer (reduction cycles).

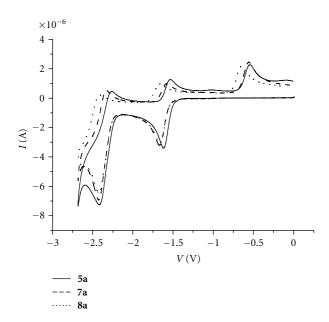


FIGURE 10: Cyclovoltammograms of monomers **5a–8a** with 1e⁻ and 2e⁻ transfer (reduction cycles).

5b–8b. Summarizing, all monomers and, in first approximation, their corresponding polymers also exhibit a reversible first reduction step at -2.1--2.2 V. The second reduction step is only reversible for the paralinked monomers, whereas the metalinked monomers show nonreversibility during the second reduction step.

3.4. OLED Design. Figure 12 shows the OLED stack used for testing the new electron-transporting polymers 9a/b-12a/b.

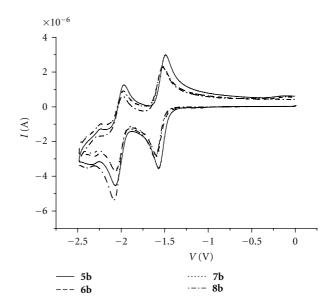


FIGURE 11: Cyclovoltammograms of monomers **5b–8b** with 1e⁻ and 2e⁻ transfer (reduction cycles).

All the blend components (polymers 9a/b–12a/b; 13; CoH-001) (41.7 wt%; 16.7 wt%; 41.7 wt%) were tested in a green single emitting layer.

As a transparent anode material, a glass substrate coated with indium-tin-oxide from Optrex Europe GmbH was used. As hole injection layer PEDOT/PSS (Clevios CH8000 from Heraeus Holding GmbH) was used. Furthermore a polymeric Interlayer 1 which is provided from Merck KGaA was deposited on top of the PEDOT. This layer improves hole transport, blocks electrons, and separates the phosphorescent-emitting layer from the PEDOT layer. The emitting layer is made out of a blend system of the new electron-transporting polymers 9a/b-12a/b, the wideband gap cohost CoH-001, and the emitter 13. Finally a metal cathode, consisting of barium/aluminium, was deposited in vacuum

Figure 13 shows the different energy levels of the materials used in this OLED. The second hole injection layer, Interlayer 1, has a HOMO energy level of -5,1 eV from which the holes are directly injected into the emitter molecule 13 with a HOMO energy level of -5,1 eV. The electrons are injected from the inner barium cathode (-2,5 eV) to the LUMO of the new polymers 9a/b-12a/b of about -2,6 eV. The wideband gap material CoH-001 exhibits a HOMO energy level of -6,2 eV and a LUMO energy level of -1,8 eV. According to these energy levels, one can assume that CoH-001 does not contribute significantly to the charge transport in the blend system; however, it was found that it plays an important role to an optimized blend morphology which finally leads to an improved OLED performance.

In the following, we report the results obtained with the new electron-transporting polymers 9a/b-12a/b in the OLED stack and discuss them depending on the different polymer structures in regard to the alkyl substitution and to the kind of linkage to the polystyrene backbone. Figure 14

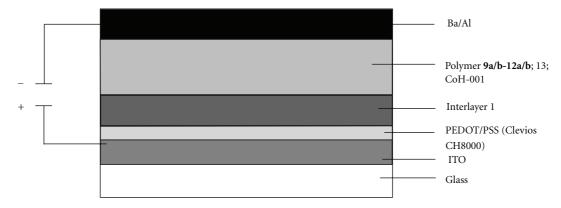


FIGURE 12: General OLED stack.

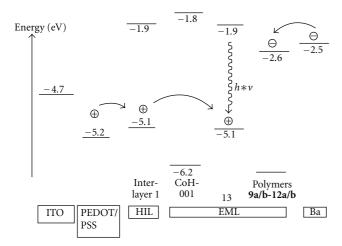


FIGURE 13: Energy levels of the used blend materials in the OLED stack.

shows the luminance-voltage plot for the OLEDs with the eight polymers (9a/b–12a/b) introduced in Table 2. Figure 15 shows the corresponding current efficiency-luminance plot of the prepared OLEDs. The results obtained for the efficiency of the different polymers are listed in Tables 4 and 5.

Upon comparing the obtained luminances, we found that the metalinked structure 9a-12a always exhibits higher values than the corresponding paralinked polymers 9b-12b (Figure 14). Former studies on 1,3,5-triazinecore structures show that different shaped side groups affect the efficiency in an OLED device. Chen et al. studied different starshaped 1,3,5-triazinecore structures and the influence on side chains according to the electron mobility and triplet energy by using several green guests [12]. They found that 2,4,6-tris(biphenyl-3-yl)-1,3,5-triazine shows a high energy barrier at the interface. It has a low electron mobility, and as a result of this the hole and electron flow is better balanced. This leads to a high efficient device. The two other studied structures 2,4,6-tris(triphenyl-3-yl)-1,3,5-triazine and 2,4,6-tris(9,9'-spirobifluorene-2-yl)-1,3,5triazine exhibit lower triplett energy and with this a lower efficiency. Related to our work one can assume that using

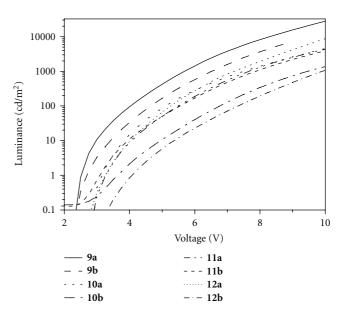


FIGURE 14: Luminance-voltage plot of OLEDs depending on the used electron-transporting polymers **9a/b–12a/b**.

metalinked phenyl-triazine polymers shows a better performance because of the improved triplett exciton limitation in the OLED stack.

In regard to the substitution (R₁), the nonsubstituted polymers **9a/b** show better properties with luminances of more than 10.000 cd/m² @ 10 V and lowest voltage onsets of about 2,4 V compared to the alkyl-substituted polymers **10a/b–12a/b**. All substituted polymers (**10a/b–12a/b**) show luminances between 800 cd/m² and 8000 cd/m² @ 10 V. The onset voltage increases with alkyl substitution to values between 2,7–3,4 V.

According to the efficiency, there is a difference between meta- or paralinked polymers (Figure 15). The metalinked nonsubstituted polymer (**9a**) shows the best efficiency with 45 cd/A @ 1080 cd/m² and is much higher than polymers with alkyl substitutions. Methyl, (**10a**) ethyl (**11a**) and tert.-butyl groups (**12a**) do not differ significantly in their performance. The efficiencies lie within the range of 34-35 cd/A @ 5000 cd/m², and the luminances are lower than

Device characteristics	9a /TMM102 + TEG001	10a /TMM102 + TEG001	11a /TMM102 + TEG001	12a /TMM102 + TEG001
Voltage/V @ 100 cd/m ²	4,4	5,35	5,1	5,25
Voltage/V @ 1000 cd/m ²	6,25	7,75	7,5	7,1
Voltage/V @ 5000 cd/m ²	8,2	>10	10	9,1
Voltage/V @ 10 mA/cm ²	7,7	9,5	9,25	8,5
Luminance Efficiency/cd/A+	36@8 V	34@8 V	35@7 V	34@8 V

TABLE 4: Voltage and efficiency of metasubstituted polymers 9a–12a.

Table 5: Voltage and efficiency of parasubstituted polymers 9b–12b.

Device characteristics	9b /TMM102 + TEG001	10b /TMM102 + TEG001	11b /TMM102 + TEG001	12b /TMM102 + TEG001
Voltage/V @ 100 cd/m ²	4,85	6,75	5,5	6,8
Voltage/V @ 1000 cd/m ²	6,85	9,5	8	9,1
Voltage/V @ 5000 cd/m ²	9	>10	>10	>10
Voltage/V @ 10 mA/cm ²	7,85	>10	9,5	10
Luminance Efficiency/cd/A+	24@7 V	29@10 V	32@8 V	20@10 V

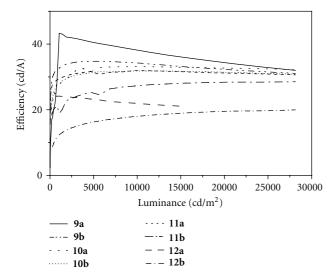


FIGURE 15: Current efficiency-luminance plot of OLEDs depending on the used electron-transporting polymers **9a/b–12a/b**.

for the nonsubstituted structure. No matter what kind of alkyl groups are added to the polymer, they show a lower performance in the OLED.

In contrast to the metalinked polymers, for paralinked polymers, the same difference cannot be found between alkyl-substituted 10b–12b and nonsubstituted polymers 9b. The nonsubstituted structure (9b) has an efficiency of about 22 cd/A, more than 20 cd/A lower than for the corresponding metalinked polymer 9a. Polymer 12b, with tert.-butyl groups, is the only one having lower efficiency. Methyl-(10b) and ethyl-(11b) substituted polymers show higher efficiencies.

While comparing the performance of the metalinked triazine side groups and the paralinked side groups, better performance is found for all metalinked active side

group polymers. Upon introduction of alkyl substituents, the performance of the OLEDs using these polymers as electron-transporting component generally is reduced. Alkyl substitution on the triazine polymer lowers the efficiency and luminance. The inserted side groups hinder an effective charge transport within the polymer structure. The longer or more compact the alkyl side group is, the smaller the reduction in the luminance.

The electroluminescence spectra in Figure 16 show a maximum absorption at about 520 nm and a small shoulder at 550 nm for all OLEDs using electron-transporting polymers 9a/b–12a/b. All OLEDs produced with polymers 9a/b–12a/b illustrate the same emission behavior which directly corresponds to the photoluminescence spectrum of the used emitter 13. No drift can be seen in the electroluminescence spectra; thus, there is no significant influence of the structure of the electron-transporting polymer used.

As a result of testing the new OLEDs depending on the synthesized polymers 9a/b-12a/b, we found that the introduction of larger alkyl substitutions (ethyl, tert.-butyl) to the 2,4-diphenyl-1,3,5-triazine basic side-group structure leads to a significant loss in OLED performance. This can be explained by the electrical inactive alkyl chains which hinder an efficient charge transport in the blend. In contrast to that, the unsubstituted polymers 9a/b already give good luminance and current efficiencies in single layer blend structures.

Besides the substituents, the choice of the linkage of the triazine basic structure to the polystyrene backbone is quite important for OLED performance. It is found that the metalinkage (9a–12a) leads to significantly enhanced luminance and current efficiencies in comparison to the para-linkage (9b–12b).

The general conclusion of this work is that a metalinkage of the active triazine unit to the polystyrene is preferred and that unsubstituted phenyl-triazines lead to most efficient devices.

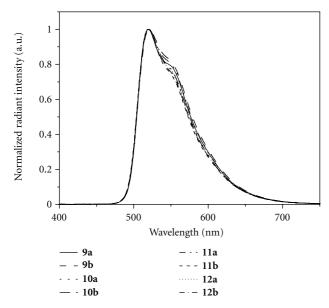


FIGURE 16: Electroluminescence spectra of OLEDs using different electron-transporting polymers (9a/b–12a/b) in the emitting blend.

4. Conclusion

Eight polystyrenes with electron-transporting 2,4,6-triphenyl-1,3,5-triazine side groups were synthesized. The triazine groups were linked in meta- or paraposition to the polystyrene backbone. Furthermore, the new polymers differ in alkyl substitution of the 4- and 6-phenyl rings. While comparing the meta- and the paralinked polymers, we recognize higher average molecular weight and higher glass transition temperatures for the paralinked polymers (10b–12b). The electron-transporting polymers were tested in green phosphorescent OLEDs in a blend with an Ir-emitter 13 and a cohost CoH-001 as a wideband gap material.

The new electron-transporting polymers lead to efficient and highly luminescent OLEDs. The best performance was obtained for the polymers without alkyl substitution 9a/b. The alkyl substitution as an electrical insulating structure constrains an effective charge transport between the active species and finally leads to lower OLED efficiency and luminance. Furthermore, the metalinked polymers 9a–12a exhibit higher efficiency and luminance than their paralinked analogues 9b–12b.

Further studies will focus on copolymers consisting of the most promising electron-transporting candidates.

Acknowledgments

The authors would like to thank the Federal Ministry of Education and Research of Germany (BMBF) for the financial support within the NEMO project 13N10618. The authors would like to thank Stefanie Kreissl for device preparation.

References

- [1] J. H. Burroughes, D. D. C. Bradley, A. R. Brown et al., "Light-emitting diodes based on conjugated polymers," *Nature*, vol. 347, no. 6293, pp. 539–541, 1990.
- [2] T. R. Hebner, C. C. Wu, D. Marcy, M. H. Lu, and J. C. Sturm, "Ink-jet printing of doped polymers for organic light emitting devices," *Applied Physics Letters*, vol. 72, no. 5, pp. 519–521, 1998.
- [3] N. B. McKeown, S. Badriya, M. Helliwell, and M. Shkunov, "The synthesis of robust, polymeric hole-transport materials from oligoarylamine substituted styrenes," *Journal of Materials Chemistry*, vol. 17, no. 20, pp. 2088–2094, 2007.
- [4] C. Adachi, M. A. Baldo, M. E. Thompson, and S. R. Forrest, "Nearly 100% internal phosphorescence efficiency in an organic light emitting device," *Journal of Applied Physics*, vol. 90, no. 10, pp. 5048–5051, 2001.
- [5] M. A. Baldo, M. E. Thompson, and S. R. Forrest, "Highefficiency fluorescent organic light-emitting devices using a phosphorescent sensitizer," *Nature*, vol. 403, no. 6771, pp. 750–753, 2000.
- [6] B. Tong, Q. Mei, S. Wang, Y. Fang, Y. Meng, and B. Wang, "Nearly 100% internal phosphorescence efficiency in a polymer light-emitting diode using a new iridium complex phosphor," *Journal of Materials Chemistry*, vol. 18, no. 14, pp. 1636–1639, 2008.
- [7] M. Suzuki, S. Tokito, F. Sato et al., "Highly efficient polymer light-emitting devices using ambipolar phosphorescent polymers," *Applied Physics Letters*, vol. 86, no. 10, Article ID 103507, 3 pages, 2005.
- [8] M. W. Thesen, B. Höfer, M. Debeaux et al., "Hole-transporting host-Polymer series consisting of triphenylamine basic structures for phosphorescent polymer light-Emitting diodes," *Journal of Polymer Science, Part A*, vol. 48, no. 15, pp. 3417– 3430, 2010.
- [9] M. W. Thesen, H. Krueger, S. Janietz, A. Wedel, and M. Graf, "Investigation of spacer influences in phosphorescent-emitting nonconjugated PLED systems," *Journal of Polymer Science, Part A*, vol. 48, no. 2, pp. 389–402, 2010.
- [10] M. Debeaux, M. W. Thesen, D. Schneidenbach et al., "Charge-transporting polymers based on phenylbenzoimidazole moieties," *Advanced Functional Materials*, vol. 20, no. 3, pp. 399–408, 2010.
- [11] C. W. Tang and S. A. Vanslyke, "Organic electroluminescent diodes," *Applied Physics Letters*, vol. 51, no. 12, article 913, 3 pages, 1987.
- [12] H. F. Chen, S. J. Yang, Z. H. Tsai, W. Y. Hung, T. C. Wang, and K. T. Wong, "1,3,5-Triazine derivatives as new electron transport-type host materials for highly efficient green phosphorescent OLEDs," *Journal of Materials Chemistry*, vol. 19, no. 43, pp. 8112–8118, 2009.
- [13] H. Inomata, K. Goushi, T. Masuko et al., "High-efficiency organic electrophosphorescent diodes using 1,3,5-triazine electron transport materials," *Chemistry of Materials*, vol. 16, no. 7, pp. 1285–1291, 2004.
- [14] R. A. Klenkler, H. Aziz, A. Tran, Z. D. Popovic, and G. Xu, "High electron mobility triazine for lower driving voltage and higher efficiency organic light emitting devices," *Organic Electronics*, vol. 9, no. 3, pp. 285–290, 2008.
- [15] M. Behl and R. Zentel, "Block copolymers build-up of electron and hole transport materials," *Macromolecular Chemistry and Physics*, vol. 205, no. 12, pp. 1633–1643, 2004.

- [16] M. Behl, E. Hattemer, M. Brehmer, and R. Zentel, "Tailored semiconducting polymers: living radical polymerization and NLO-functionalization of triphenylamines," *Macromolecular Chemistry and Physics*, vol. 203, no. 3, pp. 503–510, 2002.
- [17] L. Zeng, T. Y. H. Lee, P. B. Merkel, and S. H. Chen, "A new class of non-conjugated bipolar hybrid hosts for phosphorescent organic light-emitting diodes," *Journal of Materials Chemistry*, vol. 19, no. 46, pp. 8772–8781, 2009.

Hindawi Publishing Corporation Advances in Materials Science and Engineering Volume 2012, Article ID 794674, 14 pages doi:10.1155/2012/794674

Review Article

Efficiency Control in Iridium Complex-Based Phosphorescent Light-Emitting Diodes

Boucar Diouf, Woo Sik Jeon, Ramchandra Pode, and Jang Hyuk Kwon Ramchandra Pode,

¹ Department of Information Display, Kyung Hee University, Dongdaemoon-gu, Seoul 130-701, Republic of Korea

Correspondence should be addressed to Jang Hyuk Kwon, jhkwon@khu.ac.kr

Received 23 February 2012; Accepted 2 May 2012

Academic Editor: Etienne Baranoff

Copyright © 2012 Boucar Diouf et al. This is an open access article distributed under the Creative Commons Attribution License, which permits unrestricted use, distribution, and reproduction in any medium, provided the original work is properly cited.

Key factors to control the efficiency in iridium doped red and green phosphorescent light emitting diodes (PhOLEDs) are discussed in this review: exciton confinement, charge trapping, dopant concentration and dopant molecular structure. They are not independent from each other but we attempt to present each of them in a situation where its specific effects are predominant. A good efficiency in PhOLEDs requires the triplet energy of host molecules to be sufficiently high to confine the triplet excitons within the emitting layer (EML). Furthermore, triplet excitons must be retained within the EML and should not drift into the nonradiative levels of the electron or hole transport layer (resp., ETL or HTL); this is achieved by carefully choosing the EML's adjacent layers. We prove how reducing charge trapping results in higher efficiency in PhOLEDs. We show that there is an ideal concentration for a maximum efficiency of PhOLEDs. Finally, we present the effects of molecular structure on the efficiency of PhOLEDs using red iridium complex dopant with different modifications on the ligand to tune its highest occupied molecular orbital (HOMO) and lowest unoccupied molecular orbital (LUMO) energies.

1. Introduction

Achievements in organic light emitting diodes (OLEDs) lead to their integration as displays in several electronic devices and make them serious candidates to replace widely used LCD panels. Extensive research efforts have been made for higher achievements in organic displays both in industrial and academic fields [1–10].

In organic light-emitting devices (OLEDs), injected electrons and holes in the emitter will attract each other to form excitons [11–20]. Spin statistics demonstrate that the ratio between singlet and triplet excitons is one to three. In fluorescent OLEDs only the singlet excitons can generate radiative recombinations, giving a maximum inherent quantum efficiency of 25% [21–23], with no phosphorescent light radiation. On the other hand, triplet emitters can harvest both singlet and triplet radiative recombinations reaching a theoretical internal quantum efficiency of 100% [24–26]. Iridium and platinum complexes present good phosphorescent emission properties [27–29]. Iridium (III) complexes are the most widely used dopants in PhOLEDs because of their higher triplet efficiency [30–35].

PhOLEDs harvest both singlet and triplet emissions, making it possible to reach high efficiency devices. However, their operation and efficient implementation are more complex than for the fluorescent OLEDs.

To achieve high efficiency in PhOLEDs, the host material that forms the EML needs to satisfy a certain number of properties regarding the dopant as well as the adjacent layers. In PhOLEDs, the HOMOs and LUMOs of the host and phosphorescent emitter dopant have to be carefully selected to achieve a good exciton confinement within the EML. As well, a particular attention should be given to the origins and effects of charge trapping, concentration of the dopant, exciton quenching and the molecular structure of the dopant for a better control of the PhOLEDs' efficiency.

In fact, beside a fast decay of triplet dopant, the host materials need to have an energy gap wide enough to allow efficient energy transfers with the dopant (Figure 1) but should not induce charge trapping. A tradeoff is necessary between the width of the gap of the host material and the energy levels of the adjacent layers in order to allow good electrons and holes injection. The host material should as

² Department of Physics, Kyung Hee University, Dongdaemoon-gu, Seoul 130-701, Republic of Korea

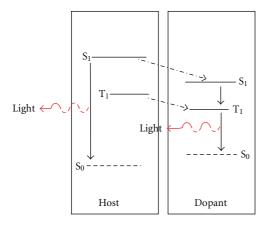


FIGURE 1: Energy structure between host and dopant in a PhOLED, S_1 represents the singlet excited states, T_1 the triplet excited states, and S_0 the ground states.

well present equivalent transport properties for electrons and holes for a balanced number of opposite carriers to recombine efficiently.

The excitation energy will efficiently transfer from the host to the triplet energy of the dopant when the triplet energy of the dopant is lower than the triplet energy of the host. The triplet excitons confinement in the dopant will make it possible to observe the phosphorescent light emission [36]. To maximize the performance of PhOLEDs, the dopant should be uniformly dispersed in the host matrix to minimize the exciton quenching or triplet-triplet annihilation [37].

The guest molecules are believed to act potentially as charge traps for electrons and holes in the EML, resulting in an increase of the driving voltage [31]. Two processes of electroluminescence in the doped EML exist. Light emission can be from the energy transfer from the host to the dopant or from trapped charges in the dopant. In the latter situation, it is assumed that the dopant molecules will act as recombination centers attracting charges by coulomb interaction if the radius of separation is within a certain range. Charge trapping effects can be observed with the presence of a large barrier at the interface between a carrier transport layer and the host material or when the gap between the host and the dopant HOMO and LUMO energy levels is too wide.

A high doping concentration minimizes the charge trapping but results in exciton quenching thereby lowering the efficiency of the light emitting device [31]. Therefore, a good balance between charge trapping, charge mobility for the recombination zone in the emissive layer, and a low enough doping concentration to avoid efficiency loss due to exciton quenching is desirable.

Triplet confinement may be controlled in two ways, namely, within the EML itself and then by the adjacent layers. The confinement in the EML is achieved when the guess material has its HOMO and LUMO levels within the band gap of the host material [31, 38]. While the adjacent layers will play the role of electron blocking layer so that, the electrons from the cathode will not drift beyond the EML

and holes from the anode will not go beyond the EML. Such a confinement arrangement will give a higher probability of recombination between the electrons and holes within the EML [38].

The objective of this paper based on our research activities is to present our investigations to control the efficiency in PhOLEDs through triplet exciton confinement, minimization of charge trapping, doping concentration, and dopant molecules design to limit self-quenching. Results are presented in their decreasing order of influence on the efficiency of the PhOLEDs. Excitons confinement needs to be adjusted before the reduction of charge trapping. Charge trapping needs to be minimized before setting the optimum doping concentration. Finally, the dopant molecular structure will act as a fine tuner in the improvement of the efficiency of the PhOLEDs.

2. Devices Fabrication and Characterization

The samples presented in this paper were fabricated on a clean glass substrate precoated with 150 nm thick film of indium tin oxide (ITO) with a sheet resistance of $12\,\Omega/\text{square}$. The ITO film and organic insulator for covering ITO edge area were patterned by standard photolithography techniques and then clean by sonification in isopropyl alcohol and acetone, rinsed in deionized water before being irradiated in a UV-ozone chamber.

All organic materials were deposited by thermal vacuum evaporation technique under a pressure of about 10^{-7} Torr at a rate of 1 Å/s. Finally, LiF and Al were deposited to form the counterelectrode in another adjacent vacuum deposition chamber without breaking the vacuum; at a rate of 0.1 Å/s for LiF and 5–10 Å/s for Al.

The OLEDs active surface area is $2 \times 2 \text{ mm}^2$. Current density-voltage (J-V) characteristics were measured using a Keithley SMU 2635A; the luminescence-voltage (L-V) curves using a Minolta CA-100A, the Electroluminescence (EL), and CIE coordinate were obtained using a Minolta CS-1000A Spectroradiometer.

3. Excitons Confinement

To achieve excitons confinement in PhOLEDs, it is necessary to have a good control of the triplet excitons diffusion at the interfaces between the carrier transport layers and the EML. Such an achievement translates in practical in the fact that the electrons from the cathode and the holes from the anode do not travel beyond the emissive layer where the radiative recombination should take place [39, 40]. In such conditions, the adjacent layer that injects electrons in the EML should form a barrier of potential for the holes. Similarly, the hole injection layer should be a barrier of potential for the electrons as depicted Figure 2. The charge transport layer can ideally be the charge injection layer for a simpler device.

This type of arrangement imposes constraints in the combination of adjacent layers (with good charge transport properties) and the EML in regard of the relative position of their HOMO and LUMO levels. The use of wide band-gap host materials may be necessary in PhOLEDs [41–45] for the

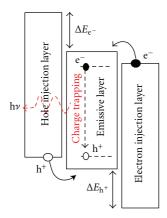


FIGURE 2: Excitons confinement in the emissive layer by the adjacent layer, $\Delta E_{\rm e^-}$ is the energy barrier for electrons, and $\Delta E_{\rm h^+}$ the energy barrier for the holes with charge trapping.

good energy transfer from the host to the dopant. This necessity induces a certain number of difficulties. When a wide band-gap material is used as a host material for the emitting layer, the carrier mobility decreases significantly since dopant molecules act as charge trapping sites [46]. To overcome such an issue, a high doping concentration of over 7% in green PHOLEDs may be required to make a good balanced current flow through dopant molecules. In such devices, exciton self-quenching and triplet-triplet annihilation by high doping concentration are unavoidable problems. For instance, when the doping concentration is increased from 2 to 6%, the phosphorescence photoluminescence quantum efficiency of tris(2-phenylpyridine)iridium (Ir(ppy)₃) is decreased by 5% [47]. Good excitons confinement is very difficult when making PhOLEDs with wide band-gap host materials. To overcome these constraints, a narrow band-gap host of 4,4'-N,N'-dicarbazoleterpheyl (CTP) was developed by our group [48]. In this study, we report highly efficient green phosphorescent devices comprising a triplet exciton confinement configuration using our CTP host with high triplet energy charge transporting layers. The maximum current and power efficiencies of 56.89 cd/A, and 48.22 lm/W with 18% external quantum efficiency (EQE) are realized by this good triplet exciton confinement configuration by minimization of self-quenching.

In order to make a better triplet exciton confinement configuration in green PHOLEDs, triplet energies among various hole-transport and electron transporting materials were investigated. As presented in the following, the highly efficient green PHOLEDs with 3% doping rate in CTP host and Ir(ppy)₃ dopant were demonstrated. Maximum current efficiency and EQE of 56.89 cd/A and 18.0% are obtained with a triplet exciton confinement configuration using a narrow band-gap CTP host and high triplet energy charge transporting layers. Such a high efficiency is attributed to a good triplet exciton confinement effect by the narrow band-gap CTP host, improvement of self-quenching issues of singlet and triplet excitons by reducing the doping concentration, and introduction of good triplet exciton blocking layers at the EML interfaces.

To investigate triplet exciton confinement ability, five devices were designed as follows:

Device A: ITO/NPB (40 nm)/CTP: Ir(ppy)₃ $(8 \text{ wt\%, } 30 \text{ nm})/\text{BAlq}(5 \text{ nm})/\text{Alq}_3$ (20 nm)/LiF (0.5 nm)/Al (100 nm);

Device B: ITO/NPB (30 nm)/TCTA (10 nm)/ CTP: Ir(ppy)₃ (8 wt%, 30 nm)/Bphen (25 nm)/LiF (0.5 nm)/Al (100 nm);

Device C: ITO/NPB (30 nm)/TCTA (10 nm)/ CTP: Ir(ppy)₃ (5 wt%, 30 nm)/Bphen (25 nm)/LiF (0.5 nm)/Al (100 nm);

Device D: ITO/NPB (30 nm)/TCTA (10 nm)/ CTP: Ir(ppy)₃ (3 wt%, 30 nm)/Bphen (25 nm)/LiF (0.5 nm)/Al (100 nm);

Device E: ITO/NPB (30 nm)/TCTA (10 nm)/ CTP: Ir(ppy)₃ (1 wt%, 30 nm)/Bphen (25 nm)/LiF (0.5 nm)/Al (100 nm).

Where α -NPB, TCTA, BPhen, and BAlq are N,N'-Bis(naphthalene-1-yl)-N,N'-bis(phenyl)benzidine), 4,4',4''-tris(N-carbazolyl)-triphenylamine), 4,7-diphenyl-1, 10-phenanthroline, and aluminum (III) bis(2-methyl-8-quinolinato)-4-phenylphenolate, respectively.

Device A was fabricated with a structure to be the reference sample. Device B was made with a triplet exciton confinement structure. J-V-L characteristics were measured over a brightness of 10,000 cd/m² and are displayed in Figure 3. For Device A we obtain at a brightness of 1000 cd/m² a driving voltage of 6.5 V, the current and power efficiencies are 21.93 cd/A and 10.82 lm/W. In Device B, the lower driving voltage of 4.7 V was measured due to the resistance reduction of CTP through good carrier injection and displacement in a narrow band-gap host as well as the good electron transporting properties of Bphen. CTP had been reported to be a good triplet green host and its exchange of energy (from S_1 to T_1) is as small as 0.3 to 0.5 eV [48]. As expected, Device B shows good current and power efficiencies of, respectively, 39.81 cd/A and 27.19 lm/W at a brightness of 1000 cd/m². Its performance is still not adequate when considering good triplet excitons confinement configuration in the EML. Very low current efficiency rolloff of 5% over the brightness of 10,000 cd/m² is observed in 8% doped CTP PhOLED. Deep hole trapping and shallow electron trapping in the wide band-gap host such as CBP and Ir(ppy)₃ dopant system have been already reported by other groups [46, 49]. The HOMO of $Ir(ppy)_3$ (5.3 eV) forms deep traps for holes in the host, governing the transport of holes in the EML. At high doping concentration, the emission zone is spread out in such a deep hole trapping device. Consequently, the selection of suitable host candidate with reasonable doping concentration is a critical issue to achieve high efficiency PHOLEDs as proven in reference [33]. Considering low roll-off characteristics in our devices, self-exciton quenching and triplet-triplet annihilation may be of high importance due to high doping concentration. To substantiate our argument, the doping concentration of Device B is varied to improve the triplet exciton confinement.

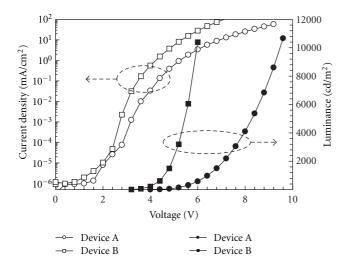


FIGURE 3: J-V-L and efficiency characteristics of Devices A and B.

Several PHOLEDs with Ir(ppy)₃ doping concentrations of 5%, 3%, and 1% were fabricated with the Device B structure. These devices are designated as Device C (5%), D (3%), and E (1%). Figure 3 shows the J-V-L characteristics of fabricated green phosphorescent devices. The J-V characteristics with decreasing doping concentration from 5% to 1% have significantly increased the resistance to current conduction. The current densities at 5.0 V are 3.80 mA/cm², 1.40 mA/cm², and 0.63 mA/cm² for, respectively, the 5%, 3%, and 1% doped devices (Device C, D, and E, resp.). The driving voltages for Device C, D, and E to reach 1000 cd/m² are, respectively, 4.7, 5.1, and 5.4 V (Figure 4). Improvement of *J-V* characteristics with increasing doping concentration is a well-known phenomenon, as well as the origin of luminescence from trapped charges by dopant molecules [46]. In fact, the Ir(ppy)₃ dopant and CTP host have, respectively, their HOMO energy levels at 5.3 and 5.7 eV, hence a gap of 0.4 eV leads to a hole trapping in our devices. At a given constant brightness of 1000 cd/m², the current and power efficiencies are 49.14 cd/A and 32.16 lm/W for Device C, 55.76 cd/A and 33.68 lm/W for Device D, and 50.90 cd/A and 29.61 lm/W for Device E. The maximum current efficiency and EQE of 49.14 cd/A and 15.5% for Device C, 56.89 cd/A and 18.0% for Device D, and 51.56 cd/A and 16.3% for Device E were obtained. The current efficiency of device E is improved by a factor of 1.4 compared to Device B.

4. Charge Trapping

Electroluminescence in PhOLEDs, as described previously, comes either from the energy transfer from the host to the guest molecules or from the charge trapping by the guest molecules. In the energy transfer model, the light emission by the dopant is due to the energy transfer from the excited host to the dopant [30, 50, 51]. The exciton is formed in the host material before being transferred to the dopant. Charge trapping has been studied from the beginning of models in the field of organic semiconductor based devices; it affects the device performance in OLEDs, organic thin film

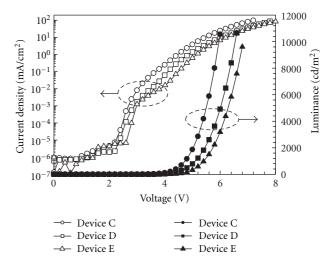


FIGURE 4: J-V-L and efficiency characteristics of Devices C, D, and E.

transistors, and organic photovoltaic cells. In the emission by charge trapping, the direct recombination of electrons and holes occurs on guest molecules, and their trapping can significantly influence the external electroluminescence quantum efficiency. The essential requirement for carrier trapping is that the guest dopant must have a higher HOMO and a lower LUMO energy than that of the host material [52]. The charge trapping mechanism will also be observed when there is a large energy barrier for charge injection from charge transport layer to the host material.

Charge trapping model assumes that the dopant acts as a trap site which can capture a charged carrier [30, 53–55]. The trapped charge recombines with a charge carrier of opposite sign to form an exciton which can contribute to light emission. In this mechanism charge carriers are directly trapped at dopant sites and the dopant is the center for the recombination and emission.

Charge trapping within the dopant material can be explained by the distribution of dopant molecules within the host. When a low concentration of the dopant in host matrix is used, the mobility limitation of a charge from one dopant site to another will lead a higher driving voltage [30]. If for example the host is n type material, as 4,4'-N,N'-dicarbazolebiphenyl (CBP), and the dopant material Ir(ppy)₃ which is a p-type molecule, holes hop among the Ir(ppy)₃ molecules in the CBP EML. With the low doping concentration, the distance between the Ir(ppy)₃ molecules is large and appears to be a hole trap. In such a situation, the hole trapping limits additional hole injection which results in the increase of the driving voltage. However, when the doping concentration increases, the hole mobility increases since the distance between the $Ir(ppy)_3$ molecules decreases. Such a transport characteristic effectively decreases the driving voltage.

The two light emission mechanisms in PhOLEDs are different in that the exciton formation center is the dopant molecule in the case the charge trapping model and the host molecule for the energy transfer model. Both mechanisms

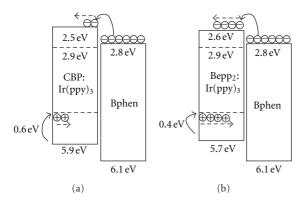


FIGURE 5: Energy level diagrams of CBP: Ir(ppy)₃ (a) and Bepp₂: Ir(ppy)₃ PHOLEDs (b).

contribute to the light emission in a certain rate depending on the device structure and energy levels of the organic materials in the PhOLED.

Charge trapping in PhOLEDs can be investigated by changing the concentration of the phosphorescent emitting material in the emissive layer and its dependence with the driving voltage can be studied. Charge trapping can be shallow or deep and it can be selective as concerning only electrons or only holes. In fact charge traps can be divided in two categories described as shallow traps and deep traps. The shallow traps can be activated and carried in the electric current by tunneling thermally activated or by hopping. Localized electronic states called deep traps are too deep to be thermally activated into current carrying states, they are effectively static. The presence of fixed charges modifies the electrostatic landscape of the material and leads to changes in electrons and holes recombination efficiency in OLEDs. It can as well improve the brightness of the device as it contributes to the electroluminescence, but it can be a disadvantage as it enhances the driving voltage [30].

4.1. Charge Trapping in Green PhOLED. These above arguments have been confirmed by our group in different studies such as the effect of hole trapping in green PhOLEDs using Ir(ppy)₃ green emitter in two different host matrices CBP and Bepp₂ (bis[2-(2-hydroxyphenyl)-pyridine]beryllium) [30] as represented, Figure 5. We fabricated PHOLEDs with the following structure: ITO/NPB (30 nm)/TCTA (10 nm) Bepp₂: Ir(ppy)₃, or CBP: (30 nm): Ir(ppy)₃/Bphen (25 nm)/LiF (5 nm)/Al (100 nm).

We have realized the host-guest system to optimize the performance of green PHOLEDs based on a comparison between two host materials with different energy gaps: CBP and Bepp₂. The minimization of hole trapping on the guest molecules and reduction of self-quenching or triplet-triplet annihilation are key factors to achieve the high efficiency. When compared with the wide band gap CBP, using a narrow band gap host (Bepp₂) and green phosphorescent Ir(ppy)₃ metal complex guest concentration as low as 2%, the current and power efficiencies of 62.5 cd/A (EQE 19.8%) and 51.0 lm/W, respectively, and a low current efficiency roll-off value of 10% over the brightness of 10,000 cd/m² were

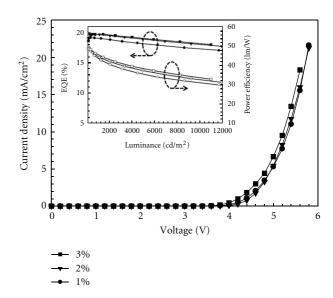


FIGURE 6: J-V characteristics of fabricated Bepp₂: $Ir(ppy)_3$ green PHOLEDs with doping concentration from 1 to 3%. Inset shows the EQE and power efficiency as a function of luminance.

demonstrated in this Bepp₂ single-host system (see Figure 6). We have limited the charge trapping by the use of an ideal host-guest device structure to produce a high efficiency phosphorescent device by minimizing hole trapping on the guest molecules and reducing self-quenching or triplet-triplet annihilation. The device structure to optimize the high current efficiencies, low current roll-off, high color stability, and low doping conditions has been explored.

To corroborate further our hypothesis of shallow hole trapping at the phosphorescent molecules in the emitting layer, we performed the capacitance measurements as a function of applied voltages in a 3% Ir(ppy)₃ doped in the Bepp₂ and CBP devices. A constant dc bias ranging from 0 V to 10 V was superimposed on the ac bias. Figure 7 shows the capacitance variation normalized to the geometrical capacitance (C_0) with the applied dc voltage. As seen from Figure 7, the capacitance of doped and undoped devices increases in forward bias, reaches a maximum value, and then decreases. Onset of the increase depends on the host material. This result suggests that the increase of capacitance may be dependent on the capacity of holding charges in the emitting layer. At zero bias, the capacitance of all devices is the same as the geometrical capacitance. On applying a small forward bias, no change in capacitance is observed and it remains equal to C_0 . It starts increasing when the hole injection begins from the anode and reaches a maximum point due to the accumulation of hole charges. On further increase of bias voltage, the minority charge carriers injection occur, resulting in a recombination of holes and electron in the emitting layer and subsequently the emission of light.

Early occurrence of recombination as observed in a $Bepp_2 : Ir(ppy)_3$ device indicates that the hole trapping in the $Bepp_2$ host is not a serious issue when compared to that of $CBP : Ir(ppy)_3$ and this cannot be attributed to the electron mobility in $Bepp_2$ (about $10^{-4} \, cm^2/Vs$) and CBP materials

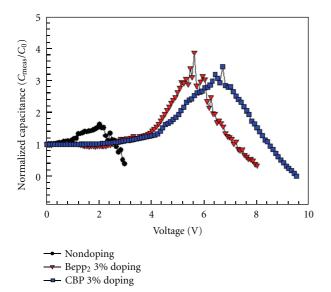


FIGURE 7: Capacitance variation normalized to geometrical capacitance (C_0) with the applied dc voltage.

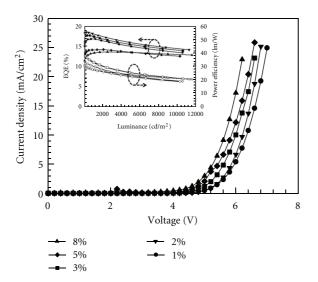


FIGURE 8: J-V characteristics of CBP: $Ir(ppy)_3$ green PHOLEDs with doping concentration from 1 to 8%. Inset shows the EQE and power efficiency as a function of luminance.

(about 3×10^{-4} cm²/Vs). The shallow traps for hole charge carriers which facilitate its transport may be responsible for the early recombination of electron and hole carriers in Bepp₂: Ir(ppy)₃ device.

Ideal host-guest device structures produce a high efficiency phosphorescent device minimizing the hole trapping on the guest molecules and reducing the self-quenching or triplet-triplet annihilation. The device structure to optimize the high current efficiencies, low current roll-off, high color stability, and low doping conditions has been explored. The doping concentration was varied from 1 to 8%. The *J-V* characteristics (Figure 8) show a strong dependence on the dopant concentration.

The strong dependence of J-V characteristics on the dopant concentration is the consequence of the fact that the phosphorescent green emission is strongly dependent on the hole trapping at the phosphorescent guest molecules level. The deep hole trapping and the shallow electron trapping in the CBP host and Ir(ppy)₃ dopant system were reported earlier by other groups [26, 29]. The HOMO of Ir (ppy)₃ (5.3 eV) forms the deep traps for the holes in the CBP host (HOMO = 5.9 eV), governing the transport of holes in the emitting layer. Further, the strong 510 nm green Ir(ppy)₃ emission peak (CIE (x, y) coordinates at 1000 cd/m² are (0.29 to 0.31, 0.60)) and a weak emission at about 450 nm due to the CBP host appear at a concentration below 5%. Upon enhancing the dopant concentration, the CBP host emission completely disappeared. Even if the better device performance appears at the low doping concentration, the high roll-off and the emission from the host in the EL output are attributed to the too narrow emission zone by deep hole trapping in the CBP host. The emission zone is spread out with a high doping concentration in such deep hole trapping devices. Consequently, the selection of the suitable host candidates is a critical issue to achieve the high efficiency PHOLEDs.

4.2. Minimization of Charge Trapping in Red PhOLEDs. In this section, we present the minimization of charge trapping in red PhOLEDs by a good energy level match between the host and guest. Förster and/or Dexter energy transfer processes [56] between host and guest molecules play an important role in confining the triplet energy excitons in the phosphorescent guest. This determines the triplet state emission efficiency in PHOLEDs. Förster energy transfer [57] is a long range interaction (up to 10 nm) due to dipoledipole coupling of donor host and acceptor guest molecules, while Dexter energy transfer [58] is a short-range process (typically 1–3 nm) which requires overlapping of orbitals of adjacent molecules. The phosphorescence emission in the conventional host-guest phosphorescent system occurs either with Förster transfer from the excited singlet S₁ state of the host to the excited singlet S₁ state of the guest and Dexter transfer from the triplet T₁ state of the host to the triplet T₁ state of the guest or direct exciton formation on the phosphorescent guest molecules, resulting in a reasonable good efficiency.

In the following, we demonstrate that to achieve high efficiency PhOLEDs a good confinement of the triplet exciton of phosphorescent dopant is needed with the use of an appropriate triplet energy gap host. Such a combination host-guest will result in an efficient radiative decay in the dopant. We illustrate this principle comparing first the efficiency of the same red emitter tris(1-phenylisoquinoline)iridium (Ir(piq)₃) in a CBP matrix or in Bebq₂ (bis(10-hydroxybenzo [h]quinolinato)beryllium) matrix, the CBP band gap being wider than Bebq₂ band gap. Second, the same host Bebq₂ is doped with Ir(phq)₂(acac)(iridium (III) bis(2-phenylquinoline) acetylacetonate) that has a narrower gap than Ir(piq)₃ (Figures 9 and 10).

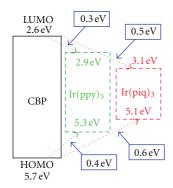


FIGURE 9: Energy level diagram of the Ir(ppy)₃ green and Ir(piq)₃ red phosphorescent complex doped by the CBP host.

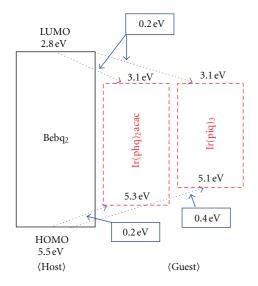


FIGURE 10: Energy level diagram of the Bebq₂ fluorescent host and Ir(phq)₂ acac and Ir(piq)₃ red phosphorescent dopant materials.

Figure 9 shows the energy level diagram of the Ir(piq)₃ red phosphorescent complexes used in doping the CBP host while Figure 10 shows the energy diagrams for both Ir(piq)₃ and Ir(phq)₂(acac) in Bebq₂ matrix. However, the wide band-gap host and narrow gap guest system often causes an increase in the driving voltage due to the difference in HOMO and/or LUMO levels between the guest and host materials [59]. Thus, the guest molecules are thought to act as deep trapping centers for electrons and holes in the emitting layer, causing an increase in the driving voltage of the PHOLED. The dopant concentration in such a hostguest system is usually as high as about 6-10% because injected charges should move through guest molecules in the emitting layer. Therefore, self-quenching or triplet-triplet annihilation by guest molecules is an inevitable problem in host-guest systems with high doping concentrations. Earlier, Kawamura et al. had reported that the phosphorescence photoluminescence quantum efficiency of Ir(ppy)₃ could be

decreased by 5% with an increase in the doping concentration from 2% to 6% [47]. Consequently, the selection of suitable host candidates is a critical issue when fabricating high efficiency PHOLEDs.

We demonstrate the importance of exciton confinement in the efficiency of a PhOLED based on the energy difference between the host matrix and the guest molecules for the same phosphorescent emitter. A narrower band gap host will result in a higher efficiency PhOLED. In this study, the minimized charge trapped host-guest system is investigated by using a narrow band-gap fluorescent host material in order to address device performance and manufacturing constraints. Here, we report an ideal host-guest system that requires only 1% guest doping weight for a good energy transfer and provides ideal quantum efficiency in PHOLEDs. We also report that strong fluorescent host materials function very well in phosphorescent OLEDs.

PhOLEDs operation can be explained based on efficient Förster energy transfers from the host singlet state to the guest singlet and triplet mixing state which appears to be the key mechanism for phosphorescence emission.

Indeed, such an enhanced performance of the Bebq2: Ir(phq)2 acac PHOLEDs was not expected with an extraordinary low doping concentration (1%) by contrast with most phosphorescent devices (6-10%). In order to investigate the origin for the enhanced performance, we fabricated several PHOLEDs by varying the doping concentration from 0.5% to 2% in the host-guest system. Current and luminance evolutions as a function of voltage are presented in Figure 11. These data provide evidence for: (1) complete energy transfer from the fluorescent host to phosphorescent guest, except at extremely low doping concentrations (0.5%); (2) no significant difference between measured I-V characteristics for identical devices but with different dopant concentrations ranging between 0.5 and 2%; (3) the quenching of both luminance, and current and power efficiencies with higher doping concentrations (2%).

Therefore, a highly efficient simple bilayer PHOLED structure with a $Ir(phq)_2$ acac guest doping concentration as low as 1% in the narrow band-gap Bebq₂ fluorescent host was demonstrated for the first time by our group.

To understand the phosphorescence emission mechanism more precisely in the Bebq₂:Ir(phq)₂acac host-guest system, we fabricated and studied a series of PHOLEDs. First, we used the well-known wide band-gap CBP host material instead of Bebq₂ and fabricated the device with a structure: NPB (40 nm)/CBP:Ir(phq)₂acac (30 nm, 10%)/BAlq (5 nm)/Alq₃ (20 nm)/LiF (0.5 nm)/Al (100 nm). At a luminance of 1000 cd/m² the resultant operating voltage was 7.1 V with current and power efficiencies of 14.41 cd/A and 6.28 lm/W, and an EQE of 11.5%. Furthermore, the maximum current and power efficiencies were 14.43 cd/A and 8.99 lm/W.

Obviously, the two fold increase in the driving voltage is a consequence of the deep trapping of injected holes and electrons at Ir(phq)₂acac sites in the CBP:Ir(phq)₂acac system. Direct charge trapping at the Ir(phq)₂acac guest

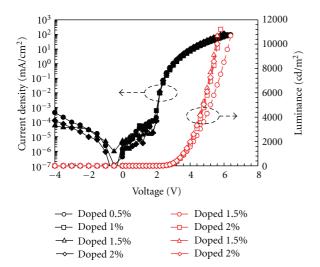


FIGURE 11: *J-V-L* plot of red PHOLEDs doped with different concentrations (0.5–2%) of Ir(phq)₂acac in Bebq₂.

molecules seems to be the key mechanism for phosphorescence emission in this host-guest system.

To corroborate our experimental results further, a PHOLED was fabricated using Ir(piq)₃ red emitting phosphorescent doping instead of Ir(phq)2acac and a Bebq₂ host. The fabricated device was: DNTPD (N,N')diphenyl-*N*,*N*′-bis-[4-(phenyl-m-tolylamino)-phenyl]-biphenyl-4,4'-diamine) $(40 \text{ nm})/\text{Bebq}_2 : \text{Ir}(\text{piq})_3 (50 \text{ nm},4\%)/$ LiF (0.5 nm)/Al (100 nm). A weak emission peak at 500 nm in the electroluminescence spectra due to the Bebq₂ host arises at a doping concentration of 4% (significantly high by comparison with an Ir(phq)₂acac doping concentration 0.5%), accompanied by a strong peak at 620 nm due to an Ir(piq)₃ doping molecule. At luminance of 1000 cd/m², the corresponding operating voltage, current and power efficiencies were 3.5 V, 8.41 cd/A, and 7.34 lm/W. Furthermore, the maximum current and power efficiency values were 9.38 cd/A and 11.72 lm/W. Increasing the Ir(piq)₃ concentration to 6% suppresses the Bebq₂ host emission and results in a clean electroluminescence red emitting peak at 620 nm due to the Ir(piq)₃ doping molecules. However, the device performance deteriorates with increasing doping concentration due to the self-quenching.

5. Ideal Doping Concentration

In PhOLEDs the triplet-triplet energy transfer between host and dopant molecules is explained based on Dexter mechanism [21, 60, 61] which is a short-range intermolecular interaction involving wave functions overlap [26, 62]; it takes place within about 1 nm range [63, 64]. This imposes constraints in the distribution and concentration of the dopant molecules within the host matrix. Among the conditions for good efficiency is the fact that every host molecule in an excited state will need to have a guest molecule in a range close enough to receive this excitation energy and radiate it back in form of phosphorescent light [65, 66]. This

doping concentration can be idealized for any system, but among PhOLEDs of a given color, it is necessary to first of all maximize the exciton confinement and minimize the charge trapping by minimizing the energy gap between the host and guest HOMOs and LUMOs [67, 68] as presented earlier in this paper. The ideal doping concentration should minimize charge trapping, self-quenching and triplet-triplet annihilation [67, 69].

In this context, we have evaluated an ideal guest concentration in PhOLEDs and made an experimental comparison to support our predictions. We use a green PhOLED, for which we evaluate an ideal doping concentration of about 1.5%.

We assume films with a crystalline structure. In order to have the most compact configuration we choose a disposition of molecules in face-centered cubic (fcc) organization. The host molecules are located at the vertexes of extended unit lattice containing $4 \times 4 \times 4$ host molecules. In such a structure we replace the excited host molecule located at the center by a dopant molecule. Obviously, this choice is not completely conform with the reality as the actual samples are rather amorphous. This will cause a certain discrepancy when comparing with experimental results. Nevertheless, this approach is valid because the molecular densities of the structures are equivalent and the size of host and guest molecules we will be using experimentally are comparable both for CBP or Bepp₂ as a host matrix when using Ir(ppy)₃ as a green phosphorescent dopant, respectively, 8.67, 9.23, and 11.9 Å.

Our computation gave a molecular number corresponding to the constant molar fraction of 0.93 mol% (1/107 mole fraction) as an ideal Dexter transfer condition. From this assumption and consideration of molecular weight of host and dopant molecules, we could simply get an ideal doping concentration. As an actual experimental condition, we obtained 1.19% of doping concentration by changing 0.93 mole fraction to weight fraction for CBP/Ir(ppy)3 system from this approach. However, there could be some discrepancy between this condition and experimental results because it assumed that the dopant molecules may have similar size to that of host molecules due to a small fraction of dopant molecules. Nevertheless, the prediction we obtained for the CBP/Ir(ppy)₃ system was very close to that obtained from the Kawamura's approach (1.02%, [70]). This indicates that our lattice assumption is closely matched to a real amorphous film situation. Similarly, 1.93% (0.93 mol%) of doping concentration was predicted in case of Bepp₂/Ir(ppy)₃ system.

This consideration lead us to estimate that in 1D picture two dopant molecules should be separated by two host molecules (Figure 12).

From simulations and experiments with 1D concept we obtain a good PhOLEDs performance with a doping concentration as low as 1%. This is the reason why we assumed the molecular arrangement described above.

For the verification of our assumptions, we conducted a series of experiments varying the doping concentration in the emissive layer. The strong green light emission at 510 nm for all electroluminescence curves is attributed to the

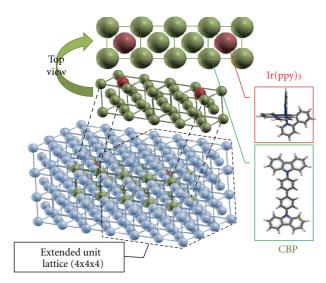


FIGURE 12: Imaginary molecular arrangements assuming a cubic lattice which is filled by imaginary spherical molecules as an fcc arrangement.

phosphorescence of Ir(ppy)₃. In principle, we can detect the side emission from the host material if the energy transfer is incomplete or inefficient. We observed that the host emission (at 420 nm-450 nm) disappears at the expected ideal doping concentration of 1.0% when the EML thickness of CBP is 10 nm. The doping concentration requirement for the elimination of CBP host emission (for complete energy transfer), however, increases when increasing the EML thickness; for instance, 3% for 20 nm and 5% for 30 nm. The necessity of a higher doping concentration for a thicker EML condition is presumably due the large discrepancy of HOMO and LUMO levels between the CBP host and guest materials (Figure 13) which might give a deep trapping nature. The injected holes in the doped EML cannot move easily due to deep trapping in Ir(ppy)₃ guest molecules and as a result an excess of charges will be located around the HLT/EML interface. Some electrons will be able to penetrate the HTL due to a relatively high electron mobility of doped EML. In such devices, a higher doping concentration is favorable to get high device performances as we reported previously [46].

However, such an overdoping is not necessary for thinner EML (about 10 nm) because the countercharge carriers (the electrons) may be injected and transported earlier than holes. Thus, they are easily crowded at the HTL/EML interface because the difference of LUMO levels between CBP host and Ir(ppy)₃ guest is relatively small (about 0.4 eV), while the difference of HOMO levels of same system is larger (about 0.6 eV) [46]. Thus, holes carriers can recombine with electrons very early before the preliminary trapping process starts at the guest molecules. In other words, the probability of holes migration to the opposite side (toward cathode) is presumably weaker than that of electrons migration toward anode side. From these circumstances and results, we conclude that the ideal doping concentration of CBP/Ir(ppy)₃ system could be 1% to the exclusion of the

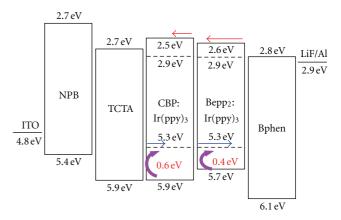


FIGURE 13: Energy band diagram of CBP: Ir(ppy)₃ and Bepp₂: Ir(ppy)₃ based green PHOLEDs.

trapping processes. As a result, we come to a conclusion that the ideal doping ratio could be derived or predicted from the consideration of the molecular packing condition in extended unit lattice (the expected doping ratio of CBP/Ir(ppy)₃: 1.19%). However, we observed the maximum EQE value at the slightly thicker, overdoped condition suggesting that 10 nm is too thin to confine most carriers at the EML region. It means that the ideal doping concentration for complete energy transfer could be somewhat different from that gives the maximum device efficiency.

Similarly, a relatively low doping concentration of about 1.93% was predicted for ideal and complete energy transfer in Bepp₂/Ir(ppy)₃. And this was confirmed by the EML spectra of Bepp₂/Ir(ppy)₃ as a function of EML thickness and doping ratio. Bepp₂/Ir(ppy)₃ does not require an overdoping at the thicker EML condition; for instance 1.5% at 20 nm, 2% at 30 nm. The reason for a complete energy transfer at the relatively reduced doping ratio even in the thicker EML condition of Bepp₂/Ir(ppy)₃ is possibly due to the lower differences of LUMO levels and HOMO levels between host and guest molecules (0.3 to 0.4 eV). In other words the charge carriers may be spread out much more uniformly in all around EML regions because of no radiation of charge injection that provides good charge balancing in the EML layer. From such a situation showing relatively low energy barriers between HOMOs and LUMOs of host and guest molecules, we could obtain the ideal doping condition even at the normal thickness condition. As we recommended before, the discrepancy between the calculation and the experimental values might come from the assumptions of crystal lattice and molecular spheres, the slight difference of molecular sizes and so forth. Nevertheless, we achieved a very close approximation in the evaluation of an ideal doping concentration for PhOLEDs described by Dexter energy transfer.

From the extensive comparison of our devices, we conclude that the optimized condition for CBP/Ir(ppy)₃ is the 20 nm thickness and 3% doping concentration. In the other hand, only 1.5% doping concentration for the same thickness of 20 nm in the case of Bepp₂/Ir(ppy)₃, that shows a lower driving voltage and higher EQE. This difference

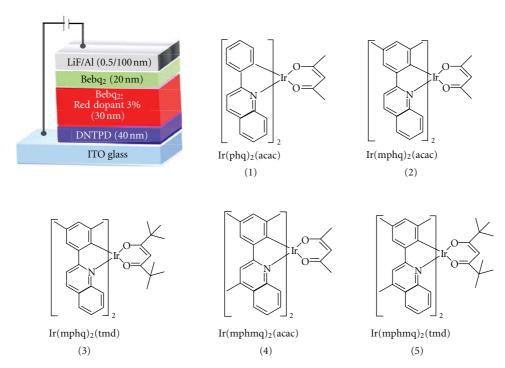


FIGURE 14: Schematic cross-section of red PHOLED with different complexes 1–5 and molecular structure of complexes 1–5.

reflects the fact that they are more delay processes such as charge trapping, nonradiative decay process, and triplet-triplet annihilation in CBP/Ir(ppy)₃.

6. PhOLED Materials

We demonstrate the importance of material structure to ultimately affect the HOMO and LUMO positions in the dopant and consecutively affect the efficiency of the PhOLED [41]. We synthesized red emitters based on Ir complexes with successive modifications on the ligands. We report new red dopants with methylated phenyl ring and quinoline ring which are coordinated to the Ir(III) atom. Every dopant also has ancillary ligands, such as acetylacetonate (acac) and 2,2,6,6-tetrametylheptane-3,5-dionate (tmd) groups. The PHOLEDs prepared by these organometallic complexes showed very efficient and bright red phosphorescence with extremely high EQE up to 24.6% (in case of the dopant with methylated main ligand and a sterically crowded tmd ancillary ligand). The addition of an electrondonating methyl group to the metallated phenyl ring (mphq) gave a bathochromic shift (compare to a reference sample), while the additional introduction of methyl group to the quinoline ring (mphmq ligand) led to a hypsochromic shift compared to the spectral range of the mphq ligand as presented below. In addition, the change of ancillary ligand to a tmd moiety from an acac moiety results in significant improvement of device efficiency.

In this study, we prepared Ir(phq)₂(acac)-based red dopants having sterically crowded alkyl moieties on their

main ligands as well as ancillary ligands. First, we added methyl groups on a phenyl part as well as a quinoline part of main lingand in Ir(phq)₂(acac) to increase intermolecular steric interaction to give reduced self-quenching effect. From this chemical modification, we could obtain very clear red spectra with much narrower full width at half-maximum. In addition, we also added sterically crowded ancillary ligand by using *tert*-butyl moiety to even protect the concentration quenching. The PHOLEDs containing those dopants as an emitter showed extremely high EQEs up to 24.6%, which corresponds to an extremely high record as a red electrophosphorescent device to date.

For the device fabrication, for the reasons of efficiency presented earlier, we utilized a narrow bandgap fluorescent host material, Bebq₂, to realize a highly efficient red PHOLEDs with excellent energy transfer [31, 71–77]. The exact device configuration used in this work was indium tin oxide (ITO)/DNTPD (40 nm)/Bebq₂: red dopants (3%, 30 nm)/Bebq₂ (20 nm)/LiF (0.5 nm)/Al (100 nm).

The device performances of the five different red PHOLEDs were investigated at the same doping concentration. The synthetic scheme and the chemical structures of those materials with formula $Ir(phq)_2(acac)$ (1), $(mphq)_2$ Ir(acac) (2), $(mphq)_2$ Ir(tmd) (3), $(mphmq)_2$ Ir(acac) (4), $(mphmq)_2$ Ir(tmd) (5), with (mphq) = 2-(3,5-dimethylphenyl) quinoline, (acac) = acetylacetonate, (tmd) = 2,2,6,6-tetrametylheptane-3,5-dionate, (mphmq) = 2-(3,5-dimethylphenyl)-4-methylquinoline, are summarized in Figure 14 with the device structure.

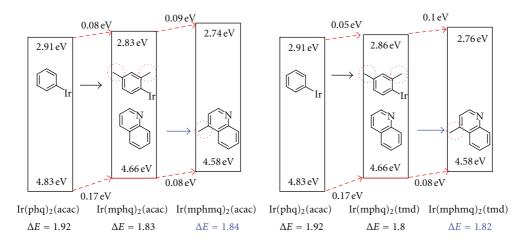


FIGURE 15: Energy band diagrams of complexes 1–5 from molecular simulation.

All five complexes show some vibronic bands in their emission spectra at 77 K. The phosphorescence peak wavelength can be fine-tuned by substitution of the electrondonating or electron-withdrawing groups to the main ligand. In order to qualitatively understand the nature of the phosphorescent excited state of cyclometalated iridium complexes, we preliminarily executed a HOMO/LUMO calculation on $Ir(phq)_2(acac)$. As a result, we found that the HOMO is distributed over the phenyl ring (3,5-position) and the iridium atom, while the LUMO is localized at the quinoline ring (4-position). Thus, the substitution of the electron-donating group (-CH₃) to the phenyl ring is expected to give a direct effect on lowering the HOMO level (stabilization of HOMO), which results in a reduction of the bandgap. The results obtained from the molecular simulation are summarized in Figure 15.

As a result, substitution of electron donating methyl group (-CH₃) for hydrogen in 3,5-position of phenyl chromophore of compound 1 leads to a 9-12 nm red shift, due the a destabilization of the d-orbital in the central Ir(III) atom from the change of this ligand-based excited state (compounds 2 and 3). Figure 16 shows the current densityvoltage (J-V) characteristics of fabricated red PHOLEDs. At a constant voltage of 5.0 V, current density values of 19.1, 23.7, 38.6, 24.4, and 27.9 mA/cm² are observed in the fabricated PHOLEDs A, B, C, D, and E, respectively. The driving voltage to reach 1000 cd/m² are 4.0, 3.8, 3.9, 3.7, and 3.7 V for Devices A, B, C, D, and E, respectively. All five PHOLEDs show similar J-V and luminance-voltage (L-V)characteristics because of similar HOMO and LUMO energy levels. Low turn-on voltages of 2.1 V for devices A, D, E, and 2.2 V for Devices B and C were observed. In the described PHOLED structure, the low driving voltage performance is attributed to the insignificant charge trapping and weak charge injection barriers at the interfaces [31, 71–77].

7. Conclusion

In this paper, we have presented four main elements that can have a direct control on the efficiency of iridium complex-

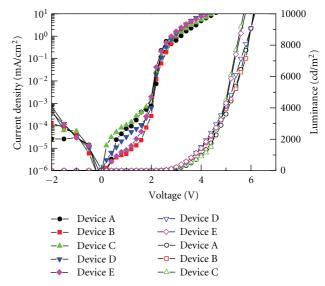


FIGURE 16: *J-V-L* characteristics of fabricated red PHOLEDs.

based PhOLEDs: exciton confinement, charge trapping, doping concentration, and the dopant molecular structure. We have demonstrated through our study that the host matrix HOMO and LUMO energy levels in comparison with the dopant levels in one hand and with the adjacent charge injection layers levels in the other hand, is the common denominator for exciton confinement, charge trapping, dopant concentration, and dopant molecular strucuture.

We have also shown the effects of exciton confinement using CTP host matrix doped with Ir(ppy)₃ for green PhOLEDs. Improvement of electron and hole blocking properties of the PhOLED by only changing the EMI's adjacent layers from the structure ITO/NPB/CTP: Ir(ppy)₃/BAlq/Alq₃/LiF/Al to ITO/NPB/TCTA/CTP: Ir(ppy)₃/Bphen/LiF/Al was observed. By implementing such configuration, we increased the luminous efficacy from 10.82 lm/W to 27.19 lm/W, the current efficiency from 21.93 cd/A to 38.81 cd/A while lowering the driving voltage from 6.5 V to 4.7 V.

Furthermore, we showed that the charge trapping can be controlled through the width of the host gap compared to the dopant, the wider energy difference can result the more charge trapping effect. That was illustrated with green dopant Ir(ppy)₃ and two different host matrices CBP and Bepp₂. Since CBP has a wider HOMO-LUMO gap than Bepp₂, we have shown that the charge trapping will be consecutively more important and as a result the driving voltage for the CBP based PhOLED is 6.8 V compared to 5.4 V for Bepp₂ for the same brightness.

The doping concentration that is tightly connected to charge trapping was proven to be adjustable to a minimum, once the energy mismatch was set to a minimum to reduce charge trapping. Such a fact was proven by our comparative study in green PhOLEDs, showing an optimum doping concentration under 2% for Bepp₂ matrix doped with Ir(ppy)₃ for green PhOLEDs.

The importance of the molecular structure of the dopant manifests by giving the possibility to tune the HOMO and LUMO levels of the dopant. In response, this had an effect on the efficiency of the final device, as we have proven earlier through the importance of the energy difference between the host and the dopant LUMOs' and HOMOs' energies.

Charge trapping and doping concentration are tightly connected as presented in this paper, nevertheless, we have shown that the doping concentration can be reduce to its minimum once the charge trapping itself is reduced to a minimum by minimizing the energy levels differences between the host and the dopant.

The relation between exciton confinement and charge trapping might also be a point of focus, as a better exciton blocker will have an influence in the electron and hole injection, but that should be tuned to result in a higher efficiency device.

In conclusion, we have demonstrated that four main elements: exciton confinement, charge trapping, dopant concentration, and dopant molecular structure directly affect the performance of the presented red and green PhOLEDs. These factors are dependent on each other and individually predominant depending on the situation.

Acknowledgment

This work was supported by the IT R&D Program of MKE/KEIT (10030834).

References

- [1] Y. Sun, N. C. Giebink, H. Kanno, B. Ma, M. E. Thompson, and S. R. Forrest, "Management of singlet and triplet excitons for efficient white organic light-emitting devices," *Nature*, vol. 440, no. 7086, pp. 908–912, 2006.
- [2] J. Endo, T. Matsumoto, and J. Kido, "Organic electroluminescent devices having metal complexes as cathode interface layer," *Japanese Journal of Applied Physics*, vol. 41, pp. L800– L803, 2002.
- [3] W. J. Lee, Y. K. Fang, H.-C. Chiang et al., "Improving turn on voltage and driving voltage of organic electroluminescent devices with nitrogen doped electron transporter," *Solid-State Electronics*, vol. 47, p. 927, 2003.

- [4] I. Tanaka, Y. Tabata, and S. Tokito, "Energy-transfer and lightemission mechanism of blue phosphorescent molecules in guest-host systems," *Chemical Physics Letters*, vol. 400, no. 1-3, pp. 86–89, 2004.
- [5] G. He, O. Scvhneider, D. Qin, X. Zhou, M. Pfeiffer, and K. Leo, "Very high-efficiency and low voltage phosphorescent organic light-emitting diodes based on a p-i-n junction," *Journal of Applied Physics*, vol. 95, p. 5773, 2004.
- [6] P. Wellermann, M. Hofmann, O. Zeika et al., "High-efficiency p-i-n organic light-emitting diodes with long lifetime," *Journal* of the Society for Information Display, vol. 13, no. 5, pp. 393– 397, 2005.
- [7] J. Meyer, S. Hamwi, T. Bulow, H.-H. Johannes, T. Riedl, and W. Kowalsky, "Highly efficient simplified organic light emitting diodes," *Applied Physics Letters*, vol. 91, p. 113506, 2007.
- [8] J. G. Jang and H. K. Shin, "High efficiency green phosphorescent organic light emitting device with (TCTA/ TCTA0.5TPBi0.5/TPBi): Ir(ppy)3 emission layer," *Thin Solid Films*, vol. 517, no. 14, pp. 4122–4126, 2009.
- [9] Q. Xin, W. L. Li, W. M. Su et al., "Emission mechanism in organic light-emitting devices comprising a europium complex as emitter and an electron transporting material as host," *Journal of Applied Physics*, vol. 101, Article ID 044512, 2007.
- [10] Y.-H. Niu, M. S. Liu, J.-W. Ka, and A. K.-Y. Jen, "Thermally crosslinked hole-transporting layers for cascade hole-injection and effective electron-blocking/exciton-confinement in phosphorescent polymer light-emitting diodes," *Applied Physics Letters*, vol. 88, Article ID 093505, 2006.
- [11] X. W. Chen, W. C. H. Choy, C. J. Liang, P. K. A. Wai, and S. He, "Modifications of the exciton lifetime and internal quantum efficiency for organic light-emitting devices with a weak/strong microcavity," *Applied Physics Letters*, vol. 91, Article ID 221112, 2007.
- [12] N. Tessler, "Transport and optical modeling of organic lightemitting diodes," *Applied Physics Letters*, vol. 77, Article ID 1897, 2000.
- [13] D. L. Dexter, "A theory of sensitized luminescence in solids," Journal of Chemical Physics, vol. 21, p. 836, 1953.
- [14] T. Mori and T. Mizutani, "Application of energy transfer model to partially DCM-doped Alq3 light-emitting diode," *Polymers for Advanced Technologies*, vol. 8, pp. 471–476, 1997.
- [15] L. I. Liu, N. N. Baashkov, C. P. Palsule, S. Gangopadhyay, and W. L. Borst, "Intermolecular energy transfer in binary systems of dye polymers," *Journal of Applied Physics*, vol. 88, p. 4860, 2000.
- [16] C. L. Lee, K. B. Lee, and J. J. Kim, "Polymer phosphorescent light-emitting devices doped with tris(2-phenylpyridine) iridium as a triplet emitter," *Applied Physics Letters*, vol. 77, p. 2280, 2000.
- [17] S. Lamansky, R. C. Kwong, M. Nugent, P. I. Djurovich, and M. E. Thompson, "Molecularly doped polymer light emitting diodes utilizing phosphorescent Pt(II) and Ir(III) dopants," *Organic Electronics*, vol. 2, no. 1, pp. 53–62, 2001.
- [18] S. C. Chang, G. F. He, F. C. Chen, T. F. Guo, and Y. Yang, "Degradation mechanism of phosphorescent-dye-doped polymer light-emitting diodes," *Applied Physics Letters*, vol. 79, p. 2088, 2001.
- [19] P. A. Lane, L. C. Palilis, D. F. O'Brien et al., "Origin of electrophosphorescence from a doped polymer light emitting diode," *Physical Review B*, vol. 63, no. 23, Article ID 235206, pp. 2352061–2352068, 2001.
- [20] D. F. O'Brien, C. Giebeler, R. B. Fletcher et al., "Electrophosphoresence from a doped polymer light emitting diode," *Synthetic Metals*, vol. 116, no. 1–3, pp. 379–383, 2001.

- [21] M. A. Baldo, D. F. O'Brien, Y. You et al., "Highly efficient phosphorescent emission from organic electroluminescent devices," *Nature*, vol. 395, no. 6698, pp. 151–154, 1998.
- [22] D. F. O'Brien, M. A. Baldo, M. E. Thompson, and S. R. Forrest, "Improved energy transfer in electrophosphorescent devices," *Applied Physics Letters*, vol. 74, no. 3, pp. 442–444, 1999.
- [23] V. Cleave, G. Yahioglu, P. Le Barny, R. Friend, and N. Tessler, "Harvesting Singlet and Triplet Energy in Polymer LEDs," *Advanced Materials*, vol. 11, p. 285, 1999.
- [24] X. Gong, J. C. Ostrowski, G. C. Bazan, D. Moses, and A. J. Heeger, "Red electrophosphorescence from polymer doped with iridium complex," *Applied Physics Letters*, vol. 81, no. 20, pp. 3711–3713, 2002.
- [25] T. Tsuzuki, N. Shirasawa, T. Suzuki, and S. Tokito, "Color tunable organic light-emitting diodes using pentafluorophenyl-substituted iridium complexes," *Advanced Materials*, vol. 15, no. 17, pp. 1455–1458, 2003.
- [26] C. Adachi, M. A. Baldo, S. R. Forrest, and M. E. Thompson, "High-efficiency organic electrophosphorescent devices with tris(2-phenylpyridine)iridium doped into electrontransporting materials," *Applied Physics Letters*, vol. 77, p. 904, 2000
- [27] A. G. Williams, S. Develay, D. L. Rochester, and L. Murphy, "Optimising the luminescence of platinum(II) complexes and their application in organic light emitting devices (OLEDs)," *Coordination Chemistry Reviews*, vol. 252, p. 2596, 2008.
- [28] P. I. Kvam, M. V. Puzyk, K. P. Balashev, and J. Songstad, "Spectroscopic and electrochemical properties of some mixed-ligand cyclometalated platinum(II) complexes derived from 2-phenylpyridine," Acta Chemica Scandinavica, vol. 49, p. 335, 1995.
- [29] J. Brooks, Y. Babayan, S. Lamansky et al., "Synthesis and characterization of phosphorescent cyclometalated platinum complexes," *Inorganic Chemistry*, vol. 41, no. 12, pp. 3055– 3066, 2002.
- [30] J. S. Park, W. S. Jeon, J. H. Yu, R. Pode, and J. H. Kwon, "Efficiency optimization of green phosphorescent organic light-emitting device," *Thin Solid Films*, vol. 519, no. 10, pp. 3259–3263, 2011.
- [31] W. S. Jeon, T. J. Park, S. Y. Kim, R. Pode, J. Jang, and J. H. Kwon, "Ideal host and guest system in phosphorescent OLEDs," *Organic Electronics*, vol. 10, no. 2, pp. 240–246, 2009.
- [32] R. C. Kwong, M. R. Nugent, L. Michalski et al., "High operational stability of electrophosphorescent devices," *Applied Physics Letters*, vol. 81, no. 1, pp. 162–164, 2002.
- [33] J. H. Yu, W. S. Jeon, J. S. Park, R. Pode, and J. H. Kwon, "Low-voltage, simple-structure, high-efficiency p-i-n-type electrophosphorescent blue organic light-emitting diodes," *Japanese Journal of Applied Physics*, vol. 49, no. 10, pp. 1021021–1021024, 2010.
- [34] H. S. Lee, S. Y. Ahn, J. H. Seo, Y. K. Kim, and Y. Ha, "Synthesis and luminescence study of red phosphorescent iridium pyrazolonate complexes for OLED," *Journal of the Korean Physical Society*, vol. 55, p. 1977, 2009.
- [35] T. Wakimoto, Y. Fukuda, K. Nagayama, A. Yokoi, H. Nakada, and M. Tsuchida, "Organic EL cells using alkalinemetal compounds as electron injection materials," *IEEE Transactions* on Electron Devices, vol. 44, no. 8, pp. 1245–1248, 1997.
- [36] F. C. Chen, G. He, and Y. Yang, "Triplet exciton confinement in phosphorescent polymer light-emitting diodes," *Applied Physics Letters*, vol. 82, p. 1006, 2003.

- [37] M. A. Baldo, S. Lamansky, P. E. Burrows, M. E. Thompson, and S. R. Forrest, "Very high-efficiency green organic light-emitting devices based on electrophosphorescence," *Applied Physics Letters*, vol. 75, no. 1, pp. 4–6, 1999.
- [38] W. S. Jeon, C. Kulshreshtha, J. H. Yu, M. J. Lim, J. S. Park, and J. H. Kwon, "High efficiency green phosphorescent OLEDs with triplet exciton confinement architecture," *Current Applied Physics*, vol. 11, no. 3, pp. 311–314, 2011.
- [39] J. Y. Lee, "Effect of doping profile on the lifetime of green phosphorescent organic light-emitting diodes," *Applied Physics Letters*, vol. 89, Article ID 153503, 2006.
- [40] S. H. Kim, J. Jang, K. S. Yook, and J. Y. Lee, "Stable efficiency roll-off in phosphorescent organic light-emitting diodes," *Applied Physics Letters*, vol. 92, Article ID 023513, 2008.
- [41] R. J. Holmes, S. R. Forrest, Y. J. Tung et al., "Blue organic electrophosphorescence using exothermic host-guest energy transfer," *Applied Physics Letters*, vol. 82, no. 15, pp. 2422– 2424, 2003.
- [42] R. J. Holmes, B. W. D'Andrade, S. R. Forrest, X. Ren, J. Li, and M. E. Thompson, "Efficient, deep-blue organic electrophosphorescence by guest charge trapping," *Applied Physics Letters*, vol. 83, no. 18, pp. 3818–3820, 2003.
- [43] X. Ren, J. Li, R. J. Holmes, P. I. Djurovich, S. R. Forrest, and M. E. Thompson, "Ultrahigh energy gap hosts in deep blue organic electrophosphorescent devices," *Chemistry of Materials*, vol. 16, no. 23, pp. 4743–4747, 2004.
- [44] M. H. Tsai, H. W. Lin, H. C. Su et al., "Highly efficient organic blue electrophosphorescent devices based on 3,6-bis(triphenylsilyl)carbazole as the host material," *Advanced Materials*, vol. 18, p. 1216, 2006.
- [45] M. F. Wu, S. J. Yeh, C. T. Chen et al., "The quest for highperformance host materials for electrophosphorescent blue dopants," Advanced Functional Materials, vol. 17, p. 1887, 2007.
- [46] B. D. Chin, M. C. Suh, M. H. Kim, S. T. Lee, H. D. Kim, and H. K. Chung, "Carrier trapping and efficient recombination of electrophosphorescent device with stepwise doping profile," *Applied Physics Letters*, vol. 86, Article ID 133505, 2005.
- [47] Y. Kawamura, K. Goushi, J. Brooks, J. J. Brown, H. Sasabe, and C. Adachi, "100% phosphorescence quantum efficiency of Ir(III) complexes in organic semiconductor films," *Applied Physics Letters*, vol. 86, Article ID 071104, 2005.
- [48] T. J. Park, W. S. Jeon, J. J. Park et al., "Driving voltage reduction and efficiency increase by narrow bandgap host materials in phosphorescent organic light-emitting diodes," *Thin Solid Films*, vol. 517, no. 2, pp. 896–900, 2008.
- [49] N. Matsusue, S. Ikame, Y. Suzuki, and H. Naito, "Charge carrier transport in an emissive layer of green electrophosphorescent devices," *Applied Physics Letters*, vol. 85, no. 18, pp. 4046–4048, 2004.
- [50] A. Sustikov, Y. You, M. E. Thompson, and B. J. Schwartz, "Electroluminescence color tuning by dye doping in organic light-emitting diodes," *IEEE Journal of Selected Topics in Quantum Electronics*, vol. 4, pp. 3–13, 1998.
- [51] F. Pschenitzka and J. C. Sturm, "Excitation mechanisms in dye-doped organic light-emitting devices," *Applied Physics Letters*, vol. 79, p. 4354, 2001.
- [52] M. Uchida, C. Adachi, T. Koyama, and Y. Taniguchi, "Charge carrier trapping effect by luminescent dopant molecules in single-layer organic light emitting diodes," *Journal of Applied Physics*, vol. 86, no. 3, pp. 1680–1687, 1999.

- [53] J. Shen and J. Yang, "Physical mechanisms in double-carrier trap-chargelimited transport processes in organic electroluminescent devices: a numerical study," *Journal of Applied Physics*, vol. 83, p. 7706, 1998.
- [54] J. Yang and J. Shen, "Doping effects in organicelectroluminescent devices," *Journal of Applied Physics*, vol. 84, p. 2105, 1998.
- [55] L. I. Liu, N. N. Barashkov, C. P. Palsule, S. Gangopadhyay, and W. L. Borst, "Intermolecular energy transfer in binary systems of dye polymers," *Journal of Applied Physics*, vol. 88, no. 8, pp. 4860–4870, 2000.
- [56] I. Tanaka and S. Tokito, "Energy-transfer processes between phosphorescent guest and fluorescent host molecules in phosphorescent OLEDs," in *Highly Efficient OLEDs with Phos*phorescent Materials, H. Yersin, Ed., Wiley-VCH, Weinheim, Germany, 2008.
- [57] T. Förster, "10th Spiers Memorial Lecture. Transfer mechanisms of electronic excitation," *Discussions of the Faraday Society*, vol. 27, pp. 7–17, 1959.
- [58] D. L. Dexter, "A theory of sensitized luminescence in solids," *Journal of Chemical Physics*, vol. 21, no. 5, pp. 836–850, 1953.
- [59] T. Tsuzuki and and S. Tokito, "Highly efficient and low-voltage phosphorescent organic light-emitting diodes using an iridium complex as the host material," *Advanced Materials*, vol. 19, pp. 276–280, 2007.
- [60] H. H. Liao, H. F. Meng, S. F. Horng et al., "Triplet exciton energy transfer in polyfluorene doped with heavy metal complexes studied using photoluminescence and photoinduced absorption," *Physical Review B*, vol. 74, Article ID 245211, 2006.
- [61] V. Adamovich, J. Brooks, A. Tamayo et al., "High efficiency single dopant white electrophosphorescent light emitting diodesy," *New Journal of Chemistry*, vol. 26, no. 9, pp. 1171– 1178, 2002.
- [62] C. Adachi, M. E. Thompson, and S. R. Forrest, "Architectures for efficient electrophosphorescent organic light-emitting devices," *IEEE Journal on Selected Topics in Quantum Electronics*, vol. 8, no. 2, pp. 372–377, 2002.
- [63] S. Tokito, T. Iijima, Y. Suzuri, H. Kita, T. Tsuzuki, and F. Sato, "Confinement of triplet energy on phosphorescent molecules for highly-efficient organic blue-light-emitting devices," *Applied Physics Letters*, vol. 83, no. 3, pp. 569–571, 2003
- [64] W. S. Jeon, T. J. Park, S. Y. Kim, R. Pode, J. Jang, and J. H. Kwon, "Low roll-off efficiency green phosphorescent organic lightemitting devices with simple double emissive layer structure," *Applied Physics Letters*, vol. 93, Article ID 063303, 2008.
- [65] S. H. Kim, J. Jang, and J. Y. Lee, "Relationship between host energy levels and device performances of phosphorescent organic light-emitting diodes with triplet mixed host emitting structure," *Applied Physics Letters*, vol. 91, Article ID 083511, 2007.
- [66] M. Ikai, S. Tokito, Y. Sakamoto, T. Suzuki, and Y. Taga, "Highly efficient phosphorescence from organic light-emitting devices with an exciton-block layer," *Applied Physics Letters*, vol. 79, no. 2, pp. 156–158, 2001.
- [67] S. Watanabe, N. Ide, and J. Kido, "High-efficiency green phosphorescent organic light-emitting devices with chemically doped layers," *Japanese Journal of Applied Physics*, vol. 46, p. 1186, 2007.
- [68] N. Matsumoto, T. Miyazaki, M. Nishiyama, and C. Adachi, "Efficient deep-blue organic light-emitting diodes based on

- 9,9-Bis(4-biphenylyl)fluorene derivatives," *Journal of Physical Chemistry C*, vol. 113, no. 15, pp. 6261–6266, 2009.
- [69] M. A. Baldo, C. Adachi, and S. R. Forrest, "Transient analysis of organic electrophosphorescence. II. Transient analysis of triplet-triplet annihilation," *Physical Review B*, vol. 62, no. 16, pp. 10967–10977, 2000.
- [70] Y. Kawamura, J. Brooks, J. Brown, H. Sasabe, and C. Adachi, "Intermolecular interaction and a concentration-quenching mechanism of phosphorescent Ir(III) complexes in a solid film," *Physical Review Letters*, vol. 96, Article ID 017404, 2006.
- [71] C. Adachi, M. A. Baldo, S. R. Forrest, S. Lamansky, M. E. Thompson, and R. C. Kwong, "High-efficiency red electrophosphorescence devices," *Applied Physics Letters*, vol. 78, no. 11, pp. 1622–1624, 2001.
- [72] Y. Kawamura, S. Yanagida, and S. R. Forrest, "Energy transfer in polymer electrophosphorescent light emitting devices with single and multiple doped luminescent layers," *Journal of Applied Physics*, vol. 92, p. 87, 2007.
- [73] A. Tsuboyama, H. Iwawaki, M. Furugori et al., "Homoleptic cyclometalated iridium complexes with highly efficient red phosphorescence and application to organic light-emitting diode," *Journal of the American Chemical Society*, vol. 125, no. 42, pp. 12971–12979, 2003.
- [74] M. A. Baldo, M. E. Thompson, and S. R. Forrest, "Phosphorescent materials for application to organic light emitting devices," *Pure and Applied Chemistry*, vol. 71, no. 11, pp. 2095– 2106, 1999.
- [75] J. Y. Lee, "Intramolecular energy transfer in heteroleptic red phosphorescent dopants," *Applied Physics Letters*, vol. 89, Article ID 223517, 2006.
- [76] C. H. Chien, F. M. Hsu, C. F. Shu, and Y. Chi, "Efficient red electrophosphorescence from a fluorene-based bipolar host material," *Organic Electronics*, vol. 10, no. 5, pp. 871–876, 2009.
- [77] Y. L. Tung, S. W. Lee, Y. Chi et al., "Organic light-emitting diodes based on charge-neutral Os(II) emitters: generation of saturated red emission with very high external quantum efficiency," *Journal of Materials Chemistry*, vol. 15, no. 4, pp. 460–464, 2005.

Hindawi Publishing Corporation Advances in Materials Science and Engineering Volume 2012, Article ID 192731, 5 pages doi:10.1155/2012/192731

Research Article

Blue Phosphorescent Organic Light-Emitting Devices with the Emissive Layer of mCP:FCNIr(pic)

Ji Geun Jang and Hyun Jin Ji

Department of Electronics Engineering, Dankook University, San 29, Anseo-dong, Cheonan, Chungnam 330-714, Republic of Korea

Correspondence should be addressed to Ji Geun Jang, semicgk@dankook.ac.kr

Received 15 February 2012; Accepted 17 April 2012

Academic Editor: Etienne Baranoff

Copyright © 2012 J. G. Jang and H. J. Ji. This is an open access article distributed under the Creative Commons Attribution License, which permits unrestricted use, distribution, and reproduction in any medium, provided the original work is properly cited.

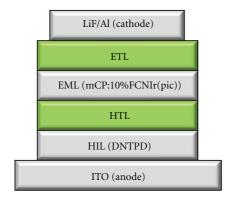
New high-efficiency blue-light-emitting phosphorescent devices with 300 Å-thick emissive layer of N,N'-dicarbazolyl-3,5-benzene [mCP] doped with 10 vol.% bis[(3,5-difluoro-4-cyanophenyl)pyridine]iridium picolinate [FCNIr(pic)] were fabricated with the different treatments of hole and electron transport layers. In the experiments, a single layer of 1,1-bis-(di-4-polyaminophenyl)cyclohexane [TAPC] and a double layer of N,N'-di(1-naphthyl)-N,N'-diphenylbenzidine [NPB] and mCP were used as hole transport layers (HTLs). In addition, 500 Å-thick double layers of tris-[3-(3-pyridyl)mesityl]borane [3TPYMB] and 4,7-diphenyl-1,10-phenanthroline [Bphen] were used as electron transport layers (ETLs) with various thickness combination of 3TPYMB/Bphen. Among the fabricated devices, the one using TAPC as an HTL and 3TPYMB(100 Å)/Bphen(400 Å) as an ETL showed best electroluminescent characteristics with a maximum quantum efficiency of 13.3% and a luminance of 950 cd/m² at 10 V. The color coordinates were (0.14, 0.22) on the Commission Internationale de l'Eclairage (CIE) chart, and the electroluminescent spectra showed the double-peak emissions at 458 nm and 483 nm.

1. Introduction

Organic light-emitting devices (OLEDs) have been intensively investigated for their applications in the solid-state lightings as well as full-color displays [1, 2]. Though the blue phosphorescent organic light-emitting diodes (PhOLEDs) are essential for the development of all phosphorescent active matrix OLEDs, highly efficient blue PhOLEDs are hard to obtain due to the large energy gap of dopants, which lead to insufficient carrier injection and exciton confinement. In the blue PhOLEDs, triplet of dopant should be larger than 2.7 eV for blue emission. Therefore, the use of host with wide energy gap is necessary because triplet of host shoud be larger than that of dopant in the hostdopant system of an emissive layer. The well-known host material in the blue PhOLEDs is mCP. It has a good hole transport property due to a carbazole unit in the backbone structure and a large triplet of 2.9 eV for efficient energy transfer [3]. Iridium(III) bis((4,6-difluorophenyl)pyridinate-N,C2')picolinate [FIrpic] is the most well-known

blue phosphorescent dopant [4]. Kawamura et al. demonstrated that the photoluminescence internal quantum yield of the blue emitter of FIrpic could approach nearly 100% when doped into the wide energy gap host of mCP [5]. However, the theoretical electrophosphorescence is difficult to carry out because of the lack of highly efficient carrier transport materials with wide energy gap for sufficient carrier injection and exciton confinement. Furthermore, color performances of the FIrpic-based devices were poor with the vertical coordinates of more than 0.3 on the CIE chart

The quantum efficiency remarkably decreases due to carrier injection loss, nonradiative relaxation of excitons, triplet-triplet annihilation at high current density, and so forth [6, 7]. The triplets have rather long lifetime so that they may diffuse to the neighbor layers by passing through an emissive layer. This effect also results in the declination of luminous efficiency and color purity due to energy transfer and relaxation of excitons outside the emissive layer. Therefore, the structural design of PhOLEDs which can



Device classifications	HTL	ETL	
Device A	NPB (300 Å)/mCP (100 Å)	3TPYMB (100 Å)/Bphen(400 Å)	
Device B	TAPC (300 Å)	3TPYMB (100 Å)/Bphen(400 Å)	
Device C	TAPC (300 Å)	Bphen (500 Å)	
Device D	TAPC (300 Å)	3TPYMB (150 Å)/Bphen(350 Å)	
Device E	TAPC (300 Å)	3TPYMB (200 Å)/Bphen(300 Å)	

FIGURE 1: Basic structure and classification of the fabricated devices.

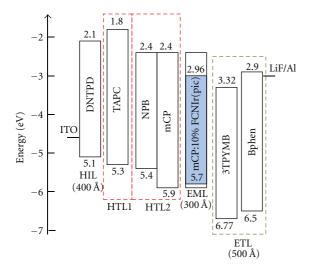


FIGURE 2: Energy band diagram of the used materials.

confine the triplet excitons in an emissive layer is extremely important to obtain high-efficiency devices.

Yook et al. reported a deep blue PhOLED with structure of N, N'-diphenyl-N,N'-bis-[4-(phenyl-m-tolylamino)-phenyl]-biphenyl-4,4'-diamine[DNTPD]/NPB/mCP /mCP: tris[(3,5-difluoro-4-cyanophenyl)pyridine]iridium[FCNIr]/Bphen in which a quantum efficiency of 9.2% and a current efficiency of 11 cd/A were obtained with a color coordinate of (0.15.0.16) at 500 cd/m² [8]. The FCNIr has a wide triplet of 2.8 eV for deep blue emission due to a strong electron withdrawing CN substituent besides *F* units.

In this work, new high efficiency blue-light-emitting phosphorescent devices with an emissive layer of mCP doped with FCNIr(pic) were fabricated and evaluated according to the treatments of hole and electron transport layers.

In the experiments, the electroluminescent characteristics of the devices with a single layer of TAPC and a double layer of NPB/mCP as an HTL were compared. In addition, the double layers of 3TPYMB/Bphen were used as an electron transport layers (ETLs) with various thickness combinations of 3TPYMB/Bphen. To our knowledge, the use of the mCP: FCNIr(pic) emitter as well as the adoption of the

TAPC as an HTL and the 3TPYMB/Bphen double layer as an ETL in the blue PhOLEDs was firstly attempted in this paper.

2. Experimental Procedure

The substrates with an ITO (indium tin oxide) anode of $12\,\Omega/\text{sq}$ on glass were cleaned by ultrasonic cleaning process with acetone and isopropyl alcohol. The remaining solvent was removed by soft baking for 10 minutes at 100°C . To improve the surface morphology of ITO transparent electrode film, the substrates were plasma treated at $150\,\text{W}$ for two minutes under 8 mTorr pressure of O_2/Ar . The plasma treatment before deposition of the first organic layer is expected to reduce the energy barrier for hole injection from anode and remove the surface contaminants. All organic layers and cathode layers were deposited by insitu method under $5\times 10^{-8}\,\text{Torr}$.

As a sequence of deposition process, the DNTPD with thickness of 400 Å was firstly deposited as a hole injection layer. Then, two kinds of HTLs were used according to device classifications: a conventional structure of NPB(300 Å)/mCP(100 Å) was used in the device A and a single layer of TAPC(300 Å) in the other devices. Next, 300 Åthick mCP doped with 10% FCNIr(pic) as a volume ratio was deposited as an emissive layer. In the formation of ETLs, the 3TPYMB/Bphen with a total thickness of 500 Å was deposited with various 3TPYMB thicknesses according to the device classifications: the thicknesses of 3TPYMB were 100 Å in the devices (A, B), 0 Å in the device C, 150 Å in the device D, and 200 Å in the device E. Finally, 10 Å-thick LiF and 1200 Å-thick Al were successively deposited as a cathode. The structures of the fabricated devices and energy diagram of the used materials are shown in Figures 1 and 2.

3. Results and Discussion

In the energy diagram of Figure 2, the DNTPD is well known as a hole injection material with the HOMO level of 5.1 eV and the LUMO level of 2.1 eV [9]. The electrons from the anode of indium tin oxide (ITO) are easily injected into the DNTPD because its highest occupied molecular orbital (HOMO) level is similar to Fermi level of ITO. The

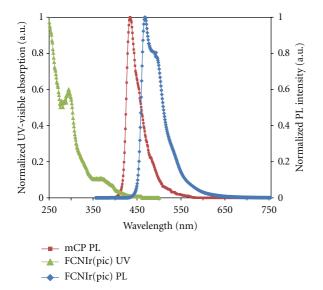


FIGURE 3: UV-visible absorption and PL spectra of FCNIr(pic) including the PL spectra of mCP.

TAPC as a hole transport material has the HOMO level of 5.3 eV and the LUMO level of 1.8 eV [10]. The triplet energy of TAPC is 2.87 eV [11] which is larger than that of FCNIr(pic) so that the triplet excitons can be effectively confined without diffusion loss into the HTL. Moreover, the electrons injected from cathode are confined in the EML due to the large LUMO offset (~0.6 eV) at the interface of the TAPC and the emissive layer. Therefore, the TAPC can be used as a good HTL in the high-efficiency blue PhOLED. With the same condition except HTL in the device structure, the electroluminescent characteristics of the device with the TAPC as an HTL were at firstly compared with those of the device with the conventional NPB/mCP as an HTL. And then, the composition effect of 3TPYMB/Bphen as an ETL on the electroluminescent characteristics of the devices with the TAPC as an HTL was investigated. Both Bphen and 3TPYMB have been used as a material of ETL in the conventional OLEDs. The triplet energy of Bphen is 2.5 eV [12] so that the Bphen cannot sufficiently confine the excitons. On the other hand, 3TPYMB has a triplet energy of 2.87 eV which is higher than the exciton energy of FCNIr(pic) and a deep HOMO level of 6.77 eV [13]. Therefore, the use of 3TPYMB as an ETL can expect an effective confinement of the excitons as well as the injected holes in the emissive layer. However, the electron mobility of 3TPYMB is much lower than that of Bphen [14]. To solve these problems, the bilayer of 3TPYMB/Bphen can be used as an ETL. The addition of a properly thick 3TPYMB to Bphen in the ETL structure can improve the electroluminescent characteristics in the blue PhOLEDs because the excitons and the injected holes are effectively confined in the emissive layer without a serious increase of current resistance.

Figure 3 shows the UV-visible absorption and photoluminescence (PL) spectra of FCNIr(pic). The PL emission peak of FCNIr(pic) was observed at 460 nm with a vibrational peak at 485 nm. The FCNIr(pic) shows a deep blue

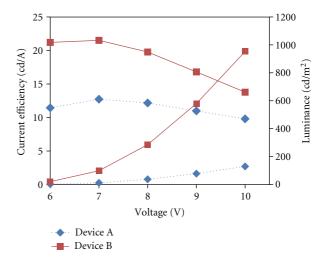


FIGURE 4: Current efficiency-voltage-luminance characteristics of the devices (A, B).

emission due to the strong electron withdrawing CN group in the phenyl unit of main ligand. The PL spectra of mCP are also shown in Figure 3. It can be clearly seen that PL spectra of mCP are overlapped with absorption of FCNIr(pic) in a range of 400~450 nm. Therefore, the efficient energy transfer from mCP to FCNIr(pic) can be expected. In addition, Dexter energy transfer between the triplets of mCP and FCNIr(pic) can be occurred because the triplet of mCP is 2.9 eV which is high compared to 2.72 eV of FCNIr(pic) [15].

The electrical properties of the devices were measured using a Polaronix M6100 test system (McScience). The optical properties such as luminance, emission spectrum, and CIE color coordinates were evaluated using a CS-1000 spectro-radiometer (Konica Minolta) in a dark room.

The current efficiency-voltage-luminance characteristics of the devices (A, B) are shown in Figure 4. In Figure 4, the maximum current efficiencies were 12.7 cd/A for the device A and 21.5 cd/A for the device B. The luminances under an applied voltage of 10 V were 130 cd/m² for the device A and 950 cd/m² for the device B. The remarkable improvement of electroluminescent characteristics in the device B compared with device A comes from the better treatment of HTL in the device B than in the device A. As a HTL in the blue PhOLEDs, the TAPC could be more ideal than the conventional NPB/mCP due to the better hole mobility, larger triplet energy and better electron confinement by a large LUMO offset at the interface of the TAPC and the emissive layer.

Figure 5 shows the current efficiency-voltage-luminance characteristic of the devices (C, D, E) compared with those of device B. The organic layer compositions of the devices (B, C, D, E) are the DNTPD/TAPC/mCP: 10%FCNIr(pic)/ETLs. The only differences of the devices (B, C, D, E) are the thicknesses of 3TPYMB in the 500 Å-thick ETL of 3TPYMB/Bphen. Among the fabricated devices, the best electroluminescent characteristics was obtained in the device B with an ETL of 3TPYMB(100 Å)/Bphen(400 Å). As it can be expected, the device C with the Bphen only as an ETL

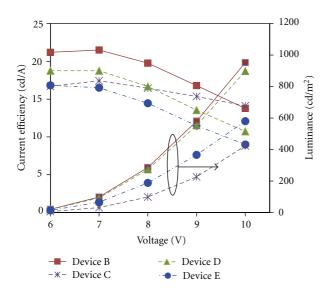


FIGURE 5: Current efficiency-voltage-luminance characteristics of the devices (C, D, E) compared with those of device B.

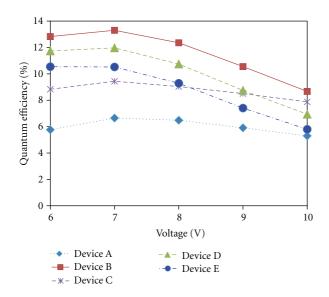


FIGURE 6: Quantum efficiency-voltage characteristics of the fabricated devices.

showed the rather poor electroluminescent characteristics because the triplet energy of Bphen is not high enough to confine the excitions. The maximum current efficiency and luminance at 10 V were 17,4 cd/A and 423 cd/m² in the device C, respectively. In the devices (D, E) with the 3TPYMB thicker than 100 Å in the ETL, the current efficiency and luminance decreased according to the increase of 3TPYMB thickness. The maximum current efficiencies were 18.8 cd/A for the device D and 16.8 cd/A for the device E. The luminance at 10 V were 900 cd/m² for the device D and 580 cd/m² for the device E. It is believed that the use of a too thick 3TPYMB in the 3TPYMB/Bphen results in the poor electroluminescent characteristics due to its low electron mobility.

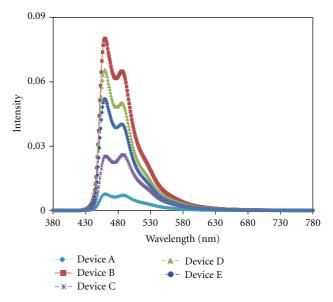


FIGURE 7: Electroluminescence spectra of the fabricated devices at 7 V.

Figure 6 shows the quantum efficiency-voltage characteristics of the fabricated devices. The best quantum efficiency-voltage characteristics was also obtained in the device B with a maximum quantum efficiency of 13.3% as shown in Figure 6.

The electroluminescence spectra at 7 V for the fabricated devices were shown in Figure 7. The Peak wavelengths were 458 nm and 483 nm, which corresponds to the typical double peak emission of FCNIr(pic). The color of the fabricated devices with a central peak at 458 nm could be evaluated to be deep blue with the color coordinates on the CIE chart of (0.14, 0.22).

From the above discussion, the new proposed device of DNTPD/TAPC/mCP: 10 vol.%FCNIr(pic)/3TPYMB/Bphen in this study can be a good blue PhOLED with high current efficiency and deep blue emission if the thicknesses of each layers are well controlled.

4. Conclusions

New high efficiency blue light-emitting phosphorescent devices with structure of DNPTD/HTL/mCP: FCNIr(pic)/ETL were fabricated and evaluated according to the different treatments of HTL and ETL. A single layer of TAPC and a double layer of NPB/mCP were compared as hole transport layers and the 3TPYMB/Bphen layers with various thickness combinations were used as electron transport layer.

Among the fabricated devices, the device B with a HTL of TAPC and an ETL of 3TPYMB(100 Å)/Bphen(400 Å) showed the best electroluminescent characteristics. It had a maximum current efficiency of 21.5 cd/A, and a luminance of 950 cd/m² at 10 V.

The color coordinates were (0.14, 0.22) on the CIE chart, and electroluminescent spectra showed the double peak emission at 458 nm and 483 nm.

As a deep blue PhOLED with the emissive layer of mCP: FCNIr(pic), the excellent electroluminescent characteristics of device B may be obtained from the adoption of TAPC with high triplet energy as a HTL and the use of a proper thick 3TPYMB combined with Bphen as an ETL.

References

- [1] B. W. D. D'Andrade and S. R. Forrest, "White organic lightemitting devices for solid-state lighting," *Advanced Materials*, vol. 16, no. 18, pp. 1585–1595, 2004.
- [2] D. Yao, S. Zhao, J. Guo et al., "Hydroxyphenyl-benzothiazole based full color organic emitting materials generated by facile molecular modification," *Journal of Materials Chemistry*, vol. 21, no. 11, pp. 3568–3570, 2011.
- [3] S. H. Kim, J. S. Jang, and J. Y. Lee, "High efficiency phosphorescent organic light-emitting diodes using carbazole-type triplet exciton blocking layer," *Applied Physics Letters*, vol. 90, no. 22, Article ID 223505, 3 pages, 2007.
- [4] Z. Wu, Y. Xiong, J. L. Zou et al., "High-Triplet-Energy Poly(9,90-bis(2-ethylhexyl)-3,6-fluorene) as Host for Blue and Green Phosphorescent Complexes," *Advanced Materials*, vol. 20, article 2359, 2008.
- [5] Y. Kawamura, K. Goushi, J. Brooks, J. Brown, H. Sasabe, and C. Adachi, "100% phosphorescence quantum efficiency of Ir(III) complexes in organic semiconductor films," *Applied Physics Letters*, vol. 86, no. 7, Article ID 071104, 3 pages, 2005.
- [6] Z. H. Zhao, J. Li, P. Lu, and Y. Yang, "Fluorescent, carrier-trapping dopants for highly efficient single-layer polyfluorene LEDs," *Advanced Functional Materials*, vol. 17, no. 13, pp. 2203–2210, 2007.
- [7] D. Beljonne, J. Cornil, R. H. Friend, R. A. J. Janssen, and J. L. Bredas, "Influence of chain length and derivatization on the lowest singlet and triplet states and intersystem crossing in oligothiophenes," *Journal of the American Chemical Society*, vol. 118, no. 27, pp. 6453–6461, 1996.
- [8] K. S. Yook, S. O. Jeon, C. W. Joo, and J. Y. Lee, "High efficiency deep blue phosphorescent organic light-emitting diodes," *Organic Electronics*, vol. 10, no. 1, pp. 170–173, 2009.
- [9] Y. M. Jeon, J. W. Kim, C. W. Lee, and M. S. Gong, "Blue organic light-emitting diodes using novel spiro[fluorene-benzofluorene]-type host materials," *Dyes and Pigments*, vol. 83, no. 1, pp. 66–71, 2009.
- [10] Y. Zhu, A. P. Kulkarni, and S. A. Jenekhe, "Phenoxazine-Based Emissive Donor-Acceptor Materials for Efficient Organic Light-Emitting Diodes," *Chemistry of Materials*, vol. 17, article 5227, 2005.
- [11] J. W. Lee, N. Chopra, S. H. Eom et al., "Effects of triplet energies and transporting properties of carrier transporting materials on blue phosphorescent organic light emitting devices," *Applied Physics Letters*, vol. 93, no. 12, Article ID 123306, 3 pages, 2008.
- [12] J. S. Park, W. S. Jeon, J. H. Yu, R. Pode, and J. H. Kwon, "Efficiency optimization of green phosphorescent organic light-emitting device," *Thin Solid Films*, vol. 519, no. 10, pp. 3259–3263, 2011.
- [13] C. Han, G. Xie, H. Xu et al., "Towards Highly Efficient Blue-Phosphorescent Organic Light-Emitting Diodes with Low Operating Voltage and Excellent Efficiency Stability," *Chemistry—A European Journal*, vol. 17, article 445, 2011.
- [14] S. H. Eom, Y. Zheng, E. Wrzesniewski et al., "Effect of electron injection and transport materials on efficiency of deep-

- blue phosphorescent organic light-emitting devices," *Organic Electronics*, vol. 10, no. 4, pp. 686–691, 2009.
- [15] S. O. Jeon, K. S. Yook, C. W. Joo, and J. Y. Lee, "High-efficiency deep-blue-phosphorescent organic light-emitting diodes using a phosphine oxide and a phosphine sulfide high-triplet-energy host material with bipolar charge-transport properties," *Advanced Materials*, vol. 22, no. 16, pp. 1872–1876, 2010.

Hindawi Publishing Corporation Advances in Materials Science and Engineering Volume 2012, Article ID 270865, 5 pages doi:10.1155/2012/270865

Research Article

LTPS-TFT Pixel Circuit Compensating for TFT Threshold Voltage Shift and IR-Drop on the Power Line for AMOLED Displays

Ching-Lin Fan,^{1,2} Min-Chi Shang,² Wei-Chun Lin,² Hsiu-Chen Chang,² Kuang-Chi Chao,¹ and Bo-Liang Guo¹

- ¹ Department of Electronic Engineering, National Taiwan University of Science and Technology, 43 Section 4, Keelung Road, Taipei 106, Taiwan
- ² Graduate Institute of Electro-Optical Engineering, National Taiwan University of Science and Technology, 43 Section 4, Keelung Road, Taipei 106, Taiwan

Correspondence should be addressed to Ching-Lin Fan, clfan@mail.ntust.edu.tw

Received 1 March 2012; Revised 29 April 2012; Accepted 8 May 2012

Academic Editor: Yong Qiu

Copyright © 2012 Ching-Lin Fan et al. This is an open access article distributed under the Creative Commons Attribution License, which permits unrestricted use, distribution, and reproduction in any medium, provided the original work is properly cited.

We propose a new pixel design for the active matrix organic light-emitting diode (AMOLED) using low-temperature polycrystalline silicon thin-film transistors (LTPS-TFTs). The proposed pixel is composed of four switching TFTs, one driving TFT (DTFT), and one capacitor. The simulation results are performed by AIM-SPICE software. The error rate of OLED output current with $V_{\rm TH}$ (threshold voltage) variation (0.3 V) and $V_{\rm dd}$ power line drop by 1 V are improved to about 1.67% and 15%, respectively. Thus, the proposed pixel circuit can successfully overcome drawbacks suffered from DTFT threshold voltage deviation and IR-drop on power line.

1. Introduction

Organic light-emitting diode (OLEDs) displays have gained considerable interest in large-area flat panel display applications due to their excellent optoelectric properties, large viewing angle, color versatility, and potentially low fabrication cost [1]. Therefore, great effort has been made to develop active matrix driving techniques for organic lightemitting diode displays making it possible to achieve large, high-resolution displays.

Recently, AMOLED driving pixel circuits are composed of amorphous silicon thin-film transistors (a-Si TFTs) or low-temperature polysilicon thin film transistors (LTPS-TFTs). It is no doubt that LTPS-TFTs are suitable as switching and driving devices for AMOLED because of their outstanding driving capability due to the higher mobility, which can approach more practical and powerful applications [2]. However, the LTPS-TFT manufacturing process will cause nonuniform electrical characteristics such as threshold voltage variations in pixels, depending on the fluctuations in excimer laser energy, resulting in uncontrollable gate oxide trap density and irregular grain boundary distribution

in the polySilicon material [3-5]. In the typical p-type 2-TFT pixel circuit, the supply power line is connected to the DTFT source node. The output current suffers from parasitic resistance on the supply power lines. The parasitic resistance may lead to power dissipation, called $I \times R$ voltage drop. This is inevitable by Ohm's Law and will cause non-uniform luminance in the panel [6]. To solve the nonuniformity issue caused by V_{TH} variation and $I \times R$ dropvoltage, several methods have been proposed [7-13]. The current programming method effectively compensates for the threshold voltage variation and field-effect mobility shifts in TFTs. However, it requires longer charging time at the data lines compared with the voltage programming method. Thus, voltage programming methods are more suitable in large-size displays. However, most of these studies could not compensate for both the DTFT threshold voltage variation and the $I \times R$ voltage drop at the same time. Comparatively, our compensation methods can overcome both critical issues and still preserve stable driving ability.

This paper describes a new voltage programming pixel circuit based on the LTPS technology. The proposed pixel circuit has high immunity to DTFT threshold voltage

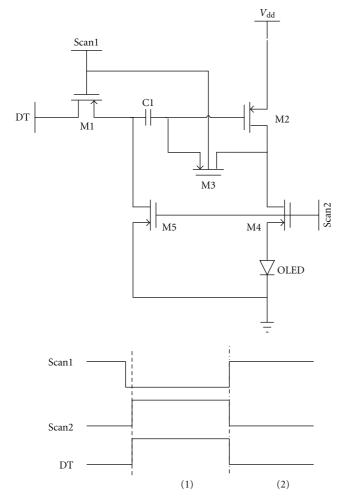


FIGURE 1: Signal lines for the proposed pixel circuit design and timing scheme.

variation and can simultaneously compensate for the voltage drop on the power line. Compared with conventional 2-TFT pixel, the simulation results demonstrate that the output current error rate and its degradation rate are improved by 1.67% and 4% due to DTFT $V_{\rm TH}$ variation ($\pm 0.3 \, {\rm V}$) and $V_{\rm dd}$ drop of 0.3 V, respectively. We believe that the proposed pixel circuit is a good candidate for large-size, high-resolution AMOLED applications.

2. Proposed Pixel Circuit and Driving Method

Figure 1 demonstrates the proposed schematic pixel circuit based on poly-Si TFTs and its signal line driving scheme. The pixel consists of four switching TFTs (M1, M3, M4, and M5), one p-type driving TFT (M2), and one capacitor. The driving scheme has two selection lines (Scan1, and Scan2) and a data line (DT). M1 is a selection switch. M3 is used for the diode connection with M2, and M4 is used for blocking current through the OLED during the compensation period, respectively. We can modify this pixel circuit for all p-type TFT structures by adding an additional control line for M3, which can be more advantageous for manufacturing. The

operation of the proposed circuit is divided into two periods: data input and compensation period; emission period. The following statements depict each operating period. During the period before (1), the high- and low-voltage signals are applied to the Scan1 and Scan2, respectively. During this period, it is the previous frame operation for the same pixel and the DT voltage which was set to 0 V.

As shown in the period of Figure 2. Scan1 is set to the low level to turn on M1 and M3. Scan2 is set to high level to turn off M4 and M5 at the same time. The M2 gate node is connected to the M2 drain node. At present, the input signal ($V_{\rm data}$), which is applied to data line (DT) delivered by M1, is stored on the left side of C1. In addition, by the M4 turnoff, we can turn off the OLED in this period to increase the OLED lift time in long-time operation. Because of the diode-connected structure of M2, the M2 gate node becomes $V_{\rm dd} - |V_{\rm TH}|$, where $V_{\rm TH}$ is the M2 threshold voltage, and $V_{\rm dd}$ is the supply power line voltage. The stored voltage across C1 is set to $V_{\rm dd} - |V_{\rm TH}| - V_{\rm data}$. The C1 reset and compensation stages can be finished at the same time in the period (1).

(2) Emission Period. As shown in the period (2) of the Figure 2. Scan1 is set to high level to turn off M1, and Scan2 is set to low level to turn off M3, while it turns on M4 and M5. The M2 drain node is connected to the OLED anode. The left side of C1 is connected to ground. Consequently, the M2 gate voltage will be boosted to $V_{\rm dd} - |V_{\rm TH}| - V_{\rm data}$, coupling in the first period. Accordingly, $I_{\rm OLED}$ is determined by the $V_{\rm SG}$ of M2 and operated in the saturation region which becomes as follows:

$$I_{\text{OLED}} = \frac{1}{2} K_{M2} (V_{\text{SG}} - |V_{\text{TH}}|)^{2}$$

$$= \frac{1}{2} K_{M2} [V_{\text{dd}} - (V_{\text{dd}} - |V_{\text{TH}}| - V_{\text{data}}) - |V_{\text{TH}}|]^{2}$$

$$= \frac{1}{2} K_{M2} (V_{\text{data}})^{2}, \quad \left(K = \mu C_{\text{OX}} \frac{W}{L}\right). \tag{1}$$

Therefore, $I_{\rm OLED}$ is independent of the M2 threshold voltage variation and the voltage-drop of the power line ($V_{\rm dd}$), only decided by $V_{\rm data}$.

In addition, the time constant is well known as RC delay time. The minimum required time for period (1) is dependent on the RC value that you designed. Thus, the capacitance area will affect the aperture area in the pixel. The smaller the capacitance area is, the larger the aperture ratio is.

3. Proposed Circuit Simulation Results

To verify the effectiveness of the proposed 5T1C pixel circuit further, we did an AIM-SPICE simulation. The TFT model used in the simulation was poly-Si TFT Model PSIA2 (level 16). The OLED model is equivalent to a diode-connected poly-Si TFT and a capacitor. The M2 threshold voltage is set to -1 V. The M2 threshold voltage variation is set to ± 0.3 V to validate it in the worst-case process. To generate enough OLED output current, the width and length of M2 is designed as $10~\mu{\rm m}$ and $4~\mu{\rm m}$. The high- and low-level signals

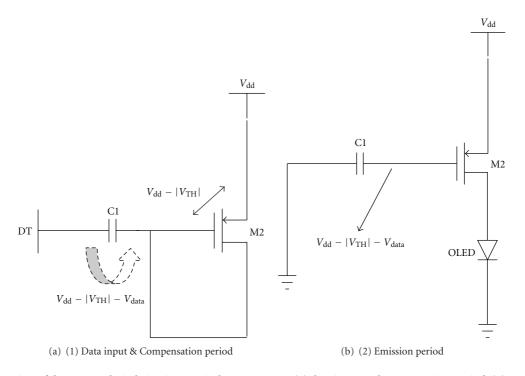


FIGURE 2: Operation of the proposed pixel circuit in equivalent two stages: (1) data input and compensation period, (2) emission period.

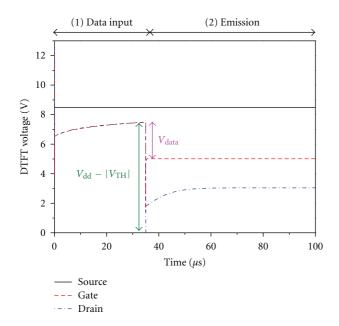


FIGURE 3: Gate, source, and drain voltages of driving TFT (DTFT) with operation stages: (1) Data input and compensation period; (2) Emission period when $V_{\rm data} = 2.5 \, \rm V$.

(Scan1 and Scan2) were set to $-5-11.5\,\mathrm{V}$ and $-11.5-11.5\,\mathrm{V}$, respectively.

Figure 3 shows the voltage of each node of DTFT when the data voltage is 2.5 V. The two-stage circuit operation is denoted by the notations (1) and (2). At the data input and

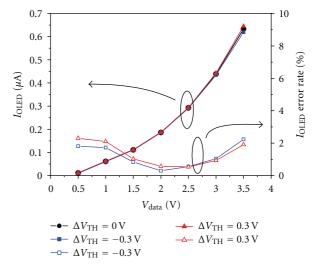


Figure 4: OLED output current simulation results and error rate at different $V_{\rm data}$ and threshold voltage variations.

compensation stage (1), the DTFT gate voltage is charged up to 7.5 V ($V_{\rm dd} - |V_{\rm TH}|$). Then, the $V_{\rm data} = 2.5$ V is input to set DTFT gate voltage to 5 V ($V_{\rm dd} - |V_{\rm TH}| - V_{\rm data}$). During the emission stage (2), the $V_{\rm SG}$ of the DTFT is $|V_{\rm TH}| + V_{\rm data}$, and the DTFT is operated in the saturation region. The proposed circuit successfully compensates for the threshold voltage degradation originating from the DTFT.

Figure 4 shows the simulation results for the proposed 5T1C pixel circuit at different V_{data} (0.5–3.5 V) according to

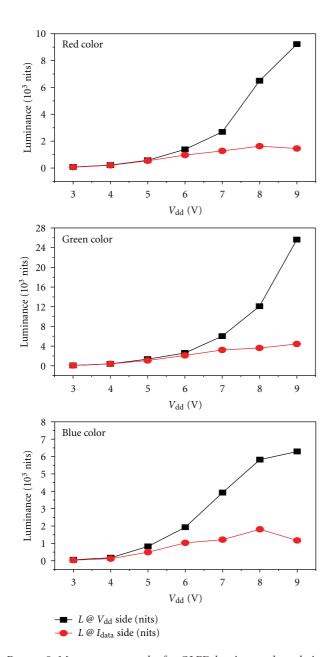


FIGURE 5: Measurement results for OLED luminance degradation for each RGB element in conventional 2-TFT pixel circuit.

the M2 threshold voltage variation ($\Delta V_{\rm TH} = \pm 0.3$ V, 0 V). Obviously, $I_{\rm OLED}$ is nearly independent of the threshold voltage variation. Moreover, the average $I_{\rm OLED}$ error rate in Figure 2 is 1.67%, while it is about 30–40% in the conventional 2-TFTs pixel.

Figure 5 shows the luminance data measured by PR-705 for the 2.2-inch QCIF (176 \times RGB \times 220) bottom-emission AMOLED panel, which is driven using p-type conventional 2-TFTs pixel. In this panel, $V_{\rm dd}$ side and $I_{\rm data}$ side were defined as the beginning and end of the supply power line, respectively. The luminance data is measured at $V_{\rm dd}$ side and $I_{\rm data}$ side, for each RGB elements, the luminance degradation rate, which is the luminance difference between $V_{\rm dd}$ side

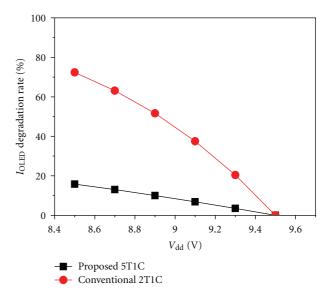


FIGURE 6: Comparison of output current degradation rate versus $V_{\rm dd}$ drop for conventional 2T1C pixel circuit and proposed pixel circuit.

and $I_{\rm data}$ side, is about 70–80% at the input of $V_{\rm dd}=9~\rm V$. The degradation of the measured luminance reveals that conventional panel which is driven by 2-TFT pixel seriously suffered from $V_{\rm GS}$ drop in driving TFT caused by power line $I\times R$ voltage-drop, which means the source terminal voltage of DTFT ($V_{\rm dd}$) will cause the above phenomenon. The luminance uniformity is extremely dependent on the $I\times R$ voltage-drop. In addition, luminance uniformity and $I_{\rm OLED}$ are in direct proportion.

Figure 6 shows the simulation results of $I_{\rm OLED}$ degradation rate compared with conventional 2-TFTs pixel circuit. The initial $V_{\rm dd}$ was set to 9.5 V and the $I \times R$ voltage-drop of $V_{\rm dd}$ was set to 1 V, which means it decays from 9.5 V to 8.5 V. In the conventional 2-TFTs pixel, the $I_{\rm OLED}$ degradation rate is about 72%. It was found that the normalized degradation rate of the output current caused by the power line $I \times R$ voltage drop was apparently improved for the conventional and proposed pixel, respectively. In addition, the degradation rate of the output current, while $V_{\rm dd}$ drop of 0.3 V is improved by about 4%. We believe that our proposed pixel circuit can successfully solve both the threshold voltage variation and the power line $I \times R$ drop-voltage influence.

4. Conclusions

A new voltage programming pixel circuit was proposed for application to large-size, high-resolution AMOLED displays. The new pixel design can successfully compensate for the driving TFT threshold voltage non-uniform deviation. The average OLED output current error rate is about 1.67% when the threshold voltage is varied by ± 0.3 V. It also has less sensitivity to the supply power line voltage-drop than conventional p-type 2-TFT pixel designs.

Acknowledgments

The authors would like to acknowledge the financial support from the National Science Council (NSC) under contract number NSC 98-2221-E-011-141 and NSC 100-2221-E-011-016 and technical support from Active-Matrix and Full-Color Department, RiTdisplay Corporation, Taiwan.

References

- [1] M. Stewart, R. S. Howell, L. Pires, M. K. Hatalis, W. Howard, and O. Prache, "Polysilicon VGA active matrix OLED displays—technology and performance," in *Proceedings of the IEEE International Electron Devices Meeting*, pp. 871–874, December 1998.
- [2] C. L. Fan, Y. Y. Lin, B. S. Lin, J. Y. Chang, C. L. Fan, and H. C. Chang, "New pixel circuit compensating poly-si TFT threshold-voltage shift for a driving AMOLED," *Journal of the Korean Physical Society*, vol. 56, no. 4, pp. 1185–1189, 2010.
- [3] J. H. Lee, W. J. Nam, S. H. Jung, and M. K. Han, "A new current scaling pixel circuit for AMOLED," *IEEE Electron Device Letters*, vol. 25, no. 5, pp. 280–282, 2004.
- [4] H. Aziz, "Degradation mechanism of small molecule-based organic light-emitting devices," *Science*, vol. 283, no. 5409, pp. 1900–1902, 1999.
- [5] T. F. Chen, C. F. Yeh, and J. C. Lou, "Investigation of grain boundary control in the drain junction on laser-crystalized poly-Si thin film transistors," *IEEE Electron Device Letters*, vol. 24, no. 7, pp. 457–459, 2003.
- [6] S. H. Jung, W. J. Nam, and M. K. Han, "A new voltage-modulated AMOLED pixel design compensating for threshold voltage variation in Poly-Si TFTs," *IEEE Electron Device Letters*, vol. 25, no. 10, pp. 690–692, 2004.
- [7] C. L. Fan, Y. S. Lin, and Y. W. Liu, "Low temperature polycrystalline silicon thin film transistor pixel circuits for active matrix organic light emitting diodes," *IEICE Transactions on Electronics*, vol. 93, no. 5, pp. 712–714, 2010.
- [8] C. W. Lin, D. Z. Pang, R. Lee et al., "Advanced poly-Si device and circuitry for AMOLED and high-integration AMLCD," in *Proceedings of the International Display Manufacturing* Conference and Exhibition (IDMC '05), pp. 315–318, February 2005.
- [9] H. J. In and O. K. Kwon, "External compensation of nonuniform electrical characteristics of thin-film transistors and degradation of OLED devices in AMOLED displays," *IEEE Electron Device Letters*, vol. 30, no. 4, pp. 377–379, 2009.
- [10] T. W. Kim and B. D. Choi, "Pixel-level digital-to-analog conversion scheme for compact data drivers of active matrix organic light-emitting diodes with low-temperature polycrystalline silicon thin-film transistors," *Japanese Journal of Applied Physics*, vol. 49, no. 3, Article ID 03CD03, 2010.
- [11] C. L. Lin, K. W. Chou, C. C. Hung, and C. D. Tu, "Lifetime amelioration for an AMOLED pixel circuit by using a novel AC driving scheme," *IEEE Transactions on Electron Devices*, vol. 58, no. 8, pp. 2652–2659, 2011.
- [12] W. J. Wu, L. Zhou, R. H. Yao, and J. B. Peng, "A new voltage-programmed pixel circuit for enhancing the uniformity of AMOLED displays," *IEEE Electron Device Letters*, vol. 32, no. 7, pp. 931–933, 2011.
- [13] J. H. Lee, J. H. Kim, and M. K. Han, "A new a-Si:H TFT pixel circuit compensating the threshold voltage shift of a-Si:H TFT and OLED for active matrix OLED," *IEEE Electron Device Letters*, vol. 26, no. 12, pp. 897–899, 2005.

Hindawi Publishing Corporation Advances in Materials Science and Engineering Volume 2012, Article ID 985762, 9 pages doi:10.1155/2012/985762

Research Article

Enhancing the Out-Coupling Efficiency of Organic Light-Emitting Diodes Using Two-Dimensional Periodic Nanostructures

Qingyang Yue, Wei Li, Fanmin Kong, and Kang Li

School of Information Science and Engineering, Shandong University, Jinan 250100, China

Correspondence should be addressed to Kang Li, kangli@sdu.edu.cn

Received 10 March 2012; Revised 17 April 2012; Accepted 19 April 2012

Academic Editor: Jwo-Huei Jou

Copyright © 2012 Qingyang Yue et al. This is an open access article distributed under the Creative Commons Attribution License, which permits unrestricted use, distribution, and reproduction in any medium, provided the original work is properly cited.

The out-coupling efficiency of planar organic light emitting diodes (OLEDs) is only about 20% due to factors, such as, the total internal reflection, surface plasmon coupling, and metal absorption. Two-dimensional periodic nanostructures, such as, photonic crystals (PhCs) and microlenses arrays offer a potential method to improve the out-coupling efficiency of OLEDs. In this work, we employed the finite-difference time-domain (FDTD) method to explore different mechanisms that embedded PhCs and surface PhCs to improve the out-coupling efficiency. The effects of several parameters, including the filling factor, the depth, and the lattice constant were investigated. The result showed that embedded PhCs play a key role in improving the out-coupling efficiency, and an enhancement factor of 240% was obtained in OLEDs with embedded PhCs, while the enhancement factor of OLEDs with surface PhCs was only 120%. Furthermore, the phenomena was analyzed using the mode theory and it demonstrated that the overlap between the mode and PhCs was related to the distribution of vertical mode profiles. The enhancement of the extraction efficiency in excess of 290% was observed for the optimized OLEDs structure with double PhCs. This proposed structure could be a very promising candidate for high extraction efficiency OLEDs.

1. Introduction

Due to the advantages of a wide viewing angle, a low operating voltage, a fast response time, and flexibility, organic light emitting diodes (OLEDs) have rapidly progressed in recent years and have been successfully applied in flat panel displays and solid-state lighting [1–3]. The extraction efficiency $\eta_{\rm ext}$ is related to the internal quantum efficiency $\eta_{\rm int}$ of the organic material and the out-coupling efficiency $\eta_{\rm out}$ of the multilayer planar structure:

$$\eta_{\text{ext}} = \eta_{\text{int}} \eta_{\text{out}}.$$
(1)

The intrinsic efficiency has been considerably improved by the use of phosphorescent harvesters [4]. However, the outcoupling efficiency of OLEDs remains very poor (it is only about 20%). This arises from Snell's law. Because of the high refractive index of indium-tin-oxide (ITO)/organic layers and substrate layer, only a small fraction of total light is able to escape from the light-emitting dielectric medium into the air. The photons emitted in the active region of OLEDs are coupled into three types of modes: the mode of direct transmission into the air, the glass total internal reflection mode,

and the high index ITO/organic guided mode. There have been various methods to increase the extraction efficiency of OLEDs. These methods can be divided into two categories, one is to place some nanostructures or low index materials on the substrate-air interface for the extraction of substrate-guided modes, such as, substrate surface roughening [5] and use of microlenses arrays [6]. The other is to insert some periodic nanostructures between the metallic cathode and the substrate layer to recover the waveguide loss in the ITO/organic layer, for example, using a refractive index modulation layer [7] or photonic band gap structure [8].

Two-dimensional periodic nanostructures (photonic crystals, PhCs) have previously been used with the aim of increasing the extraction efficiency of GaN-based light-emitting diodes (LEDs) [9, 10]. Similarly, PhCs structure can be added to OLEDs devices to increase the out-coupling efficiency. OLED out-coupling efficiency levels can be improved by optimizing the structural characteristics of the 2D PhCs, particularly the lattice constant (the period), the depth, the filling factor, and the lattice symmetry (square or triangle lattice).

This paper is organized as follows. In the second section, we provide a structural model of actual OLEDs in order to analyze the mechanisms that affect the light out-coupling characteristics. In this part, the mechanisms by which the 2D PhCs structures enhance the out-coupling efficiency of OLEDs are also given. In Section 3, we employ the finite-difference time-domain (FDTD) method to simulate the out-coupling efficiency of the OLEDs and describe the architecture of the device used in simulations. In Section 4, in order to find the optimal structure, we scan the structural characteristics of 2D periodic nanostructures (embedded PhCs and surface PhCs), such as, the period, the depth, and the filling factor. The influence of 2D periodic nanostructures on enhancing the out-coupling efficiency of the OLEDs is discussed, and then it is found the embedded PhCs have a key action in improving the out-coupling efficiency (about 240%) but the contribution of the surface PhCs is poor (only about 120%). Furthermore, we analyze the phenomena using the mode theory, and it demonstrates that the overlap between the mode and PhCs is related to the vertical mode profiles. At the end of this part, an optimized OLEDs structure with surface PhCs on the top of the substrate and embedded PhCs between the ITO layer and the substrate layer is designed. Finally, the conclusion is presented.

2. The OLEDs Microcavity Model and the PhCs

A schematic diagram of the OLEDs structure is shown in Figure 1. The typical OLEDs structure is a multilayer planar structure with the reflective metal contact layer, the ITO layer $(n = 1.8 \sim 2.0)$, the substrate layer (n = 1.5), and the organic layer ($n \approx 1.8$) which includes a hole injection layer, a hole transporting layer, an emitting layer, an electron transporting layer, and an electron injection layer. A small fraction of the emitted light is directed into the air because the total internal reflection can occur at the glass-ITO interface and the airglass interface. This leads to the conception of Fabry-Perot (F-P) microcavity OLEDs [11]. The out-coupling losses are caused by the surface plasmon polaritons (SPPs), the waveguide mode, the substrate mode, and the electrode absorption, as shown in Figure 1. Due to the SPPs at the interface of the metal and the organic (dielectric), about 36% of the generated light is dissipated as scattered light or as nonradiative emission in the cathode region. According to the total internal reflection that occurs at the glass-ITO interface and the air-glass interface, a greater portion of the emitted light is confined within the substrate layer and organic/ITO layer that can be guided as the substrate mode (22%) and the waveguide mode (20%). Four percent of generated light is absorbed by the metal electrodes. Thus, only about 18% of the light can escape from planner OLEDs. The total energy that is trapped as the substrate mode and the waveguide mode is up to 40%. In order to improve the light extraction efficiency, first the light that is confined within the substrate layer and the organic/ITO layer from the conventional planar structure of OLEDs should be extracted.

PhCs have previously been used to improve the extraction efficiency of GaN-based LED, and the best light extraction efficiency of the PhCs LED achieves 73% without

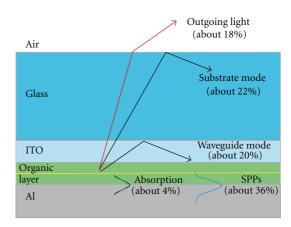


FIGURE 1: Kinds of light out-coupling losses in ordinary OLEDs.

using encapsulants [12]. PhCs are dielectric perturbations on the scale of the wavelength, offering control of the way light propagates in the medium. A guided mode that propagates within the high index layer can be characterized by an efficient index $n_{\rm eff}$, smaller than the substrate index $n_{\rm sub}$, whose wavevector is

$$k_{//} = \frac{n_{\text{eff}} \, \omega}{c} = \frac{n_{\text{sub}} \sin(\theta_m) \omega}{c},$$

$$\theta_m \ge \theta_c = \arcsin\left(\frac{n_{\text{low}}}{n_{\text{sub}}}\right),$$
(2)

where $n_{\rm low}$ is the index of the low index layer, θ_m is the mode propagation angle, and θ_c is the angle of total reflection. If the mode wavevector is $k_{//} = n_{\rm eff}\omega/c \le n_{\rm low}\omega/c$, the light will radiate from the substrate layer into the low index layer and form the leaky mode. In the presence of PhCs, the guided modes become Bloch modes [12] and the wavevector $k_{//}$ is now coupled to other harmonics $k_{//} + G$ by the reciprocal lattice vectors G, increasing extraction efficiency. To diffract the guided light into the low index layer, the lattice constant p of the PhCs needs to satisfy the diffraction condition,

$$k_{//} = |k_{//} + mG_0| \le \frac{n_{\text{low}} \omega}{c},$$
 (3)

where $G_0 = 2\pi/p$ and m is an integer (determining which harmonic is responsible for diffraction to the low refractive index layer). The Bloch mode is then referred to as a leaky mode, because its power leaks to the low index layer as it propagates. So the PhCs can improve the light extraction efficiency of the OLEDs. The diffraction condition depends on the wavelength, the lattice constant, and the mode propagation angle.

3. Numerical Analysis

In this study, the three-dimensional (3D) FDTD method was employed for simulations, which is a space and time discretization of Maxwell curl equations [13]. The FDTD calculation domain is shown in Figure 2. The simulation structure was composed of a glass layer, a SiN_x layer, an ITO layer, an organic layer, and a metal contact layer. The 2D PhCs were

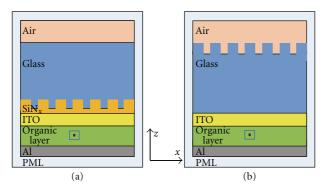


FIGURE 2: Schematics of OLED structure with (a) embedded PhCs between the ITO layer and the substrate (b) surface PhCs etched on the substrate.

embedded in a glass-substrate interface or located on the top surface of the glass layer, as shown in Figures 2(a) and 2(b). Dipole sources were chosen as the excitation source since it has been proved that the electron-hole-recombination can classically be represented by a dipole [14]. Multiple dipole sources are intrinsically suited for the simulation of the active layer in 3D FDTD method. Nevertheless, the attempt of using multiple dipole sources as well as periodic continuation boundary conditions is not convenient since it will lead to a nonphysical interference pattern. Therefore, a single dipole source within a finite computational domain was chosen. Furthermore, a perfectly matched layer (PML) [15] enclosing the entire simulation domain was used to absorb outgoing waves and avoid nonphysical reflections (see Figure 2). In addition, inhomogeneous mesh was used during the simulation, the grid size was 15 nm in the x and ydirections and 10 nm in the z direction.

The power loss in materials (ITO and glass) during the simulation was ignored since the imaginary part of the ITO and glass index is closed to zero at the wavelength of $0.55 \,\mu m$ (see Figure 3) [16].

The extraction efficiency $\eta_{\rm ext}$ was calculated from the power flux extracted from the OLEDs $P_{\rm out}$ with respect to the overall emitted power from the active layer $P_{\rm emit}$ (see Figure 2):

$$\eta_{\text{ext}} = \frac{P_{\text{out}}}{P_{\text{emit}}} = \frac{P_{z,\text{out}}^+}{P_{x,\text{in}}^+ + P_{x,\text{in}}^- + P_{y,\text{in}}^+ + P_{y,\text{in}}^- + P_{z,\text{in}}^+ + P_{z,\text{in}}^-}.$$
(4)

With $P_{z,\text{out}}^+$ the power flow integrated over a plane just above the OLEDs structure and $P_{x,y,z,\text{in}}$ the integrated power flux through the planes normal to x, y, or z enclosing the source. The + and - signs indicate power flow parallel or antiparallel to the corresponding axis.

The extraction efficiency enhancement factor F is defined as follow:

$$F = \frac{\eta_{\text{ext}}}{\eta_{\text{con}}},\tag{5}$$

where $\eta_{\rm ext}$ is the extraction efficiency of the OLEDs with PhCs structures, and $\eta_{\rm con}$ is the extraction efficiency of the conventional OLEDs.

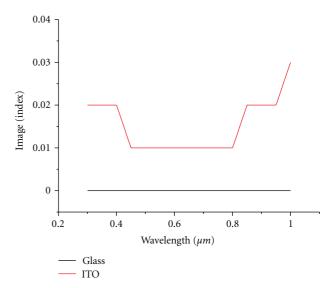


FIGURE 3: The imaginary part of the index as a function of wavelength. The solid red line shows the imaginary part of the index of ITO while the solid black line shows the imaginary part of the index of glass.

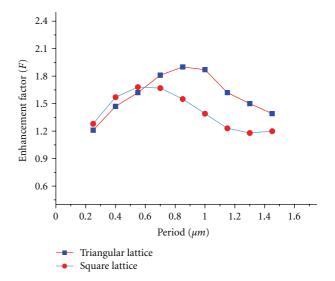


FIGURE 4: The enhancement factor of triangular lattice PhCs and square lattice PhCs as a function of period.

In the following, the continued guided wave was used as the source in the organic layer, with its vacuum wavelength of 0.55 μ m at the plane in the center of the organic layer. The enhancement of the output coupling efficiency was studied based on the standard embedded PhCs with the filling factor f=0.35 and the etched depth $d=0.3\,\mu$ m (as shown in Figure 2(a)), when the period varied from 0.3 μ m to 1.4 μ m (see Figure 4). The filling factors of triangular lattice and square lattice PhCs are expressed, respectively, as follows [17]

$$f_{\text{triangular}} = \frac{2\pi R^2}{\sqrt{3}p^2},$$
 (6)
 $f_{\text{square}} = \frac{\pi R^2}{p^2},$

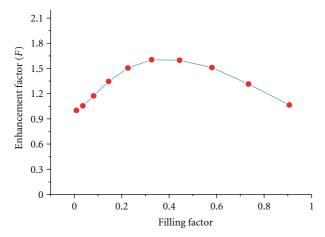


FIGURE 5: Enhancement of the out-coupling efficiency as a function of filling factor.

where, R is the radius of the hole which is filled with the glass in Figure 2(a) or air hole in Figure 2(b). From Figure 4, it can be seen that the enhancement factor of triangular PhCs was approximately equal to the square lattice PhCs when the period was changed from $0.3~\mu m$ to $0.7~\mu m$. However, the F of triangular PhCs was obviously much larger than the square lattice with the period was between $0.7~\mu m$ to $1.4~\mu m$. And the average F of triangular lattice was also larger than the square lattice PhCs. Thus, triangular lattice PhCs were selected for the next simulations, since they have better performances than square ones.

The dependence of the enhancement factor F on the PhCs filling factor is illustrated in Figure 5 which shows that the F is lower when the filling factor is too small or too large. The highest enhancement was obtained at about f=0.4. These results are in agreement with [18].

Optimization of the PhCs is difficult, because it involves solving a multiparameter inverse problem. There are countless combinations of vacuum wavelength, lattice symmetry, period (lattice constant), filling factor and depth of PhCs, and it is impossible to say which one gives the most efficient PhCs structure in releasing the trapped energy in the OLEDs structure. From the above discussion, in order to simplify the problem we choose triangular lattice PhCs with filling factor f=0.35 to analyze the enhancement of the out-coupling efficiency using the vacuum wavelength $\lambda=0.55\,\mu\mathrm{m}$. In the next section, we concentrate on studying the influence of the PhCs parameters, such as, lattice constant (period), depth of the PhCs and thickness of the ITO layer on the enhancement of the output-coupling efficiency.

4. Simulation Results and Discussion

4.1. Influence of the Embedded PhCs on the Enhancement of the Out-Coupling Efficiency. For an OLED with embedded PhCs, the dependence of the enhancement on the PhCs parameters was calculated based on a standard embedded PhCs structure with the period $p=0.5\,\mu\text{m}$, the depth $d=0.3\,\mu\text{m}$, the thickness of the SiN_x layer $T=0.4\,\mu\text{m}$,

and the height of the ITO layer $h = 0.2 \,\mu\text{m}$ as shown in Figure 2(a). Each parameter was varied in turn while other parameters were kept constant, and the enhancement factor F was calculated. Different Fs of light out-coupling efficiency with period p varying from 0.3 μ m to 1.4 μ m were calculated as illustrated in Figure 6(a). From Figure 6(a), it can be seen that F was low when the p was too small or too large. The F was kept at a larger value when the p was changed from $0.5 \,\mu\text{m}$ to $1.1 \,\mu\text{m}$. The wavevector $k_{//}$ became Bloch mode and radiated from the substrate layer into the low index layer by the reciprocal lattice vectors G according to the theory in Section 2. The reciprocal lattice vectors G was decided on by the period p of the PhCs. Evidently, each guided mode has a separate optimum reciprocal lattice vector for maximum extraction and is diffracted into the lower refractive index layer. The OLEDs structure is a multimode waveguide, and the single period hardly enhances the total extraction efficiency of all the modes. Thus, it is reasonable that the p of $0.5 \,\mu\text{m} \sim 1.1 \,\mu\text{m}$ was chosen in the experiment.

The enhancement factor F was plotted as a function of depth in Figure 6(b), which shows that F increased with the depth d increasing. A maximum value of 172% was obtained at a depth of $0.4\,\mu\mathrm{m}$. In this case, the depth of the PhCs d is equal to the SiN_x layer. It means that a larger F can be obtained by etching PhCs deeply through the SiN_x layer. The F grows as the depth of PhCs increases, and this is related to the overlap of the vertical guided mode profile with the PhCs layer. For small PhCs depth $d < 0.1\,\mu\mathrm{m}$, the attenuation length [18] of the guided mode profile within the PhCs layer is larger than the etch depth, hence, a steep increase is found until the mode profile negligibly penetrates into the low index layer. For $d > 0.2\,\mu\mathrm{m}$, the enhancement factor grows since the guided mode is squeezed more and more between the metal layer and the PhCs layer.

The effect of the height of the ITO layer h was also investigated. The relationship between enhancement factor F and h which was changed from $0 \mu m$ to $0.4 \mu m$ is shown in Figure 6(c). The F almost linearly decreased with increasing h, and the largest value 187% was obtained when the height ITO layer was $0 \mu m$. Because the power of the waveguide mode was mostly confined in the region between the ITO/organic layer and the PhCs, the smaller h resulted in high energy concentrated in the PhCs layer. Theoretically, to get the largest enhancement factor, the height of the ITO layer should be chosen as $0 \mu m$. However, this is not reasonable because the ITO layer is the electrode of OLEDs. The PhCs can be directly patterned in the ITO layer of the glass cylinder to replace the PhCs in the SiN_x layer. In addition, there was no noticeable degradation of electrical characteristics under typical operating conditions [19].

The patterned PhCs ITO layer is a good choice to improve the enhancement factor of the out-coupling efficiency. The patterned ITO layer was fabricated by the bellow method, the ITO layer was deeply etched through the organic layer and the holes were filled with glass. The influence of the height of the ITO PhCs H on enhancing the out-coupling efficiency was studied, and the enhancement factor F of out-coupling efficiency was found when H varied from $0 \, \mu m$ to

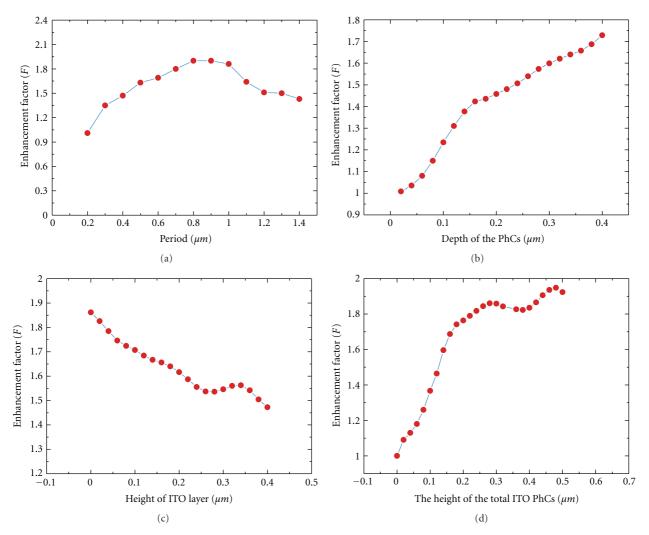


FIGURE 6: Enhancement of light out-coupling efficiency as a function of (a) period of the PhCs p, (b) depth of PhCs embedded in the SiN_x layer d, (c) height of ITO layer h, and (d) height of the total ITO layer H.

 $0.5 \, \mu \text{m}$ in Figure 6(d). The F significantly increased as H was changed from $0 \, \mu \text{m}$ to $0.3 \, \mu \text{m}$. The attenuation length [18] of the guided mode profile within the PhCs layer was large than H, and hence a steep increase was found until $H=0.3 \, \mu \text{m}$. Then an oscillation could be found in the range of $0.3 \, \mu \text{m} < H < 0.5 \, \mu \text{m}$, and F gradually reached a constant 180%. Since low-order modes are strongly evanescent in the etched region, their diffraction does not significantly increase for H larger than $\sim \lambda/n_{\text{PhC}}$ [9], where n_{PhC} is the average index of the PhCs layer. It can be expressed as follows:

$$n_{\rm PhC} \approx \sqrt{f \varepsilon_{\rm glass} + (1 - f) \varepsilon_{\rm ITO}}.$$
 (7)

The peak occurred at a height H equal to $0.3 \, \mu \text{m}$. However, this ascending trend approximately kept constant at this depth and changed to fluctuation as the PhCs were etched deeper. This implies that there is no additional benefit from a much deeper ITO layer.

To fully explain the variation trend shown in Figure 6(d), the vertical mode profiles of the ordinary OLEDs structures are first discussed as shown in Figure 7 (actually, there are

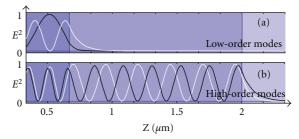


FIGURE 7: The vertical mode profiles of the ordinary OLEDs structures. (a) low-order modes (b) high-order modes.

many modes in the multilayer planar structure, we used four modes of these to express the modes profiles). As shown in Figure 7(a), the power of these low order modes was confined in the ITO/organic layer, so the embedded PhCs could be used to improve the out-coupling efficiency by extracting the power of these low order modes. Figure 7(b) is the high-order modes profiles whose power was located

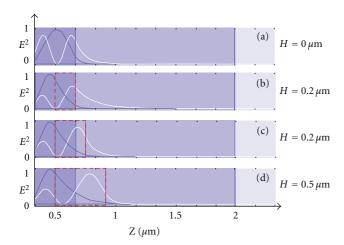


FIGURE 8: The vertical low-order modes profiles of the OLEDs structure with embedded ITO PhCs. The region in the red rectangle is the PhCs layer.

in the substrate layer. Similarly, the out-coupling efficiency was enhanced using surface PhCs to extract the high-order modes power. Distributions of these low-order modes with ITO PhCs thicknesses H are provided in Figure 8. The index of the PhCs layer can be obtained by the formula (7), which is larger than the index of the glass and smaller than the index of the organic layer. Since, these low modes slowly penetrated into the PhCs layer with H increasing from $0 \mu m$ to $0.5 \mu m$, the interaction between the PhCs and these modes increased, and thus the out-coupling efficiency grew with changes in H. When $H = 0.2 \,\mu\text{m}$, the peak of first-order mode entered into the PhCs layer, and most of the power of the first-order mode escaped from the organic layer. The peak of the ground state mode was out of the PhCs layer, whose power was partly still in the organic layer. The peak of the ground state mode became closer and closer to the PhCs layer with H increasing, and thus the overlap of this mode with the PhCs increased and the power strongly diffracted to the substrate. When $H = 0.5 \,\mu\text{m}$, the peak of the ground state mode got very close to the PhCs but was still in the high index layer, the out-coupling efficiency kept constant at 180% with a small oscillation.

To get much higher light extraction efficiency, PhCs etched through the active layer have been used in the GaN-based LED [20]. A standard embedded PhCs OLEDs structure with 0.3 µm PhCs pattern ITO layer was used in simulations, and the glass cylinder penetrates into the organic layer with the thickness T. The enhancement factor F of the structure with T varying from $0 \mu m$ to $0.2 \mu m$ at an interval of 0.01 μ m was calculated. These results are shown in Figure 9. It was found that the enhancement factors F almost linearly increased from approximately 180% to 240% when T was changed from $0 \mu m$ to $0.2 \mu m$. The turning point occurred at a thickness equal to 0.13 μ m. When $T \ge 0.13 \mu$ m, the slope of the increasing line was larger than that for $T \le$ $0.13 \,\mu\text{m}$, and a maximum of 240% was obtained at T= $0.2 \,\mu\text{m}$. Similarly, the vertical mode profiles of the ordinary OLEDs structure were studied. As shown in Figure 10, the

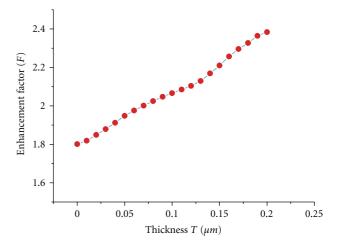


FIGURE 9: The enhancement factors F of the structure with thickness T.

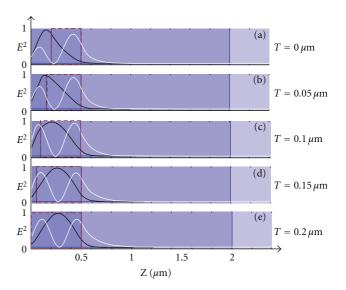


FIGURE 10: The vertical low-order modes profiles of the OLEDs structure with PhCs embedded into organic layer. The region in the red rectangle is the PhCs layer.

peak of the first-order mode penetrates completely into the PhCs layer, which hardly affects the out-coupling efficiency. To simplify the problem, only the ground state mode is considered. The peak of this mode got closer and closer to the PhCs layer when T was changed from $0\,\mu\mathrm{m}$ to $0.1\,\mu\mathrm{m}$. This implies that the interaction between the mode and the PhCs becomes stronger and stronger. When $T \geq 0.1\,\mu\mathrm{m}$, the peak of ground state mode completely enters into the PhCs layer, the overlap of the mode and PhCs had a much steeper enhancement, and a maximum of 240% was obtained at $T = 0.2\,\mu\mathrm{m}$.

4.2. Influence of the Surface PhCs on the Enhancement of the Out-Coupling Efficiency. To analyze the effect of the surface PhCs on the enhancement of the light extraction, we used

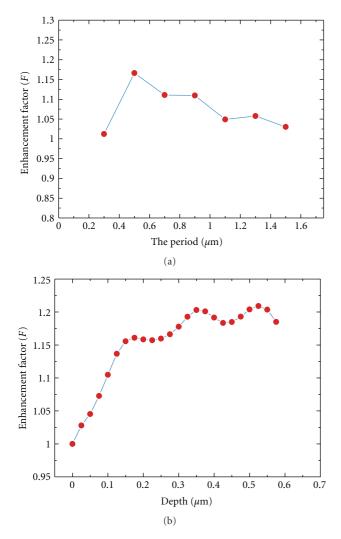


FIGURE 11: Enhancement of the out-coupling efficiency as a function (a) the period and (b) the depth of PhCs.

an approach similar to that of the embedded PhCs. We used the surface PhCs structure with the period $p = 0.5 \mu m$, depth of the PhCs $d = 0.2 \,\mu\text{m}$ as the standard structure (see Figure 2(b)). The enhancement is depicted as a function of the period p and depth d in Figures 10(a) and 10(b). The highest enhancement factor F was obtained at the period of 0.5 \sim 0.9 μ m. The result is close to the embedded PhCs, but somewhat differently, the maximum is only about 120%. From Figure 11(b), it can be found that the light outcoupling efficiency dramatically increased when the surface PhCs were etched from $0 \mu m$ to $0.35 \mu m$. This is attributed to the strong overlap between the high-order guided modes and PhCs. As shown in Figure 12, the peaks of these modes slowly entered into the PhCs layer with d increasing. Much more power of the high-order guided modes can escape from the substrate layer. When $d \ge 0.35 \,\mu\text{m}$, this ascending trend stopped and changed to fluctuation as the PhCs were etched deeper. Because peaks of these high-order modes have been located in the PhCs regions, deeper etched PhCs cannot enhance the interaction between these modes and PhCs. This

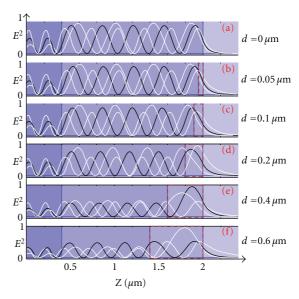


FIGURE 12: The vertical high-order modes profiles of the OLEDs structure with surface PhCs. The region in the red rectangle is the PhCs layer.

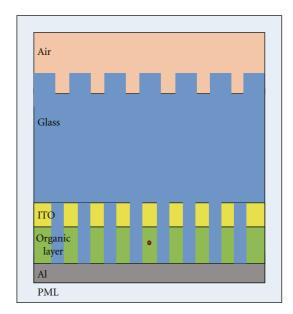


FIGURE 13: Schematics of optimized OLED structure with embedded PhCs and surface PhCs.

implies that there is no additional benefit from drilling the holes deeper and deeper. From the simulation results, it was found that the surface PhCs play a poor role in enhancing the out-coupling efficiency of the OLEDs (about 120%). In the experiment, the enhancement factor F of about 130% with surface PhCs was obtained [21].

4.3. Optimized OLEDs Structure with Embedded PhCs and Surface PhCs. We designed an OLED structure with embedded PhCs and surface PhCs (see Figure 13). The parameters of embedded PhCs were set as period $p = 0.7 \,\mu\text{m}$, height

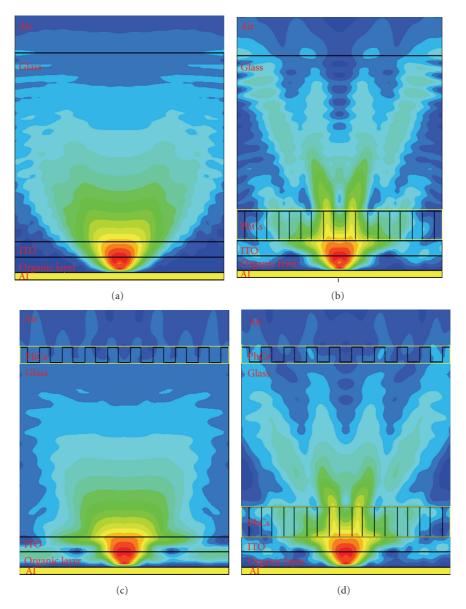


FIGURE 14: The vertical power distribution of (a) ordinary OLEDs, (b) OLEDs with embedded PhCs, (c) OLEDs with surface PhCs, and (d) OLEDs with embedded PhCs and surface PhCs. The region in the yellow rectangle is the PhCs layer.

of the ITO layer $h=0.3\,\mu\mathrm{m}$, and depth $d=0.5\,\mu\mathrm{m}$. The ITO layer and the organic layer were patterned with PhCs using glass. At the same time, the surface PhCs structure with the period $p=0.5\,\mu\mathrm{m}$ and depth $d=0.3\,\mu\mathrm{m}$ was etched in the surface of the substrate. An enhancement factor F of 290% was obtained via FDTD simulation. Figure 14(a) shows that with the vertical power distribution of ordinary OLEDs, most of emitted light from the organic layer is confined in the high index layers. The emitted light was redistributed by the embedded PhCs [22] in this structure, as shown in Figure 14(b), since the light can be easily extracted by the embedded PhCs. From the results presented in the Section 4.2, it was found that the top PhCs contribute little to enhance the out-coupling efficiency of OLEDs. The surface PhCs can extract a small fraction of the light (the power

of the high order modes), as illustrated in Figure 14(c). The structures with embedded PhCs and surface PhCs (see Figure 14(d)) present an effective way to avoid energy spreading into the ITO/organic layer and substrate layer and contribute to the extraction of low-order modes and high-order modes. This proposed structure could be a very promising candidate for high extraction efficiency OLEDs.

5. Conclusion

In this paper, we employed the finite-difference time-domain (FDTD) method to study the improvement of the out-coupling efficiency using embedded PhCs and surface PhCs. Some parameters of the PhCs including the filling factor, the depth, and the lattice constant were investigated. The

result shows that the embedded PhCs play a key role in enhancing the out-coupling efficiency, a maximum of 187% was obtained using SiN_x PhCs, and the largest value of 240% was obtained when the PhCs were etch into the organic layer. The out-coupling efficiency of the surface PhCs is only about 120%, so it has a poor role in improving the out-coupling efficiency. And then we analyzed the phenomena by using the mode theory, which showed that the low-order modes and high-order modes should be modified to escape from OLEDs using the double PhCs. It demonstrated that the overlap between the mode and PhCs is related to the vertical mode profiles and that it is an effective attempt to enhance the light extraction efficiency by changing the distributions of vertical mode profiles. Finally, the enhancement of the extraction efficiency in excess of 290% was observed for the optimized double photonic crystal pattern. This proposed that structure could be a very promising candidate for high extraction efficiency OLEDs.

Acknowledgments

The work was supported by the National Natural Science Foundation of China (61077043), the National Basic Research Program of China through Grands no. 2009CB-930503 and 2009CB930501. The authors would like to thank Dr. Manfred Hammer of the University of Twente for the codes he provided, which were the basis of mode analyses shown in Figures 8, 9, 11, and 12. The authors would also like to thank Dr. Edward C. Mignot, Shandong University, for linguistic advice.

References

- [1] T. Sekitani, H. Nakajima, H. Maeda et al., "Stretchable active-matrix organic light-emitting diode display using printable elastic conductors," *Nature Materials*, vol. 8, no. 6, pp. 494–499, 2009.
- [2] E. C. W. Ou, L. Hu, G. C. R. Raymond et al., "Surface-modified nanotube anodes for high performance organic light-emitting diode," *ACS Nano*, vol. 3, no. 8, pp. 2258–2264, 2009.
- [3] Z. Yu, L. Hu, Z. Liu et al., "Fully bendable polymer light emitting devices with carbon nanotubes as cathode and anode," *Applied Physics Letters*, vol. 95, no. 20, Article ID 203304, pp. 3304–3307, 2009.
- [4] M. A. Baldo, D. F. O'Brien, Y. You et al., "Highly efficient phosphorescent emission from organic electroluminescent devices," *Nature*, vol. 395, no. 6698, pp. 151–154, 1998.
- [5] J. Zhou, N. Ai, L. Wang et al., "Roughening the white OLED substrate's surface through sandblasting to improve the external quantum efficiency," *Organic Electronics*, vol. 12, no. 4, pp. 648–653, 2011.
- [6] J. H. Lee, Y. H. Ho, K. Y. Chen et al., "Efficiency improvement and image quality of organic light-emitting display by attaching cylindrical microlens arrays," *Optics Express*, vol. 16, no. 26, pp. 21184–21190, 2008.
- [7] K. Hong, H. K. Yu, I. Lee, K. Kim, S. Kim, and J. L. Lee, "Enhanced light out-coupling of organic light-emitting diodes: Spontaneously formed nanofacet-structured MgO as a refractive index modulation layer," *Advanced Materials*, vol. 22, no. 43, pp. 4890–4894, 2010.

- [8] Y. J. Lee, S. H. Kim, J. Huh et al., "A high-extraction-efficiency nanopatterned organic light-emitting diode," *Applied Physics Letters*, vol. 82, no. 21, pp. 3779–3781, 2003.
- [9] A. David, T. Fujii, R. Sharma et al., "Photonic-crystal GaN light-emitting diodes with tailored guided modes distribution," *Applied Physics Letters*, vol. 88, no. 6, 2006.
- [10] D. H. Long, I. K. Hwang, and S. W. Ryu, "Design optimization of photonic crystal structure for improved light extractionof GaN LED," *IEEE Journal on Selected Topics in Quantum Electronics*, vol. 15, no. 4, pp. 1257–1263, 2009.
- [11] H. Benisty, H. De Neve, and C. Weisbuch, "Impact of planar microcavity effects on light extraction—Part I: basic concepts and analytical trends," *IEEE Journal of Quantum Electronics*, vol. 34, no. 9, pp. 1612–1631, 1998.
- [12] J. J. Wierer, A. David, and M. M. Megens, "III-nitride photonic-crystal light-emitting diodes with high extraction efficiency," *Nature Photonics*, vol. 3, no. 3, pp. 163–169, 2009.
- [13] A. Taflove and S. C. Hagness, Computational Electrodynamics: The Finite-Difference Time-Domain Method, Artech House, Norwood, Mass, USA, 2005.
- [14] H. Benisty, R. Stanley, and M. Mayer, "Method of source terms for dipole emission modification in modes of arbitrary planar structures," *Journal of the Optical Society of America A*, vol. 15, no. 5, pp. 1192–1201, 1998.
- [15] J. P. Berenger, "A perfectly matched layer for the absorption of electromagnetic waves," *Journal of Computational Physics*, vol. 114, no. 2, pp. 185–200, 1994.
- [16] P. Vandersteegen, C. Van Buggenhout, P. Bienstman, and R. Baets, "Numerical investigation of a 2D-grating for light extraction of a bottom emitting OLED," in *Proceedings of* the International Conference on Transparent Optical Networks (ICTON '06), vol. 2, pp. 211–214, June 2006.
- [17] A. David, *High-efficiency GaN-based light-emitting diodes: light extraction by photonic crystals and microcavities*, Ph.D. thesis, Ecole Polytechnique, Palaiseau, France, 2006.
- [18] C. Wiesmann, Nano-structured LEDs-Light extraction mechanisms and applications, Ph.D. thesis, Science Faculty, Universität Regensburg, Regensburg, Germany, 2009.
- [19] Y. R. Do, Y. C. Kim, Y. W. Song, and Y. H. Lee, "Enhanced light extraction efficiency from organic light emitting diodes by insertion of a two-dimensional photonic crystal structure," *Journal of Applied Physics*, vol. 96, no. 12, article 8, pp. 7629– 7636, 2004.
- [20] S.-C. Wang, Y.-W. Cheng, Y.-F. Yin et al., "Interactions of diffraction modes contributed from surface photonic crystals and nanoholes in a GaN-based light-emitting diode," *Journal* of *Lightwave Technology*, vol. 29, no. 24, Article ID 6065741, pp. 3772–3776, 2011.
- [21] P. Vandersteegen, A. U. Nieto, C. Van Buggenhout et al., "Employing a 2D surface grating to improve light out coupling of a substrate emitting organic LED," in *Light-Emitting Diodes: Research, Manufacturing, and Applications XI*, vol. 6486 of *Proceedings of the SPIE*, pp. 64860H1–64860H8, January 2007.
- [22] M. Fujita, S. Takahashi, Y. Tanaka, T. Asano, and S. Noda, "Applied physics: simultaneous inhibition and redistribution of spontaneous light emission in photonic crystals," *Science*, vol. 308, no. 5726, pp. 1296–1298, 2005.

Hindawi Publishing Corporation Advances in Materials Science and Engineering Volume 2012, Article ID 247976, 4 pages doi:10.1155/2012/247976

Research Article

Enhancement of Efficiency and Lifetime of Blue Organic Light-Emitting Diodes Using Two Dopants in Single Emitting Layer

Jianning Yu,^{1,2} Na Wei,¹ Chong Li,³ Bin Wei,¹ Wei Huang,³ Taiju Tsuboi,⁴ Jianhua Zhang,² and Zhilin Zhang¹

- ¹ Key Laboratory of Advanced Display and System Applications, Shanghai University, Ministry of Education, Yanchang Road 149, Shanghai 200072, China
- ² School of Mechanical and Electronic Engineering and Automation, Shanghai University, Shanghai 200072, China
- ³ Key Laboratory for Organic Electronics and Information Displays and Institute of Advanced Materials, Nanjing University of Posts and Telecommunications, Wenyuan Road 9, Nanjing 210046, China

Correspondence should be addressed to Chong Li, li.chong@wxrtc.com and Bin Wei, bwei@shu.edu.cn

Received 9 February 2012; Revised 8 April 2012; Accepted 24 April 2012

Academic Editor: Saulius Grigalevicius

Copyright © 2012 Jianning Yu et al. This is an open access article distributed under the Creative Commons Attribution License, which permits unrestricted use, distribution, and reproduction in any medium, provided the original work is properly cited.

We have demonstrated efficient blue organic light-emitting diode with the structure of indium tin oxide/4,4′,4″-tris(N-(2-naphthyl)-N-phenyl-amino)triphenylamine/1,4-bis[N-(1-naphthyl)-N'-phenylamino]-4,4′-diamine/9,10-di(2-naphthyl)anthracene (ADN): 1-4-di-[4-(N,N-di-phenyl)amino]styryl-benzene (DSA-ph) 3 wt%/tris-(8-hydroxyquinoline)aluminum/LiF/Al. Improved efficiencies and longer operational lifetime were obtained by codoping a styrylamine-based dopant BD-3 (0.1 wt%) into the emitting layer of ADN doped with DSA-ph compared to the case of non-codoping. This was due to the improved charge balance and expansion of exciton recombination zone. The better charge balance was obtained by reducing the electron mobility of ADN which was higher than the hole mobility in the case of non-codoping.

1. Introduction

High performance and high efficiency in organic lightemitting diodes (OLEDs) depend on charge carrier distribution and charge balance. Especially the charge balance is very important to achieve a long lifetime of OLED, because the balance avoids charge leakage from the emitting layer to the electrodes. A number of methods have been undertaken to achieve high carrier density and charge balance. For example, one method is to carry out a good alignment between the Fermi level of the electrode and the corresponding transport band of the adjacent organic layer. Other methods are that indium tin oxide (ITO) has been physically (e.g., UVozone), chemically, and/or electrochemically treated, and hole injection layer (HIL) has been inserted between anode and organic layer, to reduce the carrier injection barrier height and to obtain high-density hole injection [1]. The electron mobility is largely different from the hole mobility for most organic materials, giving rise to charge imbalance. It is necessary to make the electron and hole mobilities in emitting layer (EML) comparable to each other [2]. In the present paper we propose a codoping method to obtain the comparable mobilities using a blue OLED.

Blue OLEDs are important for various applications, for example, traffic signals, full color scanners, displays, and lighting including white emission generated by color conversion method. Therefore we fabricate a blue OLED to find a method to obtain the charge-balanced OLEDs. Of various blue emitters, 1-4-di-[4-(N,N-di-phenyl)amino]styrylbenzene (DSA-ph) has been paid much attention because of its high efficiency and stability [3]. Diphenylanthracene derivative, 9,10-di(2-naphthyl)anthracene (ADN) has been used as highly efficient host material for not only green

⁴ Faculty of Engineering, Kyoto Sangyo University, Kamigamo, Kita-ku, Kyoto 603-8555, Japan

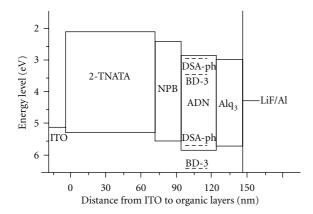


FIGURE 1: Device structure and energy levels of Device B.

and red emitters but also blue emitters such as 2,5,8,11-tetra-t-butylperylene (TBP) [4] and 4,4'-bis[2-(4-(N,N-diphenylamino)phenyl)vinyl]biphenyl (DPAVBi) [5]. Therefore we are concerned with blue OLED with emitting layer (EML) of DSA-ph doped ADN in this paper.

2. Experimental

The OLEDs were fabricated by vacuum thermal evaporation method. The base pressure was better than 7×10^{-4} Pa during the evaporation of organic materials and Al cathode. The deposition rate was lower than 0.3 nm/s for 4,4′, 4″-*tris*(N-(2-naphthyl)-N-phenyl-amino) triphenylamine (2-TNATA), 1,4-*bis*[N-(1-naphthyl)-N'-phenylamino]-4,4′-diamine (NPB), ADN, DSA-ph, and *tris*-(8-hydroxyquinoline)aluminum (Alq₃). All these materials were purchased from e-Ray Optoelectronics Technology Co., Ltd. All the device fabrication processes were performed without breaking the vacuum. The layer thickness was controlled in situ using a quartz crystal monitor.

The following two devices were fabricated:

Device A: ITO/2-TNATA (75 nm)/NPB (20 nm)/ADN: DSA-ph 3 wt% (30 nm)/Alq₃ (20 nm)/LiF (0.5 nm)/Al (100 nm);

Device B: ITO/2-TNATA (75 nm)/NPB (20 nm)/ADN: DSA-ph 3 wt%: BD-3 0.1 wt% (30 nm)/Alq₃ (20 nm)/LiF (0.5 nm)/Al (100 nm),

where the thickness of each layer and the doping concentration of emitting layer (EML) are indicated. The ITO had a thickness of 220 nm. The layer structure of Device B is shown in Figure 1, together with the highest occupied molecular orbital (HOMO) and lowest unoccupied molecular orbital (LUMO) energy levels for each layer.

The difference of Device B from Device A is that a styrylamine-based blue-emitting dye BD-3 is codoped in EML in Device B. The BD-3 was purchased from Kodak Co., Ltd. It was selected because it exhibited a very high electroluminescence (EL) efficiency of 7.2 cd/A and emitted a 448 nm deep blue light which can be distinguished from DSA-ph emission [6].

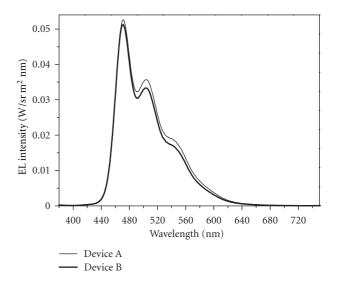


FIGURE 2: Electroluminescence spectra of Devices A and B measured at 10 V.

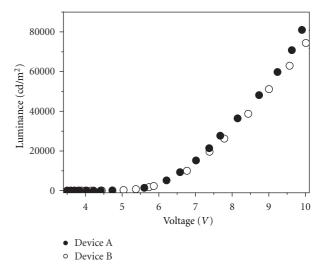


FIGURE 3: The luminance-voltage characteristics of Devices A and B

3. Results and Discussion

Figure 2 shows the EL spectra of Devices A and B measured at 10 V. The nearly identical EL spectra were obtained for the two devices, that is, intense peak at 470 nm accompanied by vibronic sidebands at 504 and about 540 nm, but a higher intensity for Device A than for Device B. The 470 nm emission band with two vibronic sidebands is ascribed to DSA-ph. Emission of ADN at 452–455 nm [7–9] was not observed, indicating efficient energy transfer from ADN to the dopant. Emission of BD-3 at 448 nm [10] was also not observed because of much smaller concentration than DSA-ph.

The luminance-voltage (L-V) and current density-voltage (J-V) characteristics are shown in Figures 3 and 4, respectively. It is found that the luminance is higher for Device A than for Device B at high voltages above about 6.5 V (Figure 3). Different OLED performance is observed between

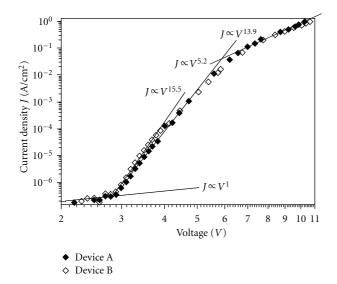


FIGURE 4: The current density-voltage characteristics of Devices A and B.

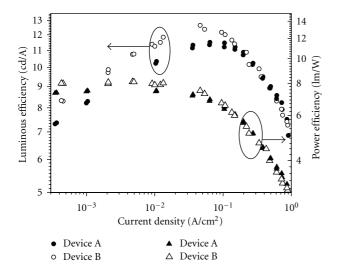


FIGURE 5: The luminous power efficiencies of Devices A and B, which are plotted against current density.

the two devices although the two devices follow the same Ohmic law of $J \propto V$ below 3 V and $J \propto V^{5.2}$ above 7 V, while Devices A and B follow $J \propto V^{13.9}$ and $J \propto V^{15.5}$ at 3-4 V, respectively (Figure 4). An increase of current density in Device B relative to Device A is observed at 3-4 V. This indicates increase of electron mobility due to decrease of electron traps in Device B.

Figure 5 shows the luminous efficiency-current density $(\eta_{\text{lumi}} - J)$ and the power efficiency-current density $(\eta_{\text{power}} - J)$ characteristics for the two devices. The efficiencies η_{lumi} and η_{power} of Device B are higher than those of Device A at current densities below 0.1 A/cm², while these efficiencies are almost the same at current densities above 0.2 A/cm² for the two devices. The external quantum efficiency (EQE) of fluorescent OLEDs is considered to be the product of the

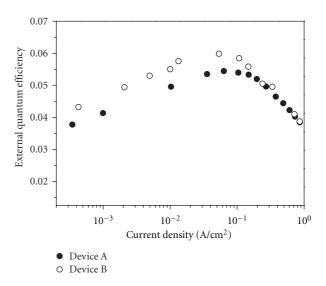


FIGURE 6: The external quantum efficiencies of Devices A and B, which are plotted against current density.

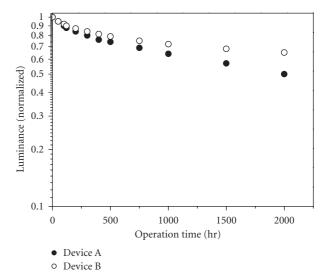


FIGURE 7: The lifetime performance of Devices A and B, which were obtained at initial luminance of 2500 cd/m² (the luminance is normalized at the initial time).

following four factors: the charge balance of holes and the electrons, the singlet exciton ratio, the photoluminescence quantum efficiency (PLQE), and the light outcoupling efficiency [11]. The charge balance and PLQE can be maximized to 100%, and the singlet ratio is considered to be 25% due to the spinstatistics of the charge recombination. Thus, if the outcoupling efficiency ranges from 20% to 30%, the upper limit of EQE becomes 5%–7.5%. It is noteworthy that we obtained an almost upper EQE of 6% (see Figure 6) in Device B based on the fluorescent emitter DSA-ph. The superiority of Device B to Device A is found in not only the EQE but also the device operational lifetime as shown in Figures 6 and 7, respectively. Regarding the lifetime, it is longer by about 1.3 times for Device B than for Device A.

We consider the reason why Device B shows higher luminous, power, and external quantum efficiencies than Device A although Device B shows lower luminance at a fixed voltage than Device A. The hole and electron mobilities of ADN are in the range of $(1-5) \times 10^{-7}$ cm² V⁻¹ s⁻¹ under external applied fields in a range of 0.5–1 MV cm⁻¹ [12]. The electron mobility is slightly higher than the hole mobility, for example, 4.65×10^{-7} cm² V⁻¹ s⁻¹ at 1 MV cm⁻¹ for the former and 4.50×10^{-7} cm² V⁻¹ s⁻¹ for the latter. However, Ho et al. found that the electron mobility of ADN was one order of magnitude higher than its hole mobility [13]. Unlike Device A, BD-3 of 0.1 wt% concentration was codoped in EML of Device B. Such a codoping leads to decrease of electron mobility by electron trapping at BD-3 molecules and becomes comparable to the hole mobility of ADN, resulting in a better charge balance in ADN emissive layer. In this way we understand the observed higher efficiencies of Device B than those of Device A.

The peak of the DSA-ph emission band is observed at 471.2 nm in Device A, while at 470.7 nm in Device B. Blue-shift is observed in Device B although the shift is very small. In the OLEDs with two-layer structure of ITO/ NPB/Alq₃/LiF/Al, the Alq₃ emission band shows blue-shift with decreasing the Alq₃ layer thickness due to optical interference effects (the recombination zone which is located at the NPB/Alq3 interface tends to be closer to the metal cathode with decreasing Alq₃ layer thickness) [14]. Therefore, the observed blue shift confirms the expansion of electron-hole recombination zone in Device B compared with Device A. It is also suggested that the expansion of exciton generation region contributes to lengthening the OLED operational lifetime. The reason is that, since the carriers are not confined in a limited area, Joule heating due to recombination of high density electrons and holes is avoided. Therefore we obtained the longer operational lifetime in Device B than in Device A.

4. Conclusions

Higher luminous and power efficiencies have been obtained at current densities below 0.1 A/cm² by codoping BD-3 into the emitting layer of ADN doped with 3 wt% DSA-ph when compared to the case of non-codoping. This improvement is attributed to the charge balance in emitting layer, which is obtained by reducing a higher electron mobility of ADN than the hole mobility. Additionally longer operational lifetime by 1.3 times has been achieved. This is attributed to the expansion of recombination zone, which leads to reduction of heat from recombination of high density electrons and holes in a narrow area.

Acknowledgments

This work was supported by the development fund for electronic and information industry (2010), the Key Innovation Project of Education Commission of Shanghai Municipality (12ZZ091), and the National Natural Science Foundation of China (60906019, 61136003).

References

- [1] L. S. Hung and C. H. Chen, "Recent progress of molecular organic electroluminescent materials and devices," *Materials Science and Engineering*, vol. 39, no. 5-6, pp. 143–222, 2002.
- [2] C. Li, M. Ichikawa, B. Wei et al., "A highly color-stability white organic light-emitting diode by color conversion within hole injection layer," *Optics Express*, vol. 15, no. 2, pp. 608–615, 2007
- [3] J. W. Ma, Z. Liang, C. Jin, X. Y. Jiang, and Z. L. Zhang, "Enhanced power efficiency for white OLED with MoO₃ as hole injection layer and optimized charge balance," *Solid State Communications*, vol. 149, no. 5-6, pp. 214–217, 2009.
- [4] J. M. Shi and C. W. Tang, "Anthracene derivatives for stable blue-emitting organic electroluminescence devices," *Applied Physics Letters*, vol. 80, no. 17, pp. 3201–3203, 2002.
- [5] J. H. Lee, Y. H. Ho, T. C. Lin, and C. F. Wu, "High-efficiency fluorescent blue organic light-emitting device with balanced carrier transport," *Journal of the Electrochemical Society*, vol. 154, no. 7, pp. J226–J228, 2007.
- [6] T. Arakane, M. Funahashi, H. Kuma et al., "Fluorescent RGB OLEDs with high performance," in *Proceedings of 44th International Symposium of the Society for Information Display (SID '06)*, vol. 37, pp. 37–40, San Francisco, Calif, USA, June 2006.
- [7] B. D. Ding, W. Q. Zhu, X. Y. Jiang, and Z. L. Zhang, "Pure blue emission from undoped organic light emitting diode based on anthracene derivative," *Current Applied Physics*, vol. 8, no. 5, pp. 523–526, 2008.
- [8] S. Tao, Z. Peng, X. H. Zhang, and S. Wu, "Efficient and stable single-dopant white OLEDs based on 9,10-bis (2-naphthyl) anthracene," *Journal of Luminescence*, vol. 121, no. 2, pp. 568– 572, 2006.
- [9] Y. Guan and L. Niu, "White organic light-emitting diodes with 9, 10-bis (2-naphthyl) anthracene," *Journal of Physics: Conference Series*, vol. 152, pp. 012049–012053, 2009.
- [10] S. W. Wen, M. T. Lee, and C. H. Chen, "Recent development of blue fluorescent OLED materials and devices," *IEEE/OSA Journal of Display Technology*, vol. 1, no. 1, pp. 90–99, 2005.
- [11] T. Tsutsui, "Progress in electroluminescent devices using molecular thin films," MRS Bulletin, vol. 22, no. 6, pp. 39–45, 1997
- [12] S. C. Tse, S. K. So, M. Y. Yeung, C. F. Lo, S. W. Wen, and C. H. Chen, "Experimental and theoretical demonstration on the transport properties of fused ring host materials for organic light-emitting diodes," *Japanese Journal of Applied Physics, Part* 1, vol. 45, no. 1, pp. 555–557, 2006.
- [13] Y. H. Ho, T. C. Lin, C. F. Wu, and J. H. Lee, "High-efficiency and long-lifetime fluorescent blue organic-emitting device," in *Organic Ligh Emitting Materials and Devices X*, vol. 6333 of *Proceedings of SPIE*, p. 633303, August 2006.
- [14] T. C. Lin, C. H. Hsiao, and J. H. Lee, "Study of the recombination zone of the NPB/Alq₃ mixed layer organic light-emitting device," in *Organic Light-Emitting Materials and Devices IX*, vol. 5937 of *Proceedings of SPIE*, pp. 59371Q-1– 59371Q-7, August 2005.